

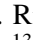


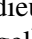
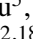
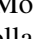




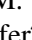


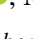


CARMENES input catalog of M dwarfs

VII. New rotation periods for the survey stars and their correlations with stellar activity[★]

Y. Shan^{1,2}, D. Revilla^{3,4}, S. L. Skrzypinski³, S. Dreizler², V. J. S. Béjar^{5,6} , J. A. Caballero⁷ ,
C. Cardona Guillén^{5,6}, C. Cifuentes⁷ , B. Fuhrmeister⁸, A. Reiners², S. Vanaverbeke⁹, I. Ribas^{10,11} ,
A. Quirrenbach¹², P. J. Amado⁴, F. J. Aceituno⁴, V. Casanova⁴, M. Cortés-Contreras³, F. Dubois^{13,14}, P. Gorrini² ,
Th. Henning¹⁵, E. Herrero^{10,11} , S. V. Jeffers¹⁶, J. Kemmer¹² , S. Lalitha¹⁷, N. Lodieu⁵, L. Logie^{13,14},
M. J. López González⁴ , S. Martín-Ruiz⁴, D. Montes³ , J. C. Morales^{10,11} , E. Nagel^{2,18} , E. Pallé^{5,6},
V. Perdelwitz^{19,8} , M. Pérez-Torres^{4,20,21} , D. Pollacco²², S. Rau^{13,14}, C. Rodríguez-López⁴ , E. Rodríguez⁴,
P. Schöfer⁴ , W. Seifert¹², A. Sota⁴ , M. R. Zapatero Osorio⁷, and M. Zechmeister²

(Affiliations can be found after the references)

Received 2 May 2023 / Accepted 7 December 2023

ABSTRACT

Aims. Knowledge of rotation periods (P_{rot}) is important for understanding the magnetic activity and angular momentum evolution of late-type stars, as well as for evaluating radial velocity signals of potential exoplanets and identifying false positives. We measured photometric and spectroscopic P_{rot} for a large sample of nearby bright M dwarfs with spectral types from M0 to M9, as part of our continual effort to fully characterize the Guaranteed Time Observation programme stars of the CARMENES survey.

Methods. We analyse light curves chiefly from the SuperWASP survey and TESS data. We supplemented these with our own follow-up photometric monitoring programme from ground-based facilities, as well as spectroscopic indicator time series derived directly from the CARMENES spectra.

Results. From our own analysis, we determined P_{rot} for 129 stars. Combined with the literature, we tabulated P_{rot} for 261 stars, or 75% of our sample. We developed a framework to evaluate the plausibility of all periods available for this sample by comparing them with activity signatures and checking for consistency between multiple measurements. We find that 166 of these stars have independent evidence that confirmed their P_{rot} . There are inconsistencies in 27 periods, which we classify as debated. A further 68 periods are identified as provisional detections that could benefit from independent verification. We provide an empirical relation for the P_{rot} uncertainty as a function of the P_{rot} value, based on the dispersion of the measurements. We show that published formal errors seem to be often underestimated for periods longwards of ~ 10 d. We examined rotation–activity relations with emission in X-rays, H α , Ca II H&K, and surface magnetic field strengths for this sample of M dwarfs. We find overall agreement with previous works, as well as tentative differences in the partially versus fully convective subsamples. We show P_{rot} as a function of stellar mass, age, and galactic kinematics. With the notable exception of three transiting planet systems and TZ Ari, all known planet hosts in this sample have $P_{\text{rot}} \gtrsim 15$ d.

Conclusions. Inherent challenges in determining accurate and precise stellar P_{rot} means independent verification is important, especially for inactive M dwarfs. Evidence of potential mass dependence in activity–rotation relations would suggest physical changes in the magnetic dynamo that warrants further investigation using larger samples of M dwarfs on both sides of the fully convective boundary. Important limitations need to be overcome before the radial velocity technique can be routinely used to detect and study planets around young and active stars.

Key words. techniques: photometric – stars: activity – stars: low-mass – stars: rotation

1. Introduction

Owing in large part to a rapidly growing interest in the search for potentially habitable planets in the Galaxy, working towards a full understanding of the most prevalent type of star has gained a sense of urgency. M dwarfs are prolific hosts of rocky, temperate planets (e.g., Dressing & Charbonneau 2015; Sabotta et al. 2021; Burn et al. 2021; Ribas et al. 2023), and are the focus of several dedicated planet search programmes, including transiting planet surveys such as MEarth (Nutzman & Charbonneau 2008), SPECULOOS (Delrez et al. 2018), and EDEN (Gibbs et al. 2020), and the radial velocity (RV) survey CARMENES (Quirrenbach et al. 2018).

When evaluating the veracity of a planet candidate detection as well as assessing the formation and evolution environment of confirmed planets, the properties and behaviour of the host star are paramount considerations. A particularly important property is the rotation period (P_{rot}). While a star’s rotation may not by itself directly influence the planet’s fate, it connects many of the other factors that do matter. For example, rotation controls the magnetic activity and field strength of the star, which in turn govern its chromospheric emission and the dosage of high-energy radiation received by orbiting planets, thus shaping their atmospheres (e.g., Lammer et al. 2003; Ribas et al. 2005; Sanz-Forcada et al. 2011; Owen & Jackson 2012; Lampón et al. 2021). The rotational evolution of the host star therefore influences the history of a planet’s evolution. Relatedly, the length of this history, that is, the ages of planet-hosting stars, can be inferred from P_{rot} through gyrochronological relations (e.g., Gaidos et al. 2023; Engle & Guinan 2023). Moreover, the visibility of stellar surface inhomogeneities in the form of spots and faculae repeats

[★] Full Tables C.1, C.2, C.4 and ground-based light curves used in this work are available at the CDS via anonymous ftp to cdsarc.cds.unistra.fr (130.79.128.5) or via <https://cdsarc.cds.unistra.fr/viz-bin/cat/J/A+A/684/A9>

with the periodicity of rotation and can be mistaken for, or distract from, planetary signals in both photometry and spectroscopy (e.g., Knutson et al. 2011; Oshagh et al. 2014; Perryman 2018; Rackham et al. 2018; Cale et al. 2021).

Quantifying stellar rotation is also crucial for understanding the nature of stars themselves. Measuring the spin evolution of stars can shed light on their interior structure and the principles of the magnetic dynamo and its coupling to angular momentum loss mechanisms. Rotation rates are linked to the age and activity level of stars through various gyrochronology and age–rotation–activity relationships (e.g., Barnes 2007; Wright et al. 2011; Reiners et al. 2014; Gaidos et al. 2023; Engle & Guinan 2023). For example, rapid rotation is usually associated with youth and high levels of activity. There have been many recent efforts to characterize these relationships for late-type stars (e.g., Reiners & Basri 2008; McQuillan et al. 2013a; Newton et al. 2016b, 2017, 2018; Stelzer et al. 2016; Astudillo-Defru et al. 2017a; Suárez Mascareño et al. 2018; Wright et al. 2018; González-Álvarez et al. 2019; Raetz et al. 2020; Magaúda et al. 2020, 2022a; Medina et al. 2020; Ramsay et al. 2020; Popinchalk et al. 2021; Boudreaux et al. 2022; Pass et al. 2022). For instance, McQuillan et al. (2013a) showed a well-defined upper limit in P_{rot} for early-M dwarfs that depends monotonically and continuously on stellar mass. Newton et al. (2016b) pointed out that the period distribution of fully convective field M dwarfs hints at a rapid spin-down phase from <10 d to >50 d. Several authors noticed a very tight correlation between Ca II H&K emission and P_{rot} for slow rotators (Astudillo-Defru et al. 2017a; Suárez Mascareño et al. 2018), which is useful for predicting P_{rot} whenever R'_{HK} ($\equiv L_{\text{Ca II H\&K}}/L_{\text{bol}}$) could be readily measured. According to Magaúda et al. (2022a), the X-ray saturation regime shows hints of mass-dependent behaviour. However, few of these aforementioned studies involved by themselves a large sample that spans the entire range of M dwarf spectral subtypes, ages, and rotation periods, or had at their disposal stellar properties that have been comprehensively and uniformly characterized.

As part of its planet search programme, the CARMENES¹ survey has intensively monitored a sample of more than 300 nearby field M dwarf stars (M0–9 V) using high-resolution spectroscopy during its guaranteed time observations (GTO – Quirrenbach et al. 2014; Quirrenbach & Amado 2020; Alonso-Floriano et al. 2015; Reiners et al. 2018b; Ribas et al. 2023). One important goal of the survey is to build a large set of benchmarks for studies of late-type stars and the planet population around them. This requires a comprehensive characterization of these stars. In order to accomplish this, we have constructed the Carmencita² catalogue (Caballero et al. 2016), where we have assembled extensive information on every survey star, from the literature, archival data, as well as from our own observations. This includes astrometry, imaging, photometry, and spectroscopy, from which properties such as kinematics, fundamental stellar parameters, multiplicity, planet-hosting status, activity, age, and rotation are derived (e.g., Cortés-Contreras et al. 2017; Reiners et al. 2018b; Jeffers et al. 2018; Passegger et al. 2019; Schöfer et al. 2019; Schweitzer et al. 2019; Cifuentes et al. 2020; Baroch et al. 2021; Marfil et al. 2021; Lafarga et al. 2021; Perdelwitz et al. 2021).

Stellar P_{rot} is most readily measurable via modulations in light curves, but also increasingly commonly through time series of activity-sensitive spectroscopic signatures and in spectropolarimetry data directly sensitive to surface magnetic fields. For M dwarfs, substantial catalogues of P_{rot} 's have been made available based on, for example, large transiting planet surveys from both space (e.g., Reinhold et al. 2013; McQuillan et al. 2014; Raetz et al. 2020; Ramsay et al. 2020; Gordon et al. 2021; Magaúda et al. 2022b) and the ground (e.g., Kiraga & Stepień 2007; Hartman et al. 2011; Newton et al. 2016b; Suárez Mascareño et al. 2016), as well as from RV (e.g., Suárez Mascareño et al. 2015, 2017b) and spectropolarimetry surveys (e.g., Fouqué et al. 2023; Donati et al. 2023). Currently, for the CARMENES M dwarfs, the Carmencita catalogue compiles P_{rot} from a variety of literature sources. A significant contributor is Díez Alonso et al. (2019), hereafter DA19, who measured P_{rot} for a 142 CARMENES survey stars from a homogeneous analysis of archival data taken by several photometric monitoring surveys. Complementary searches for periodicity in the CARMENES GTO sample have also been undertaken using spectroscopic activity indicators (Lafarga et al. 2021; Schöfer et al. 2022; Fuhrmeister et al. 2023). In addition, planet hosts often have their P_{rot} constrained in the discovery papers (e.g., Ribas et al. 2023, and references therein). However, many stars in this prime sample are still missing P_{rot} determinations, and some stars have conflicting or implausible periods based on comparison with multiple references or with activity signatures.

Since DA19, more photometric observations have become available for our sample. Here we continue DA19's endeavour using light curves from survey data as well as our own ground-based follow-up efforts to populate the P_{rot} catalogue for CARMENES survey stars. We also add periods from recent literature references, and perform a critical analysis of the reliability of the P_{rot} determinations for each star. Our new catalogue, therefore, builds on and supersedes DA19, and should be considered the reference P_{rot} catalogue for the CARMENES survey stars. Combined with newly available stellar parameters for this sample, we put P_{rot} for nearby M dwarfs in the context of activity, mass, age, and planet-hosting status. We examine the spread in published P_{rot} values and discuss realistic uncertainties in rotation period measurements.

In this manuscript, we describe the CARMENES survey sample in Sect. 2.1. In the rest of Sect. 2, we present the data used to measure P_{rot} , including light curves from SuperWASP, TESS, and ground-based follow-up observations, as well as time series of CARMENES spectroscopic indicators. We describe the methods for analysing the light curves from each data set in Sect. 3. Our measurements are presented in Sect. 4. Informed by comparisons with the literature (Sects. 4.1 and 4.2), $v \sin i$ (Sect. 4.3) and H α (Sect. 4.4) measurements, we assign the most credible value for each target using a framework outlined in Sect. 4.5. Sect. 4.6 characterizes the scatter in multiple P_{rot} measurements and discusses implications for realistic uncertainties. Rotation-activity relations, including X-ray, H α , R'_{HK} , and magnetic field strengths are examined in Sect. 5.1. Correlations with stellar mass, kinematics, and age are shown in Sect. 5.2. The distribution of P_{rot} 's for known planet hosts in this sample is discussed in Sect. 5.3. We summarize in Sect. 6.

2. Data

2.1. Sample

Our overall sample consists of 348 stars from the CARMENES RV survey, whose selection has been documented in previous

¹ CARMENES: Calar Alto high-Resolution search for M dwarfs with Exoearths with Near-infrared and optical Échelle Spectrographs, <https://carmenes.caha.es>

² Carmencita: CARMENES Cool dwarf Information and daTa Archive.

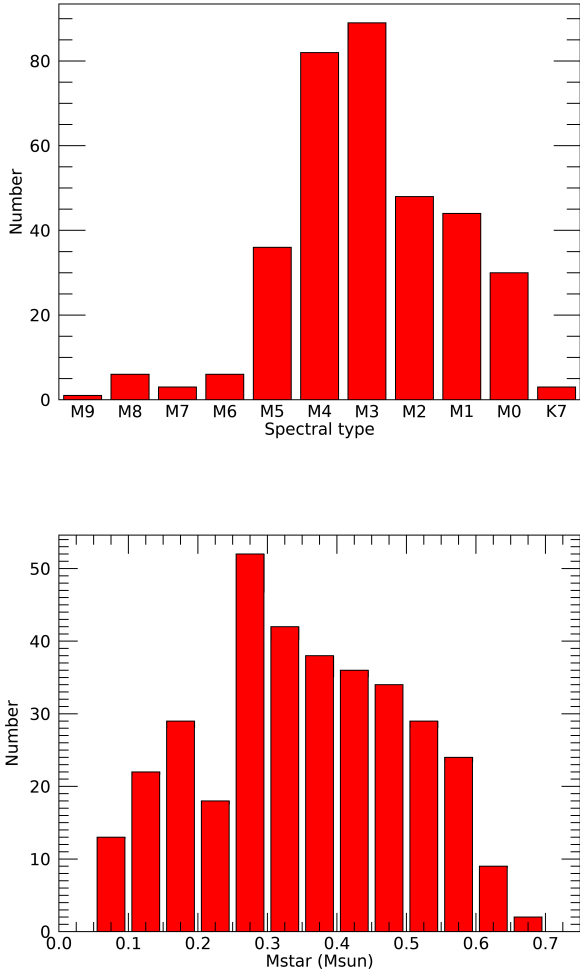


Fig. 1. Distribution of spectral type (top) and stellar mass (bottom) of the CARMENES survey sample (total of 348 stars) studied in this work.

works (e.g., Quirrenbach et al. 2014; Alonso-Floriano et al. 2015; Caballero et al. 2016; Ribas et al. 2023). As shown in Fig. 1, this sample spans the entire range of the M dwarf spectral type and masses. Most of these stars appear to be field stars, although 69 of them have been recently identified to belong to nearby stellar kinematic groups with ages $\lesssim 800$ Myr (Cardona et al. 2022).

Our goal is to compile as much information on the rotation periods of as many stars in this sample as possible. To this end, we first performed a literature search and found at least one rotation period estimate on record for 241 stars (see Sect. 4.1). We also collected new photometric and spectroscopic data to help independently derive periods for a subset of the sample stars. Table 1 presents an overview of the sources of our data and the numbers of light curves provided by each of them. More detailed descriptions are given below.

2.2. Ground-based photometry

2.2.1. SuperWASP

The Super-Wide Angle Search for Planets (SuperWASP) Survey is an all-sky photometric survey for transiting exoplanets (Pollacco et al. 2006). Two robotic telescopes, each consisting of eight cameras, observe from La Palma (Spain) and Sutherland (South Africa), chiefly through broadband filters (400–700 nm).

Since 2004, they have monitored the entire sky at high cadence (weather-permitting) for about four months per year. The typical photometric precision is $\lesssim 1\%$ for stars with $V \lesssim 11.5$ mag. The first and so far only public data release (DR1) made available data collected up to 2008 (Butters et al. 2010). This was one of several public data sets used by DA19. Data post-2008 can be obtained via direct request to the SuperWASP team. We made such a request and received SuperWASP light curves for 112 CARMENES survey stars. The light curves were produced by the SuperWASP team after custom extraction and detrending according to the Sys-Rem algorithm (Tamuz et al. 2005; Afonso et al. 2007), which corrects for systematics arising from the instrument or atmospheric extinction, leveraging the manifestation of these effects in large sets of simultaneously monitored stars. This extraction method is expected to preserve astrophysical signals such as rotational modulation.

The observations span up to nine seasons (though not necessarily contiguous), each of which typically lasts for ~ 130 days and occurs during the fall and winter months. We note that SuperWASP light curves with fewer than about 25 nights of data (i.e., $\lesssim 25$ nightly-binned data points) tend to be too sparsely populated to give credible signals. The number of light curves that exceeds this threshold (i.e., deemed potentially useful) is 99.

2.2.2. AstroLAB IRIS

Optical observations were collected for six CARMENES survey targets using the 684 mm aperture Keller $f4.1$ Newtonian New Multi-Purpose Telescope of the public observatory AstroLAB IRIS located at Zillebeke, Belgium³. The telescope is equipped with a Santa Barbara Instrument Group (SBIG) STL-6303E CCD camera operating at -20°C . A 4-inch Wynne corrector feeds the CCD at a final focal ratio of 4.39 and provides a nominal field of view of $20' \times 30'$. The $9\mu\text{m}$ physical pixels project to $0''.62$ and are read out binned to 3×3 pixels, or $1''.86$ per combined pixel. We used the B , V , and R filters from Astrodon optics. These filters closely match the Johnson-Cousins system (Goldman et al. 2006). Differential photometry relative to suitable comparison stars in the field of view were used to construct the light curves using the Lesve photometry package.

2.2.3. Observatorio de Sierra Nevada (OSN)

A number of targets were also photometrically monitored at Observatorio de Sierra Nevada (OSN)⁴ in Granada, Spain, using the T90 and T150 telescopes and different set of filters (B , V , R , I) in the Johnson photometric system. T90 is a 90 cm Ritchey-Chrétien telescope equipped with a CCD camera VersArray $2k \times 2k$ with a resulting field of view of $13.2' \times 13.2'$. The camera is based on a high quantum efficiency back-illuminated CCD chip, type Marconi-EEV CCD42-4, with optimized response in the ultraviolet (Amado et al. 2021). The T150 telescope is a 150 cm Ritchey-Chrétien telescope equipped with a CCD camera Andor Ikon-L DZ936N-BEX2-DD $2k \times 2k$, with a resulting field of view of $7.92' \times 7.92'$. The camera is based on a back-illuminated CCD chip, with high quantum efficiency from ultraviolet to near infrared. This camera also includes thermo-electrical cooling down to -100°C for negligible dark current (Quirrenbach et al. 2022).

³ <http://www.astrolab.be>

⁴ <https://www.osn.iaa.csic.es/en>

Table 1. Overview of sources of light curve data for the targets in the CARMENES survey.

Survey	Location	Instrument configuration	Band	No. of light curves ^(a)
SuperWASP	Roque de los Muchachos, Spain	8 × Andor DW436	Clear, Broad (0.4–0.7 μm)	112 (99)
	Sutherland, South Africa		Broad (0.4–0.7 μm)	
AstroLAB IRIS	Zillebeke, Belgium	0.68 m Keller + SBIG STL-6303E	<i>B, V, R</i>	6 (6)
OSN	Observatorio de Sierra Nevada, Spain	0.90 m, 1.50 m	<i>B, V, R, I</i>	22 (14)
LCOGT	Las Cumbres Observatory, Chile	0.40 m	<i>B, V, i</i>	13 (9)
TJO	Montsec Observatory, Spain	0.80 m + LAIA	<i>R</i>	5 (3)
TESS	Space	4 × 0.10 m + CCID-80	<i>T</i> (0.6–1.0 μm)	240

Notes. ^(a)The number of light curves with >25 nightly-binned epochs, i.e., deemed admissible for analysis, are given in parentheses. Applicable only to ground-based data sets.

The data were reduced in the same way for both telescopes. All CCD measurements were obtained via synthetic aperture photometry using typically a 1×1 binning (no binning). Each CCD frame was bias subtracted and flat-fielded in a standard way. Different aperture sizes were tested in order to choose the best one for our observations. A number of nearby and relatively bright stars within the frames were selected as check stars, and the best set is chosen to be used as reference stars. The data in each filter are presented as magnitude differences normalized to zero. Outliers due to bad weather conditions were previously removed. In particular, we used the same methodology as in previous works involving photometric monitoring of nearby M dwarfs with exoplanets (e.g., Amado et al. 2021; Quirrenbach et al. 2022). Of the 22 stars for which we have OSN light curves, 14 have ≥ 25 nightly-binned epochs and were retained for analysis.

2.2.4. Las Cumbres Observatory (LCOGT)

Part of our sample was observed in the *B*, *V*, and *i'* bands using the 40 cm telescopes of the Las Cumbres Observatory Global Telescope (LCOGT) network (Brown et al. 2013), during different campaigns between 2016 and 2021 under the Instituto de Astrofísica de Canarias programmes IAC2016A-004, IAC2017AB-001, IAC2018A-001, IAC2018B-005, IAC2019A-001, IAC2020A-001, IAC2020B-001, and IAC2021B-002 (PI: V. J. S. Béjar). The 40 cm telescopes are equipped with a $3k \times 2k$ SBIG CCD camera with a pixel scale of $0''.571$ providing a field of view of $29''.2 \times 19''.5$. Sky transparency conditions at the observatories were mostly clear during our observations, and the average seeing varied from one to a few arcseconds. Raw data were processed using the BANZAI pipeline (McCully et al. 2018), which includes bad pixel, bias, dark, and flat field corrections for each individual night. We performed aperture photometry for our targets and several reference stars in the same field of view, and estimated the relative flux between the target and references in order to derive the photometric light curves. We selected the most appropriate aperture for each target (typically around 10 pixels or $5''$) that minimizes the dispersion of the differential photometry. Nine of the 13 stars for which LCOGT light curves were collected have more than 25 nightly-binned epochs and are used for period analysis.

2.2.5. Montsec Observatory (TJO)

Part of the photometric monitoring was done with the Joan Oró Telescope (TJO) at the Montsec Observatory in Lleida

(Spain)⁵. The TJO is a 0.8 m robotic telescope equipped with the LAIA instrument, a $4k \times 4k$ back illuminated CCD camera Andor iKon XL with a pixel scale of $0''.4$ and a square field of view of $30'$. The instrument is also equipped with a set of Johnson *UBVRI* photometric filters.

The photometric measurements of the TJO were collected between 2019 and 2022. For all the targets, the observational strategy consisted of executing blocks of five images every two or three nights during the visibility period throughout the year. All the observations were done using Johnson *R* filter and 1×1 binning. The resulting images were calibrated with darks, bias, and flat fields with the ICAT pipeline (Colome & Ribas 2006) using standard procedures. Differential photometry was extracted with AstroImageJ (Collins et al. 2017) using the aperture size and the set of comparison stars that minimized the root-mean-square (rms) of the photometry. Out of five targets with TJO observations, we rejected two for having fewer than 25 nightly-binned epochs, leaving three for analysis.

2.3. TESS

The Transiting Exoplanet Survey Satellite (TESS) mission is a space-based all-sky photometric survey to look for transiting planets around bright stars (Ricker et al. 2015). This mission divides the entire sky into 26 sectors and observes each field continuously at high cadence (2 or 30 min) for 27.4 days at a time. The first 26 sectors constituted the primary mission and were completed between July 2018 to July 2020. Subsequently, most fields are being revisited. In this work, we used data from the primary mission, covering the southern and most of the northern hemispheres. For the stars that already have periods recovered from the first 26 sectors, we also checked data from later sectors (up to sector 47) to ensure consistency⁶.

We cross-matched the stars from the CARMENES sample with those from version 8 of the TESS Input Catalog (TICv8) using *Gaia* DR2 identifiers, when available, and otherwise via 2MASS identifiers. Of them, 240 of the survey stars were observed in the first 26 sectors. The remaining 109 stars lie in missing patches at the edges of adjacent sectors and in the ecliptic region, which was not observed until sector 42.

For our analysis, we used chiefly the 2-minute-cadence light curve products from TESS: Simple Aperture Photometry (SAP)

⁵ <https://montsec.ieec.cat/en/>

⁶ With the exception of J10360+051, which was not in the primary mission, we determined its period based on SAP data from sectors 45 and 46.

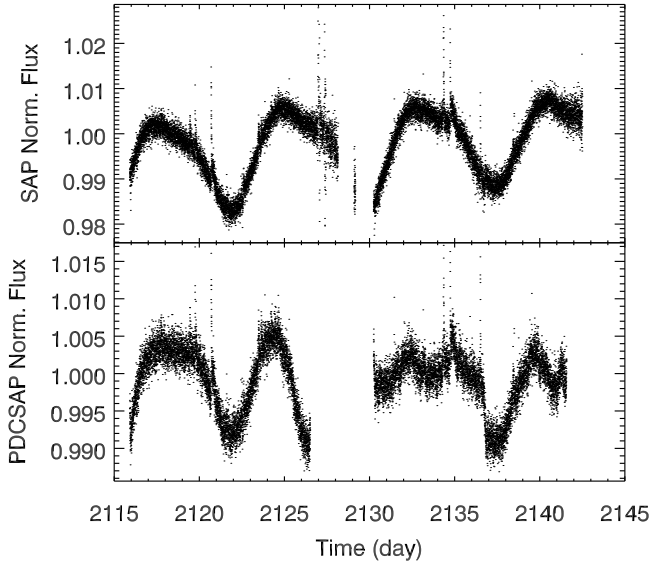


Fig. 2. SAP (top) and PDCSAP (bottom) light curves for J01339–176 from TESS sector 30. A periodic modulation at ~ 8 d is apparent in the SAP, but not in the PDCSAP. The time in the X axis is BJD – 2457 000 days.

and Pre-search Data Conditioning SAP (PDCSAP). These were available for 210 stars in our sample. For the 30 stars that do not fall into the pre-selected TESS target list but are captured in the 30-min-cadence Full Frame Images (FFIs), we custom extracted their light curves. All data were downloaded via the Mikulski Archive for Space Telescopes⁷. The data were reduced using the Python packages *Lightkurve* (Lightkurve Collaboration 2018) as well as *tesscut* (Brasseur et al. 2019). Below we describe how each data product was used.

2.3.1. PDCSAP light curves

Since the PDCSAP is optimized for planetary transit searches (Kinemuchi et al. 2012), it is most useful for detecting variability with timescales of less than a few days (see also discussion in Sect. 3.2.1). In the majority of cases, we used them as-is. For a few stars where the light curves show effects of possible contamination from nearby sources, we examined their raw Target Pixel Files (TPF) and refined the aperture masks to optimize the target’s summed light curve. In these cases, the light curves were not detrended prior to analysis.

2.3.2. SAP light curves

Despite being the ‘rawer’ predecessor of the PDCSAP that can show large, instrument-related systematics and glitches, the SAP light curves are more suitable for measuring or indicating periods between ~ 5 and ~ 30 days. Figure 2 shows the example of J01339–176, whose SAP light curve exhibits an unambiguous modulating pattern repeating at ~ 8 d, whereas its PDCSAP light curve appears to be more irregular.

2.3.3. FFI light curves

Using the Python tool *tesscut*, we recovered the 30-min cadence light curves for the 30 stars that did not have SAP. For each target star, we cut a 20×20 pixel region of the FFI around its position to create a custom TPF. Since these TPFs do not come with a predefined optimal aperture mask, we generated them ourselves. We used *lightkurve*’s *create_threshold_mask* method, which draws an aperture according to a user-given flux threshold value. For each target, we visually inspected its TPF using *tpfplotter* (Aller et al. 2020) to determine the optimal threshold value to use for creating the aperture mask. For some stars with bright close visual companions, we manually adjusted the aperture boundaries to best exclude the companions. Light curves were extracted from summing the pixels in the apertures.

2.4. Spectroscopic indicators

Various spectroscopic indicators sensitive to stellar activity have been demonstrated to exhibit variability linked to the stellar P_{rot} . Schöfer et al. (2019, 2022) and Lafarga et al. (2021) have already analysed a subset of CARMENES stars in this way. Here, we collected updated spectroscopic indicator time series from the CARMENES survey (up to February 2022) to form a sample of 205 stars with more than 20 epochs of CARMENES spectra (see Fuhrmeister et al. 2023, for more details). As chromospheric indicators we used the following features available in the CARMENES spectral range, which were demonstrated by Schöfer et al. (2019) to most likely show detectable variability related to rotation: pseudo-equivalent width (pEW) of $H\alpha$ and the two bluer Ca II infrared triplet (IRT) lines (Ca-IRTab), following Fuhrmeister et al. (2019, see their Table 2 for the integration bands used), as well as the TiO bandhead index at 7050 Å, defined as the quotient of the integrated flux density in two wavelength bands on both sides of the bandhead (see Table 3 in Schöfer et al. 2019). In addition, we used Ca II H&K data as measured by R'_{HK} , whose variability has also been associated to rotation (e.g., Suárez Mascareño et al. 2015). R'_{HK} cannot be measured from the CARMENES spectra, which does not span the blue wavelength range. Rather, we used archival data from a collection of different telescopes, mainly High Accuracy Radial velocity Planet Searcher (HARPS) and High Resolution Échelle Spectrometer (HIRES), as compiled by Perdelwitz et al. (2021). The subsample with R'_{HK} time series containing >20 epochs consists of 56 stars.

3. Data analysis

This section describes the procedures for processing and time series analysis of each dataset listed in Sect. 2. All retrieved P_{rot} ’s and other applicable information (e.g., uncertainty flags for the SuperWASP analysis) are given in Table C.2.

3.1. Ground-based photometry

3.1.1. SuperWASP

The SuperWASP light curves were first filtered for outliers on a season-by-season basis. The standard deviation (σ) threshold used for iterative outlier rejection was set to the number of σ ’s away from which we expect only one outlier for a given number of data points present in the data set assuming Gaussianity, as determined from an inverse error function. This requirement translates into a typical threshold of 3σ to 4σ .

⁷ <https://mast.stsci.edu/portal/Mashup/Clients/Mast/Portal.html>

The light curves were subsequently nightly-binned, where each bin was assigned a time and flux value corresponding to the error-weighted mean of the points that fell in the bin. The flux error of the bin was computed as the standard error of the weighted mean. By default, analysis was carried out on nightly-binned data. For 17 H α -active stars whose periods were suspected to be short, we also considered their unbinned light curves. Here we adopted the definition of H α -active from Schöfer et al. (2019): $pEW'_{\text{H}\alpha} < -0.3 \text{ \AA}$, where $pEW'_{\text{H}\alpha}$ is the H α pseudo-equivalent width measured with spectral subtraction from that work (see also Sect. 4.4). Eight of the 17 stars have compelling evidence of a period $\geq 10 \text{ d}$, usually visible in the light curve itself and supported by multiple literature measurements. For those stars, the final analyses were performed on nightly-binned data.

We constructed error-weighted Generalized Lomb-Scargle (GLS; Zechmeister & Kürster 2009) periodograms from the light curve data, using the IDL implementation of GLS⁸. The peaks of the GLS occur at the most salient sinusoidal frequencies in the data, whose significances are assessed from their false alarm probability (FAP). The FAP of a given measured peak power P_n was calculated as

$$\text{FAP}(P_n) = 1 - [1 - \text{prob}(P > P_n)]^M, \quad (1)$$

where $\text{prob}(P > P_n)$ is the probability that a signal with power P is greater than the threshold power P_n , and M is the number of independent frequencies being tested. We used the following prescription:

$$\text{prob}(P > P_n) = (1 - P_n)^{(N-3)/2} \quad (2)$$

and $M = \Delta f \Delta t$, where Δf is the range of frequencies searched and Δt the total time baseline. N is the number of data points in the time series. By default, we searched a range of frequencies from 1 d^{-1} to 10^{-3} d^{-1} , concordant with the inverse of the typical time span of SuperWASP data ($\sim 2\text{--}4$ seasons), such that $\Delta f \approx 1 \text{ d}^{-1}$. In a few cases where a very short period was expected, we searched from 10 d^{-1} in the unbinned light curve data.

Since sampling from ground-based instruments can be opportunistic and the photometry noisy, the periodograms are often difficult to interpret and require analysis based at least in part on qualitative principles. We visually examined each GLS periodogram for significant peaks with $\text{FAP} < 0.1\%$. For objects with more than one season of coverage, we looked for periodicities in the full global data set as well as on a season-by-season basis. When a period is very apparent in one well-sampled season, we accepted it even if it is not found with as much significance in other seasons. Many periodograms have multiple peaks exceeding our FAP threshold. In these cases, we evaluated the plausibility of each period signal by a visual inspection of the corresponding phase-folded light curves, aided by comparison to any reported periods in the literature and activity signatures (see Sect. 4). Daily aliases are very common and generally manifest themselves as a peak close to 1 d mirroring a strong peak at a longer period. Therefore, periods below 1.5 d were usually dismissed in favour of any identifiable counterpart peak structure symmetric across the 0.5 d^{-1} axis, unless there were strong reasons to suspect fast rotation, as evidenced by $pEW'_{\text{H}\alpha}$.

In general, we considered a detection to be valid when it manifests itself as a single dominant peak, usually with $\text{FAP} \ll 0.1\%$, either in global or in seasonal data (at least one season with more than 25 nightly-binned epochs), with the periodicity clearly visible by eye in phase-folded data. The period

should not exceed 130 d (i.e., the average length of a season) in a global analysis consisting of more than one season, or half the seasonal baseline in a seasonal analysis.

For several signals for which we are less confident, for example where multiple periods of comparable significance are present, or the formal significance is strong but the period is barely visible in the phase-folded data, we flagged them as ‘U’ for uncertain, to denote a possible signal following the nomenclature of Newton et al. (2016b). Among them are three periods that are uncomfortably close to the synodic lunar period (see below). We report these signals because they may help verify measurements in future works.

Four stars have periodicities of $\sim 28 \text{ d}$ as their most convincing signals. Since this coincides with the synodic lunar month, these periods received extra scrutiny. J13102+477 shows a 29.06 d period, which agrees well with the measurement from MEarth (28.8 d ; Newton et al. 2016b). J23556–061, which is a single-lined spectroscopic binary (SB1), shows a strong 28.53 d periodicity in one of SuperWASP seasons, driven by a repeating distinctly sharp trough pattern that is uncharacteristic of star spot modulation. However, with an orbital period $> 5000 \text{ d}$ (Baroch et al. 2021), the binary nature of J23556–061 is unlikely to explain the 28-d variability. J10584–107 has a strong 27.87 d signal in one season and a weak 28.47 d signal in another. However, this star has a resolved $v \sin i = 2.8 \text{ km s}^{-1}$ (Reiners et al. 2022) and, therefore, it is suspected to be a fast rotator. In the SuperWASP data, J04376–110 shows a highly significant 28.64 d period in its best-covered season, but a 36.69 d signal is present in another season (albeit at lower significance and with poorer coverage). We report the $\sim 28 \text{ d}$ periods of all four stars, but flagged the latter three with ‘U’.

We retrieved periods for 44 objects, with 34 considered to be reliable and 10 being uncertain, three of which due to similarity with the synodic month. An example of the SuperWASP analysis is shown in Fig. C.1 for J22330+093. This light curve spans three seasons, the latter two of which have superior coverage and exhibit significant modulations with a period of $\sim 37 \text{ d}$. We took the most significant signal from the second season to be the P_{rot} for this star.

3.1.2. Other ground-based surveys

We repeated the analysis on the light curves collected from the other ground-based facilities. We treated each data set from each telescope and bandpass separately, but we did not split any light curve into seasons. In nightly-binned data, we looked for periodicities with formal significance $\text{FAP} < 0.1\%$ and below half the total length of the corresponding data set. If a qualifying signal is found in multiple data sets for the same star, we recorded the one with the lowest FAP. In total, 12 periods were determined in this manner.

3.2. TESS

3.2.1. PDCSAP

To prepare the TESS PDCSAP light curves for analysis, points that deviated by more than 5σ from the mean magnitude, mostly comprising flares and transit features, were removed on a sector-by-sector basis. Then, we used the GLS periodogram as in Sect. 3.1.1 to find significant periods in the unbinned data. We searched for periods on a sector-by-sector basis, limiting the period search to a maximum of $\sim 13 \text{ d}$ (i.e., half of the total time baseline per sector) and a minimum corresponding to the

⁸ <https://github.com/mzechmeister/GLS/blob/master/idl/gls.pro>

Nyquist frequency. We located all peaks in the periodograms with $\text{FAP} < 1\%$ and analyzed them separately. We assessed the veracity of each period by visually inspecting the TPF, the GLS periodogram, and the overall and phase-folded light curves. Figure C.2 shows an example ‘summary page’ containing the relevant information used for diagnostics. If the periodogram displayed several significant peaks, we compared the light curve phase-folded on each candidate period to pinpoint the one that showed the clearest modulation signal at minimal scatter. In addition, we checked whether the detected period was consistent across sectors, when applicable, and was compatible with the rotation velocity $v \sin i$ (Reiners et al. 2018b) or activity indicators, such as the $pEW'_{\text{H}\alpha}$ (Schöfer et al. 2019).

Through this vetting process, we recovered 41 periods from the PDCSAP light curves, all of which are < 6 d. In some cases, significant peaks were found beyond 6 d, but closer inspection revealed them to be spurious and related to corrections introduced by producing the PDCSAP. We conclude that ~ 6 d is the limit to which rotation modulation can be accurately represented in the PDCSAP. A similar conclusion was reached by Medina et al. (2020).

3.2.2. SAP

Whereas the PDCSAP destroys astrophysical variability above a few days, the SAP is unfiltered and therefore better preserves longer-period signals (see e.g., Fig. 2). We stitched the SAP light curves across intra- and inter-sector data gaps (where applicable) using median flux normalization. We used a GLS periodogram to obtain the preliminary P_{rot} of the star, which we confirmed and refined by visual inspection of the phase-folded light curve.

From the SAP we measured P_{rot} for an additional 17 stars. All of these periods lie between 6 d and 25 d and show high consistency with literature values and activity signatures (when available). Therefore, the SAP light curves can be valuable for constraining the periods of intermediate-rotators where the PDCSAP would fail. This could be especially useful for mapping the transition region between active and inactive M dwarfs.

3.2.3. FFI

Analogous to the PDCSAP, we analyzed the 30-min cadence light curves custom-extracted from the FFIs, from which we recovered two periods: for J05366+112 and J06574+740. J06574+740 was later observed in sectors 40 and 47, where the PDCSAP data confirmed the period from the FFI analysis (see further discussion in Appendix A.2 and Fig. C.3).

3.3. Spectroscopic activity indicators

To each time series of the chromospheric indicators, a 3σ -clipping was first applied to omit outliers due to flaring or weather and instrumental issues. Here, we used the GLS periodogram as implemented in PyAstronomy⁹ (Czesla et al. 2019) to search for periods longer than 1.5 d (to exclude daily aliases) and shorter than 150 d. We defined periods with $\text{FAP} < 0.1\%$ as significant. For a given star, we required that the top significant period in a majority (minimum two) of indicators to agree within 15% to be associated with the rotation of the star. In this case, we designated the period as the simple average of all the agreeing period values.

⁹ <https://github.com/sczesla/PyAstronomy>

In all except one case, the data sets yielding acceptable periods contain at least 25 epochs. For J09468+760, the signal in three of the indicators show high significance and consistency in 24 epochs of data, and therefore we adopted the corresponding period. For several stars, we detrended the time series with a degree-two polynomial, because they revealed more convincing and plausible signals. Figure C.4 shows an example of the spectroscopic indicator time series and periodogram for J14524+123, for which the $\text{H}\alpha$ and Ca-IRT exhibit significant signals at ~ 23 d. A total of 44 stars have an admissible period measured in this manner.

4. Results

In this section, we combine results from our analysis with work by previous authors (Sect. 4.1) to provide the most comprehensive and up-to-date catalogue of P_{rot} ’s for the CARMENES M dwarf sample. Where applicable, we compare our measurements with the literature, examine several types of disagreements and consider how to decide between multiple discrepant values (Sect. 4.2). For stars with resolved $v \sin i$ and stellar radius (R_*) measurements, an upper limit on P_{rot} can be calculated. We verify that most of the measured P_{rot} ’s are consistent with their implied upper limits, and argue that exceeding this limit should arouse suspicion (Sect. 4.3). We also show P_{rot} correlates with $pEW'_{\text{H}\alpha}$ in a way that could help identify some types of spurious periods (Sect. 4.4). Informed by these lessons, we devise a framework to choose the most reasonable P_{rot} for each star and assign a confidence rating based on available information (Sect. 4.5). We show the dispersion among multiple measurements and discuss typical errors as a function of P_{rot} length (Sect. 4.6).

4.1. Rotation periods from the literature

Since the CARMENES survey sample consists chiefly of nearby stars, many have been monitored as part of photometric and spectroscopic surveys in addition to the ones presented here. For 241 stars in our sample, we found at least one, and often multiple period measurements in the literature. Our main references include P_{rot} catalogs from photometry (Kiraga & Stepień 2007; Hartman et al. 2011; Irwin et al. 2011; Kiraga 2012; Newton et al. 2016b, 2018; Suárez Mascareño et al. 2016; Oelkers et al. 2018; Díez Alonso et al. 2019; Medina et al. 2020, 2022; Irving et al. 2023; Pass et al. 2023)¹⁰, spectroscopic indicators (Suárez Mascareño et al. 2015, 2017b, 2018; Lafarga et al. 2021)¹¹, spectropolarimetry (Morin et al. 2008, 2010; Donati et al. 2008, 2023; Hébrard et al. 2016; Moutou et al. 2017; Fouqué et al. 2023), as well as planet discovery papers, which sometimes take hybrid approaches via combined analysis of diverse types of data sets. All literature periods and their references are given in Table C.2.

4.2. Rotation periods derived in this work

Following Sect. 3, we recovered periodicities for 129 stars in our sample. Of these, 89 have at least one independent measurement from the literature. It is instructive to compare these periods, as

¹⁰ We considered A, B, and U-rotators in Newton et al. (2016b, 2018), where ‘A’ and ‘B’ denote reliable periods and ‘U’ represents uncertain.

¹¹ For stars from Lafarga et al. (2021), we only considered those for which at least two activity indicators exhibit periodicity with $\text{FAP} < 0.1\%$ consistent to within 15%.

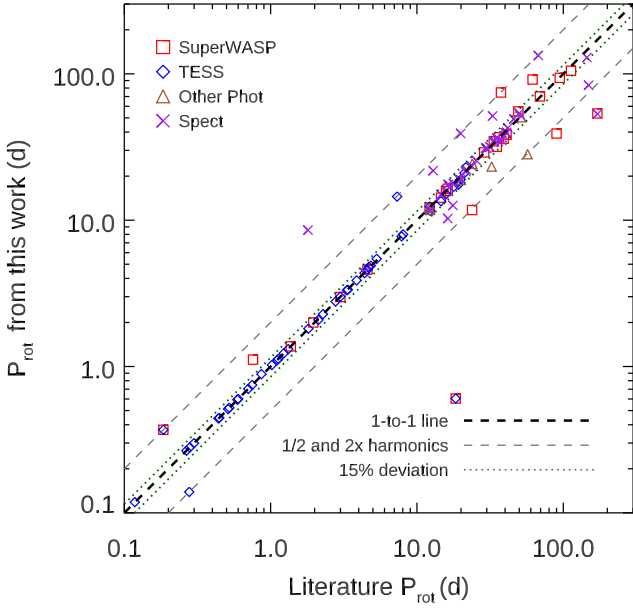


Fig. 3. Comparison between P_{rot} 's determined in this work and from the literature for stars in common. The red squares, blue diamonds, brown triangles, and purple 'X's represent periods from SuperWASP, TESS, other ground-based photometry, and spectroscopic indicators, respectively. The majority of periods are consistent with each other and are found directly on the one-to-one line (black dashed line) or within 15% (green dotted line). The clear outliers from the 1-to-1 correspondence, some of which are obvious 1/2 \times and 2 \times harmonics (grey dashed lines), are discussed in Appendix A.1. Note that some stars have periods determined from independent data sets in this work.

in Fig. 3. For simplicity, in the case where multiple periods have been published, we plot the one deemed most reasonable (i.e., consistent with other periods and activity signatures).

While most P_{rot} 's from this work are in excellent agreement with the literature, some of them deviate from the one-to-one relation by more than 15%. Of these, 7 are likely harmonics of each other and 12 are otherwise discrepant. The discrepant values are most often associated with the chromospheric activity indicators, suggesting that these periods may be less reliable than their photometric counterparts and should be used with more caution. We discuss these outliers individually in Appendix A.1. Therein we also document our reasoning for picking the most plausible period when presented with multiple measurements.

The simplification of using one literature P_{rot} per star in this comparison entails that not every discrepancy with and between the literature values can be fully described in the text. This subsection and the outlier list in Appendix A.1 are meant to give a representative view of the types of disagreements that occur. We direct the reader to Sect. 4.5 to see how contesting periods are evaluated in this work to help determine the most recommended value, and to Sect. 4.6 for a discussion on the general level of consistency in independent period measurements and its implications.

4.3. Consistency with $v \sin i$

We compare the P_{rot} 's for the CARMENES sample against the upper limits set by resolved $v \sin i$ measurements, where available (i.e., predominantly for fast rotators), together with the R_* , determined from effective temperature (T_{eff}) and bolometric luminosity (L_{bol}) measurements according to the methods

of Schweitzer et al. (2019). Such a comparison gives an independent indication of the plausibility of the documented P_{rot} 's for the fastest rotators in the sample. The relation between P_{rot} , $v \sin i$, and R_* is given by Eq. (3), by which we also define the quantity $P_{\text{rot,max}}$:

$$P_{\text{rot}} \leq \frac{P_{\text{rot}}}{\sin i} = \frac{2\pi R_*}{v \sin i} \equiv P_{\text{rot,max}}. \quad (3)$$

The majority of our $v \sin i$ values were uniformly measured from high-resolution CARMENES spectra ($R \sim 90\,000$) by Reiners et al. (2022), taking into account line broadening effects such as the Zeeman effect. Since $v \sin i$ values $\leq 2 \text{ km s}^{-1}$ cannot be reliably recovered in these spectra (Reiners et al. 2018b), we replaced all $v \sin i$ with nominal values below 2 km s^{-1} with an upper limit of 2 km s^{-1} and did not use them for computing $P_{\text{rot,max}}$. We assigned an uncertainty of at least 2 km s^{-1} or 10% of the measured value, whichever is larger, to capture modelling errors in rotation profile, limb darkening, instrumental broadening and turbulence. For stars without a $v \sin i$ in Reiners et al. (2022), we used values from Reiners et al. (2018b), where available. For J04173+088, we used the $v \sin i$ measured by Kesseli et al. (2018). We also discarded all $v \sin i$ measurements of known double-lined spectroscopic binaries (SB2's).

From the same spectra, Marfil et al. (2021) measured T_{eff} using spectral synthesis fitting. L_{bol} values were computed following the methodology of Cifuentes et al. (2020) using the latest *Gaia* eDR3 data (Gaia Collaboration 2021). R_* was then derived via the Stefan-Boltzmann Law combining T_{eff} and L_{bol} . In general, stellar mass (M_*) was calculated using a mass-radius relation given by Schweitzer et al. (2019), which is anchored in eclipsing binaries. Since the fast rotators are predominantly young and active, inferring robust stellar parameters from spectra is more challenging and errors in T_{eff} could affect the accuracy of R_* for this subsample. We mitigated this effect for the set of stars which we could assign to nearby young moving groups (and therefore estimate an age) based on their Galactic kinematics (Cardona et al. 2022). For those stars, we reevaluated their M_* and T_{eff} using their bolometric luminosities and PARSEC isochrones (Bressan et al. 2012) for the corresponding ages. We derived the radii from these parameters, again via the Stefan-Boltzmann Law. Since in this case R_* is model-dependent and only indirectly measured, a comparison against the measured P_{rot} values is in a sense also a consistency check for the stellar radius values listed for this sample. For known SBs in the sample as reported by Baroch et al. (2018, 2021), we adopted the estimated mass and radius of the primary component in computing $P_{\text{rot,max}}$, since we assumed that the measured rotation period can be attributed to the brighter companion. Table C.1 tabulates the $v \sin i$, R_* , M_* , and $P_{\text{rot,max}}$ for this sample. The typical formal uncertainty on R_*/R_{\odot} and M_*/M_{\odot} are 0.01–0.03.

Figure 4 plots the measured P_{rot} , either from this work or by other authors, against $P_{\text{rot,max}}$. Also shown as upper error bars are the 1σ 'tolerance' on $P_{\text{rot,max}}$, calculated from replacing $v \sin i$ and R_* in Eq. (3) with $v \sin i - \delta v \sin i$ and $R_* + \delta R_*$, respectively. The vast majority of stars exhibit fully consistent measurements, meaning $P_{\text{rot}} < P_{\text{rot,max},1\sigma}$. The few outliers marked by thick black circles are discussed in Appendix A.2, where we argue that all the significantly disagreeing periods are suspect.

4.4. Correlation with $pEW'_{\text{H}\alpha}$

H α emission is a potent chromospheric activity indicator in M dwarfs. Using CARMENES spectra for this sample, Schöfer et al. (2019) have uniformly characterized the amount

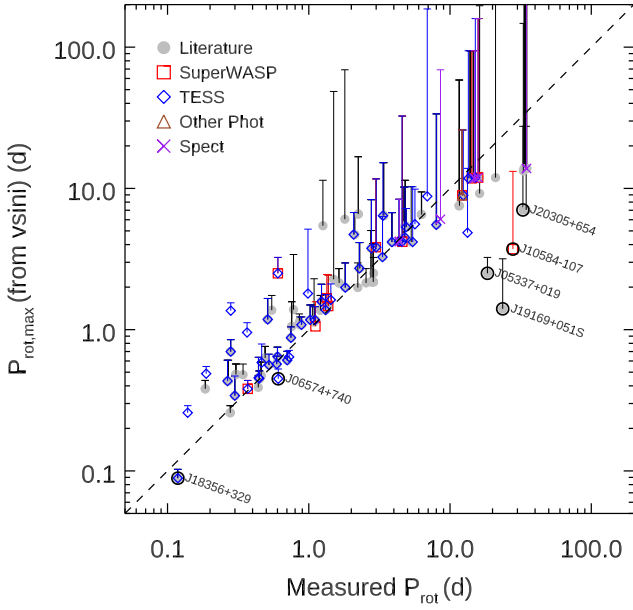


Fig. 4. Comparison between measured P_{rot} (from photometric or spectroscopic time series) and expected maximum P_{rot} from $v \sin i$ and R_* . Error bars mark the 1σ tolerance on $P_{\text{rot,max}}$ based on the uncertainties in $v \sin i$ and R_* . Points falling in the region below the 1-to-1 line (dashed) have contradicting P_{rot} , $v \sin i$ and R_* measurements. Those that fall significantly below (i.e., outside the 1σ error) are marked with a black circle and discussed in Appendix A.2.

of $H\alpha$ emission normalized by a quiescent reference star in the corresponding spectral type. The result is a metric defined as the $H\alpha$ pseudo-continuum width with spectral subtraction, $pEW'_{H\alpha}$, which is straightforward to measure and should correlate with P_{rot} . The $pEW'_{H\alpha}$ values for our sample are given in Table C.1.

Figure 5 compares the P_{rot} measurements available for this sample against $pEW'_{H\alpha}$, showing the overall expected trend whereby stronger $H\alpha$ emission (i.e., larger negative value) is associated with faster rotators. Stars with $pEW'_{H\alpha} \lesssim -0.3 \text{ \AA}$ (i.e., defined to be ‘ $H\alpha$ active’ by Schöfer et al. 2019) tend to have rotation periods shorter than 10 d, whereas stars with $pEW'_{H\alpha} \sim 0$ typically have rotation periods longer than 10 d. While it appears not uncommon for stars with $P_{\text{rot}} > 10 \text{ d}$ to exhibit $H\alpha$ in emission, very few stars with $pEW'_{H\alpha} > -0.3 \text{ \AA}$ are rapid rotators with $P_{\text{rot}} < 10 \text{ d}$. In fact, almost all of the points in the lower-left quadrant, representing supposed fast-rotators which appear to be $H\alpha$ -inactive, are likely spurious. We discuss them under Appendix A.3.

4.5. Best adopted rotation periods

The situation where multiple disagreeing periods are attributed to one given star is not uncommon. The fact that individual P_{rot} measurements do not always withstand scrutiny attests to persistent challenges in performing such measurements, as discussed in Sect. 4.6. Our goal is to recommend one single P_{rot} to adopt for each star in the CARMENES sample, and provide an indication of its reliability. In assembling our catalog, we were sometimes confronted with the dilemma of having to select the most likely P_{rot} value out of several conflicting possibilities, or one that is at odds with activity signatures in the absence of alternative options. To make the most informed evaluation on the veracity of a given P_{rot} , we developed a framework for leveraging multiple pieces of information.

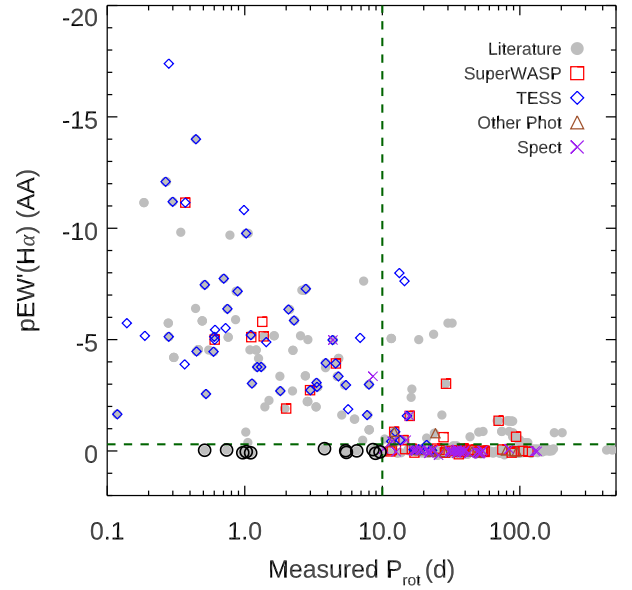


Fig. 5. $H\alpha$ pseudo-equivalent width from Schöfer et al. (2019) versus measured P_{rot} . Symbols as in Fig. 4. The dashed green lines delineate $pEW'_{H\alpha} = -0.3 \text{ \AA}$ and $P_{\text{rot}} = 10 \text{ d}$. Points to the lower-left of these bounds, marked with black circles, are considered to be outliers and discussed in Appendix A.3.

There are many possible approaches to assess period fidelity. Drawing from our investigations in Sects. 4.2, 4.3, and 4.4, we choose to use three pieces of information, where available, in order of priority: (1) agreement with other measurements; (2) consistency with $v \sin i$; (3) consistency with $pEW'_{H\alpha}$.

For each P_{rot} measurement, we assign a rating describing its likelihood to be correct on a coarse scale: ‘secure’ (‘S’), ‘provisional’ (‘P’), and ‘debated’ (‘D’) based on whether there is independent evidence supporting or contradicting it. Each P_{rot} measurement is by default ‘provisional’ unless one of the following applies:

1. If the P_{rot} agrees (or disagrees) with the majority of other independent P_{rot} measurements¹² for the same star within (or outside) 15%, then it is upgraded to ‘secure’ (or downgraded to ‘debated’). Values that are obvious harmonics are treated as positive supporting evidence. If no other P_{rot} measurements are available, then
2. Check plausibility with $v \sin i$. A strong agreement ($P_{\text{rot}} \lesssim P_{\text{max},1\sigma} \lesssim 30 \text{ d}$) leads to a ‘secure’ designation. A strong disagreement ($P_{\text{rot}} > P_{\text{max},1\sigma}$) leads to a ‘debated’ designation. If $v \sin i$ is not measured, then
3. For $P_{\text{rot}} < 10 \text{ d}$, $pEW'_{H\alpha} < -0.3 \text{ \AA}$ leads to a ‘secure’ designation, whereas $pEW'_{H\alpha} > -0.3 \text{ \AA}$ leads to a ‘debated’ designation.

Based on these ratings, a single ‘best’ known period ($P_{\text{rot,best}}$) was assigned to each star where at least one period measurement is available. We take the period with the best rating (‘secure’ > ‘provisional’ > ‘debated’). In cases where multiple periods are tied, we generally give precedence to photometric periods from this work. After this, we use the following hierarchy of preferred

¹² The literature measurements are independent to varying degrees. While some works are based on entirely separate observations, others have performed independent analyses of the same data sets, for example DA19’s use of the MEarth archival data, on which the periods from Irwin et al. (2011), Newton et al. (2016b), and Newton et al. (2018) are also based.

periods: periods from DA19 (which was the first comprehensive study for this sample), other photometric surveys from the literature, planet discovery papers, spectroscopic indicators from this work and the literature, and spectropolarimetry. The only periods we exclude from becoming $P_{\text{rot,best}}$ are those of U-rotators from this work and from Newton et al. (2016b, 2018), the ‘*’-rotators of Fouqué et al. (2023), the ‘marginal detections’ of Donati et al. (2023), which are deemed by the authors themselves to be uncertain, as well as those from Oelkers et al. (2018), who presented variability periods (<50 d) for a large sample ($\sim 5 \times 10^4$) of stars from the KELT survey, in which many are only ‘possible rotation periods’ that did not undergo individual vetting. We noticed that Oelkers et al. (2018) often reported the 1-day aliases of existing period measurements. These periods are valuable as supporting evidence for other period measurements, in the same way as the U-rotators, but not reliable enough to stand alone.

In total, there are 166 stars whose adopted periods have a high likelihood of being correct (‘secure’ or ‘S’), 68 stars whose periods are tentative (‘provisional’ or ‘P’), and 27 stars whose periods are disputed (‘debated’ or ‘D’). The ‘provisional’ periods are most often long and difficult to refute with activity signatures, while also being difficult to confirm with multiple measurements. A typical ‘debated’ period is a short one derived for a star that is not spectroscopically active.

The final adopted periods, $P_{\text{rot,best}}$, are given in Table C.1. These are used for the analyses in Sect. 5. For an estimate of the period errors, we refer to Sect. 4.6. All literature periods that contributed to the assessment are given in Table C.2.

4.6. Empirical estimates of P_{rot} error

The existence of debated period measurements is a symptom of broader challenges with determining accurate stellar rotation periods. The detectability and reliability of a detected rotation signal are affected by many interconnected factors including:

- The characteristics and quality of the data sets (e.g., time and duration of observations, sampling strategy, data precision). For example, ground-based surveys are plagued by poorer precision, weather, and aliasing, while space-based surveys tend to have limited time baselines;
- The choice of analysis methods and thresholds (e.g., Aigrain et al. 2015). For example, authors working independently with the same data set can still sometimes obtain discrepant results, such as Newton et al. (2016b) and DA19 on MEarth photometry, or Fouqué et al. (2023) and Donati et al. (2023) on SPIRou spectropolarimetry;
- The astrophysical behaviour of the star itself. Some example processes that can affect P_{rot} determination are differential rotation (e.g., Reinhold et al. 2013), spot configurations and lifetimes (e.g., Giles et al. 2017), and variability unrelated to rotation. The evolution of surface active regions over time can affect modulation amplitudes (e.g., Irwin et al. 2011) and lead to intrinsically quasi-periodic variations (e.g., Angus et al. 2018). An example from our sample is shown in Fig. 6 for the star J18174+483, where five seasons of SuperWASP observations spanning six years reveal evolving morphology, amplitude and phase, visible against the backdrop of the global best-fit sinusoidal signal (15.8 d). The best-fit periods differ slightly from season to season, varying between 15.6 d and 17 d;
- The nature and strength of the physical link between the modulating observable and stellar rotation (see discussion in, e.g., Lafarga et al. 2021; Schöfer et al. 2022). For example, stellar activity can manifest differently in photospheric

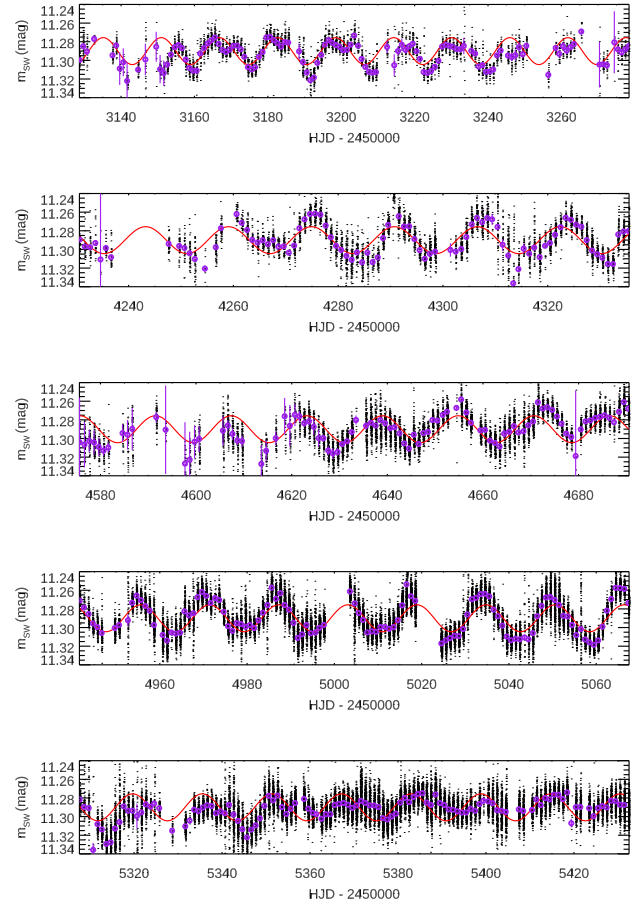


Fig. 6. SuperWASP light curve of J18174+483 in five seasons spanning six years. The best-fit sinusoidal signal to the global data set (15.83 d) is plotted as the red curve. Purple circles are daily-binned data points.

spots than in chromospheric lines, impacting their variation patterns and sensitivity to rotation.

These considerations complicate the assignment of appropriate errors to a given period measurement (e.g., Irwin et al. 2011; Newton et al. 2016b). Authors who do report P_{rot} errors estimate them using a variety of methods, though it is unclear to what extent these formal errors adequately capture the complex and varied factors affecting the retrieved period values. For instance, one popular measure of P_{rot} error uses the breadth of the periodogram peak, which would be misleading if multiple peaks are present (Newton et al. 2016b).

When multiple independent P_{rot} measurements are made for a given star, their level of disagreement provides an empirical measure of the uncertainty. Using statistical dispersion as a proxy for level of disagreement, we investigate the behaviour of this empirical error (σ_{emp}) for our sample. For each of our sample stars with more than one period measurement available (from the literature or from this work), we compute the standard deviation among this set of periods. To minimize the outsized effects of harmonics and aliases on our metric, we replaced periods that are obvious $2\times$ or $1/2\times$ harmonics or daily aliases of the adopted period $P_{\text{rot,best}}$ (i.e. within 15%) with the harmonic or alias value closest to $P_{\text{rot,best}}$. A few of the period discrepancies may also be attributed to yearly aliasing, although for this exercise we left them as they are.

In Fig. 7 we plot σ_{emp} against $P_{\text{rot,best}}$ for 169 stars. A strong positive correlation is evident: larger P_{rot} ’s have larger dispersions in their measurements. In general, faster rotators

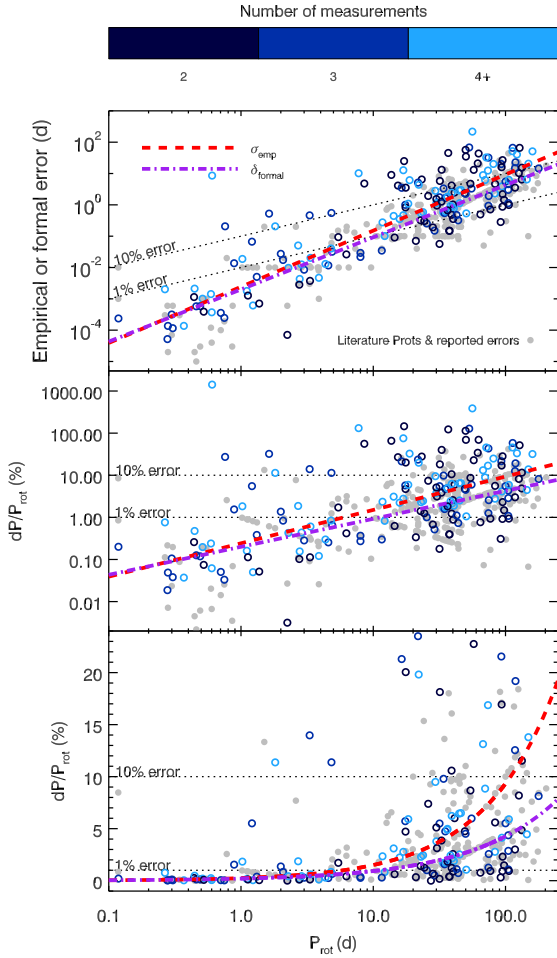


Fig. 7. Measures of error as a function of P_{rot} . Blue unfilled circles plot the ‘empirical’ dispersion σ_{emp} , i.e., standard deviation of the measured periods, colour-coded by the number of measurements (see colour bar). Grey filled circles represent ‘formal’ errors δ_{formal} , as reported in the literature. Top: σ_{emp} versus $P_{\text{rot,best}}$ (blue) and δ_{formal} versus reported P_{rot} (grey); middle: fractional error versus P_{rot} , where fractional error is obtained by dividing σ_{emp} or δ_{formal} (collectively termed ‘ dP ’) by P_{rot} . Bottom: same as the middle, but with the y-axis shown on a linear scale. The best-fit power laws are plotted for σ_{emp} (red dashed, as given in Eq. (4)) and δ_{formal} (purple dot-dashed, as given in Eq. (5)). The black dotted lines depict constant fractional errors of 10% and 1% for comparison. Note that the bottom panel has restricted vertical plotting range in order to show the difference in the two power laws. Points beyond the vertical range are not shown.

(<10 d) display a high level of consistency among independent measurements, with typically $\leq 1\%$ dispersion. Among the 116 slower rotators (≥ 10 d), the median dispersion is modest at $\sim 5\%$. However, large outliers are also common: 38 stars have fractional dispersions $\geq 10\%$, and 28 have dispersions $\geq 20\%$. Figure 8 displays the cumulative fraction of stars exceeding a range of thresholds in fractional dispersion for <10 d, 10–100 d, and ≥ 100 d rotators.

The best-fit power law gives an empirical estimate of the typical error in an individual P_{rot} measurement as a function of P_{rot} value:

$$\sigma_{\text{emp}}(P_{\text{rot}}) = 9.24 \left(\frac{P_{\text{rot}}}{100 \text{ d}} \right)^{1.79} \Rightarrow \frac{dP_{\text{rot,emp}}}{P_{\text{rot}}} = 9.24\% \left(\frac{P_{\text{rot}}}{100 \text{ d}} \right)^{0.79}, \quad (4)$$

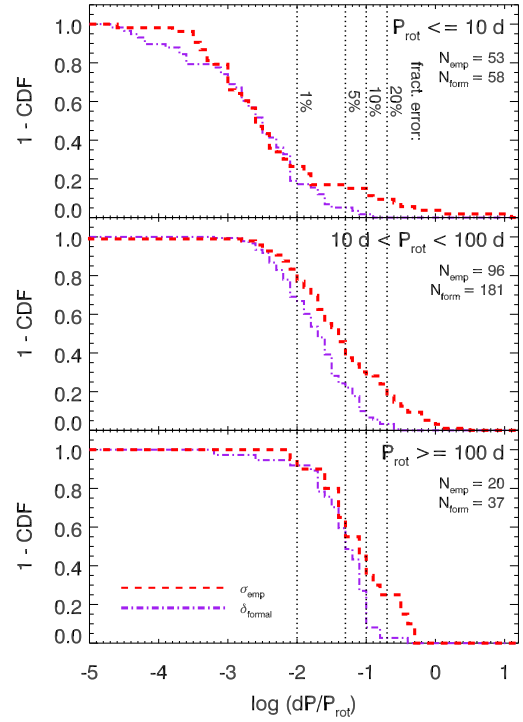


Fig. 8. Reverse cumulative distribution of fractional period errors: comparison between ‘empirical’ (σ_{emp} , red dashed) and ‘formal’ errors (δ_{formal} , purple dot-dashed). Top: for $P_{\text{rot}} \leq 10$ d; middle: for $10 < P_{\text{rot}} < 100$ d; bottom: for $P_{\text{rot}} \geq 100$ d. The number of data points in each bin are given as N_{emp} for the empirical dispersion and N_{form} for the formal error distribution.

where $dP_{\text{rot,emp}}/P_{\text{rot}}$ denotes the fractional period error. According to Eq. (4), the average fractional error reaches above 10% for very slow rotators with $P_{\text{rot}} > 109$ d. However, since the dispersion on a number of ≥ 10 d periods already far exceed the 10% (see Figs. 7 and 8), single P_{rot} measurements in the 10–100 d range can also be more unreliable than Eq. (4) would suggest. Additional measurements are important for verification, and are especially relevant for disentangling between harmonics and aliases, whose effects were filtered out in this exercise. Even in the absence of harmonics and aliases, Eq. (4) likely gives a conservative representation of dispersion, because our assumption that the P_{rot} values from the literature are independent is not completely valid (e.g., authors may use the same data sets, and published results can be at least somewhat influenced by the knowledge of one another). Interestingly, the error-to- P_{rot} relation characterized by Eq. (4) is very comparable to that found by Irwin et al. (2011) using injection-retrieval simulations in MEarth data (see note ‘g’ under Table 1 therein).

For comparison, in Fig. 7 we overplot 276 literature P_{rot} values with their reported formal errors δ_{formal} collected for this sample. The best-fit power law,

$$\delta_{\text{formal}}(P_{\text{rot}}) = 4.27 \left(\frac{P_{\text{rot}}}{100 \text{ d}} \right)^{1.66} \Rightarrow \frac{dP_{\text{rot,formal}}}{P_{\text{rot}}} = 4.27\% \left(\frac{P_{\text{rot}}}{100 \text{ d}} \right)^{0.66}, \quad (5)$$

characterizes the average formal error as a function of P_{rot} , and is slightly shallower than our empirical relation (Eq. (4)). While nearly indistinguishable at 1 d, the discrepancy grows with P_{rot} such that, at 100 d, σ_{emp} exceeds δ_{formal} by more than a factor of two. Furthermore, as shown in Fig. 8, the share of stars with large period errors appears to be also underestimated compared to reality. In this sample, only 3% of periods above 10 d have

formal fractional errors above 20%, compared to 24% with fractional measurement dispersions greater than 20%. In sum, we find that formal period errors tend to be somewhat more optimistic than the actual dispersion of measurements, especially for slower rotators with $P_{\text{rot}} \gtrsim 10$ d.

Since Eq. (4) is by construction derived using an ensemble of periods agnostic of the data, method, and stellar properties, it is not necessarily applicable to arbitrary data sets with very specific characteristics. Nevertheless, since we effectively ‘marginalize’ over all the factors that could affect the measurement, Eq. (4) has the advantage of being a very general and reasonable representation of uncertainty in the absence of a more principled error analysis. Therefore, we adopt $\sigma_{\text{emp}}(P_{\text{rot}})$ given in Eq. (4) as our estimate of period error in this work, while stressing that periods $\gtrsim 10$ d can be more erroneous than this equation would suggest.

Equation (4) also provides an instructive relation between the period uncertainty and period value. Intuitively, shorter periods should be much easier to measure because they undergo more cycles (for a fixed observing time baseline) and are associated with larger variability amplitudes and more stable spot configurations (measured in number of rotations, see e.g., Basri et al. 2022), which are favourable conditions to unambiguous and more precise detections. Moreover, shorter periods are more accessible by space-based missions, whose low noise, high cadence, and continuous monitoring capabilities facilitate the detailed characterization of stellar variability.

However, the short-period advantage is difficult to scale up to the $\gtrsim 10$ d-class rotators. Longer periods are challenging to measure because of the inherent difficulties involved in carrying out a long-term all-sky survey. With the exception of the original *Kepler* mission (which monitored a small patch of the sky for four years), long time baseline surveys typically operate from the ground, where long-term stability in photometry cannot be guaranteed for months and years. In addition to day-to-night cycles and seasonal visibility, ground-based observations are also affected by weather conditions and moon phases, all of which lead to non-uniform sampling, aliasing, and data points of varying quality, hindering the precise characterization of low-amplitude variability.

The increased spread in measurements at larger periods could also be reflecting trends in differential rotation. It has been shown that slower rotators tend to have stronger relative differential rotation (e.g., Donahue et al. 1996; Reiners & Schmitt 2003; Reinhold et al. 2013), which could further contribute to blurring their measured P_{rot} . Under this interpretation, P_{rot} itself is not a unique quantity, and its ‘error’ characterizes the dispersion in latitudinal rotation rates. This hypothesis should be tested in a data set with more uniform and widespread coverage and analysis techniques, as has been done with the *Kepler* sample (e.g., Reinhold et al. 2013).

5. Discussion

5.1. Rotation-activity relations

Magnetic dynamos, powered by rotation, operate in stars and give rise to global magnetic fields that transform convective energy in the stellar interior to heat the surface, including the chromosphere and corona. While the exact process by which this happens is still not completely understood (see, e.g., Charbonneau 2005; Kochukhov 2021; Reiners et al. 2022), the theory may be constrained by a number of well-defined correlations between rotation rate of a star and energy output from the chromosphere and corona, which have been directly observed. The mass-dependence of such relations, in particular across the mass boundary at about $0.35 M_{\odot}$, is of especial interest due to

the theoretical change in the dynamo mechanism for fully convective stars.

Proxies for chromospheric activity include emission in the $H\alpha$ and Ca II H&K lines, while X-ray flux tracks coronal emission. In stars later than $\sim F$ -type, it has long been demonstrated that faster rotation maps into greater non-thermal flux (e.g., Pallavicini et al. 1981; Noyes et al. 1984). Further investigation uncovered two distinct regimes for this correlation: an unsaturated regime where the luminosity of the activity indicator increases monotonically with rotation rate, and a saturated regime where the bolometrically normalized luminosity of the activity indicator stays roughly constant (e.g., Pizzolato et al. 2003; Mamajek & Hillenbrand 2008; Wright et al. 2011; Reiners et al. 2014). The saturation regime sets in below a certain threshold period, P_{sat} . The correlation is characterized by the slope in each regime, the break point between the two regimes (i.e., P_{sat}), and any systematic or random scatter around the relation. These relationships have also been studied extensively for M dwarfs for which rotation periods have been measured (L_X : Stelzer et al. 2016; González-Álvarez et al. 2019; Magaúda et al. 2020; $L_{H\alpha}$: Newton et al. 2017; L_{Ca} : Astudillo-Defru et al. 2017a; Suárez Mascareño et al. 2018; Boudreaux et al. 2022).

Magnetic heating is thought to be the underlying driver of non-thermal emission. Recently, Reiners et al. (2022) elucidated the mechanism responsible for activity–rotation relations. They measured the average surface magnetic field strengths (B) for a large subset of M dwarfs from the CARMENES survey, by using Zeeman broadening modelling of high-quality spectra. They demonstrated that $\langle B \rangle$ behaves identically to that of other activity indicators with respect to rotation. Saturation in magnetic activity is therefore a consequence of saturation in the magnetic field as it reaches the kinetic energy limit. Furthermore, non-thermal emission from the chromosphere and corona directly trace the magnetic flux, which is proportional to rotation rate.

In Fig. 9 we show several well-known rotation-activity relations for the CARMENES M dwarf sample in terms of the Rossby number, $Ro \equiv P_{\text{rot}}/\tau_{\text{conv}}$. We calculated the convective overturn time τ_{conv} as a function of $(V - K_s)$ colour using the prescription of Wright et al. (2018), which is calibrated for the entire range of M dwarf spectral types. Johnson V and Two-Micron All-Sky Survey K_s magnitudes were taken from Cifuentes et al. (2020) and references therein (see also Appendix B). We note that other calibrations for τ_{conv} are available and systematically offset from one another (see Appendix B), and that the exact prescription choice may affect the quantitative details of the activity–rotation relations (Magaúda et al. 2020). The points in Fig. 9 are colour-coded by stellar mass, divided into bins $>0.35 M_{\odot}$, $0.20\text{--}0.35 M_{\odot}$, and $<0.2 M_{\odot}$, the latter two corresponding to fully convective stars.

All activity indicator measurements for this sample were compiled from the literature as described below. To these values we fitted classical rotation–activity relations in the following broken-power-law form (unless otherwise specified) where non-zero slopes are allowed in both the saturated and unsaturated regimes:

$$\text{Activity Indicator} = \begin{cases} A(Ro/Ro_{\text{sat}})^{\beta_{\text{sat}}} & \text{for } Ro < Ro_{\text{sat}} \\ A(Ro/Ro_{\text{sat}})^{\beta_{\text{unsat}}} & \text{for } Ro > Ro_{\text{sat}} \end{cases} \quad (6)$$

Here A is a normalization constant, Ro_{sat} is the saturation Rossby number, and β_{sat} and β_{unsat} are slopes in the saturated and unsaturated regimes, respectively. The fits were performed using the Markov Chain Monte Carlo fitting package *emcee*

Table 2. Best-fit activity–rotation parameters.

M_\star range	N_\star	$\log_{10}(A)$	$\log_{10}(\text{Ro}_{\text{sat}})$	β_{sat}	β_{unsat}	$\log_{10}(f)$	Lit. Ro_{sat}	Lit. β_{sat}	Lit. β_{unsat}	Ref.
L_X/L_{bol} :										
Whole sample	108	$-3.16^{+0.11}_{-0.10}$	$-0.78^{+0.07}_{-0.08}$	$-0.04^{+0.09}_{-0.09}$	$-1.90^{+0.17}_{-0.18}$	$+0.04^{+0.06}_{-0.06}$	0.13 (fixed)	$-0.16^{+0.03}_{-0.03}$		Rei14
$>0.35 M_\odot$	53	$-3.23^{+0.11}_{-0.10}$	$-0.69^{+0.03}_{-0.05}$	$-0.08^{+0.12}_{-0.11}$	$-2.96^{+0.16}_{-0.17}$	$-0.11^{+0.07}_{-0.06}$				
$\leq 0.35 M_\odot$	55	$-3.01^{+0.16}_{-0.15}$	$-0.38^{+0.07}_{-0.08}$	$+0.02^{+0.10}_{-0.10}$	$-3.55^{+0.53}_{-0.47}$	$-0.04^{+0.08}_{-0.07}$				
$L_{\text{H}\alpha}/L_{\text{bol}}$:										
Whole sample	176	$-3.96^{+0.06}_{-0.05}$	$-0.88^{+0.05}_{-0.06}$	$-0.08^{+0.05}_{-0.04}$	$-1.29^{+0.06}_{-0.06}$	$-0.21^{+0.04}_{-0.03}$	$0.21^{+0.02}_{-0.02}$	0 (fixed)	$-1.7^{+0.1}_{-0.1}$	New17
$>0.35 M_\odot$	74	$-4.00^{+0.15}_{-0.14}$	$-0.92^{+0.11}_{-0.13}$	$-0.23^{+0.16}_{-0.15}$	$-1.36^{+0.07}_{-0.07}$	$-0.20^{+0.06}_{-0.05}$				
$0.2-0.35 M_\odot$	58	$-3.91^{+0.06}_{-0.06}$	$-0.91^{+0.10}_{-0.10}$	$-0.11^{+0.05}_{-0.05}$	$-1.12^{+0.09}_{-0.11}$	$-0.39^{+0.06}_{-0.05}$				
$\leq 0.2 M_\odot$	44	$-3.98^{+0.13}_{-0.12}$	$-0.62^{+0.14}_{-0.14}$	$-0.02^{+0.08}_{-0.07}$	$-1.73^{+0.28}_{-0.40}$	$-0.17^{+0.08}_{-0.06}$				
$\leq 0.35 M_\odot$	102	$-3.94^{+0.06}_{-0.06}$	$-0.77^{+0.08}_{-0.08}$	$-0.06^{+0.04}_{-0.04}$	$-1.32^{+0.11}_{-0.12}$	$-0.28^{+0.05}_{-0.04}$				
R'_{HK} :										
$>0.35 M_\odot$ ^(a)	80	$-4.18^{+0.08}_{-0.08}$	$\log_{10}(0.13)$...	$-0.94^{+0.11}_{-0.11}$	$-0.30^{+0.05}_{-0.04}$				
$\leq 0.35 M_\odot$	43	$-4.23^{+0.10}_{-0.09}$	$-0.98^{+0.20}_{-0.18}$	$+0.41^{+0.13}_{-0.13}$	$-1.01^{+0.20}_{-0.26}$	$-0.36^{+0.07}_{-0.06}$				
$\langle B \rangle$:										
Whole sample	149	$+3.47^{+0.05}_{-0.04}$	$-1.01^{+0.06}_{-0.06}$	$-0.09^{+0.04}_{-0.04}$	$-1.00^{+0.05}_{-0.06}$	$-0.39^{+0.04}_{-0.03}$	0.13 (fixed)	$-0.11^{+0.03}_{-0.03}$	$-1.26^{+0.10}_{-0.10}$	Rei22
$\leq 0.35 M_\odot$	69	$+3.46^{+0.05}_{-0.05}$	$-0.81^{+0.16}_{-0.11}$	$-0.09^{+0.03}_{-0.04}$	$-1.01^{+0.12}_{-0.18}$	$-0.49^{+0.05}_{-0.05}$				

Notes. ^(a)This fit was done only in the unsaturated arm using a fixed $\text{Ro}_{\text{sat}} = 0.13$ and without the severe outlier J14257+236W.

References. Rei14: [Reiners et al. 2014](#); New17: [Newton et al. 2017](#); Rei22: [Reiners et al. 2022](#).

(Foreman-Mackey et al. 2013). We set uninformative priors on $\log(A)$, β_{sat} , and β_{unsat} , and imposed a flat prior on $\log(\text{Ro}_{\text{sat}}) \in [-2, 0]$. In addition to the reported formal errors on the measured activity indicator, we added a parameter $\log(f)$ in constructing the likelihood function to account for underestimated variance as a fixed fraction f of each activity indicator measurement, following standard procedures (see, e.g., [Newton et al. 2017](#); [Núñez et al. 2022](#)). We did not account for errors on Ro . The fits employed 32 walkers each taking 5000 steps, discarding the first 1000 steps. The best-fit parameters are given in Table 2. In this work, all instances of \log refer to the common logarithm in base 10.

X-rays. The X-ray measurements are from ROSAT 1RXS ([Voges et al. 1999](#)). We plot bolometric-normalized X-ray luminosity L_X/L_{bol} versus Ro relation for 113 stars in our sample. Of these, 108 stars have ‘S’ and ‘P’ period designations. For these stars we fitted Eq. (6) to L_X/L_{bol} .

We fitted to the whole sample as well as separately to partially convective ($>0.35 M_\odot$) and fully convective ($\leq 0.35 M_\odot$) M dwarfs. Figure C.5 shows an example of the posterior distribution for the whole sample fit. Table 2 displays these best-fit parameters and their 1σ errors (i.e., 16th and 84th percentiles of the posterior distributions) for each mass range considered. Figure 9 plots the corresponding relations for the partially convective ($>0.35 M_\odot$) and fully convective ($\leq 0.35 M_\odot$) M dwarfs. We overlay the relation shown in Fig. 3 of [Reiners et al. \(2014\)](#), which was based on a broader range of stellar masses, including predominantly sunlike stars. We note that [Reiners et al. \(2014\)](#) computed the empirical Ro based on [Wright et al. \(2011\)](#), which deviates from the [Wright et al. \(2018\)](#) version by up to -0.2 dex (see Fig. B.1).

In the saturated regime, all fits are compatible with a null slope, although across the convective mass boundary the slopes are $\sim 1\sigma$ apart. The early-M dwarfs show a slightly negative slope ($\beta_{\text{sat}} = -0.08 \pm 0.12$) consistent with that of [Reiners et al. \(2014\)](#) of -0.16 . However, the mid- and late-M dwarfs follow a slightly positive slope of $+0.02 \pm 0.10$, which is 2σ deviant from the slope of [Reiners et al. \(2014\)](#). A hint of this dichotomy is also visible in Fig. 4 of [Magaudá et al. \(2020\)](#) and extensively discussed in [Magaudá et al. \(2022a\)](#).

The break points marking the end of saturation also appears to have a significant mass dependence. For early-M’s, the decline in activity starts already at $\text{Ro}_{\text{sat}} \sim 0.2$, whereas for later-M’s it is close to $\text{Ro}_{\text{sat}} \sim 0.4$. [Magaudá et al. \(2020\)](#) found a very similar dependence for P_{sat} in the L_X-P_{rot} relation for M dwarfs. These values are significantly larger than the $\text{Ro}_{\text{sat}} = 0.13$ assumed by previous authors studying the $L_X-\text{Ro}$ relation ([Wright et al. 2011, 2018](#); [Reiners et al. 2014](#)). Since Ro_{sat} plays a role in calibrating the empirical τ_{conv} , this difference could be related to the offsets between various τ_{conv} parameterizations (see e.g., Appendix B). The slope in the unsaturated regime is about -3.0 for the early-M’s and -3.5 for the later-M’s, the latter being poorly constrained due to the relatively few data points available.

H α . Bolometric-normalized H α -luminosities were collected from [Newton et al. \(2017\)](#) and supplemented by [Schöfer et al. \(2019\)](#). Preference was given to the [Newton et al. \(2017\)](#) measurements for two reasons: (1) there are more stars in our full sample that have a $L_{\text{H}\alpha}/L_{\text{bol}}$ measurement from [Newton et al. \(2017\)](#) than from [Schöfer et al. \(2019\)](#); 209 versus 96¹³; (2) to facilitate comparison with the fitted activity–rotation relation of [Newton et al. \(2017\)](#). To put all measurements on the [Newton et al. \(2017\)](#) scale, we fitted a linear relation to the $\log(L_{\text{H}\alpha}/L_{\text{bol}})$ of 56 shared stars to derive a small correction that was applied to all the [Schöfer et al. \(2019\)](#) values¹⁴.

¹³ This difference is mainly due to the choice made by [Schöfer et al. \(2019\)](#) to compute the H α luminosity only for stars considered to be active, i.e., $pEW'_{\text{H}\alpha} < -0.3 \text{ \AA}$, effectively setting a floor at $L_{\text{H}\alpha}/L_{\text{bol}} \sim 10^{-5}$. In contrast, [Newton et al. \(2017\)](#) computed $L_{\text{H}\alpha}/L_{\text{bol}}$ also for stars exhibiting H α fluxes below this threshold. Therefore, they reached lower values of luminosity ratios ($\sim 10^{-6}$) and apparently probed the unsaturated regime to a greater extent.

¹⁴ The systematic deviation originates in differences in measurement methodologies. The two works used somewhat different zero-points: [Newton et al. \(2017\)](#) measured the excess emission with respect to the strongest observed H α absorption as a function of colour, whereas [Schöfer et al. \(2019\)](#) measured excess emission with respect to the slowest rotating star of the same spectral type. It is debated whether the H α line behaves in a monotonic way at low activity levels (e.g., [Cram & Mullan 1979](#)), and a good zero point may not even exist.

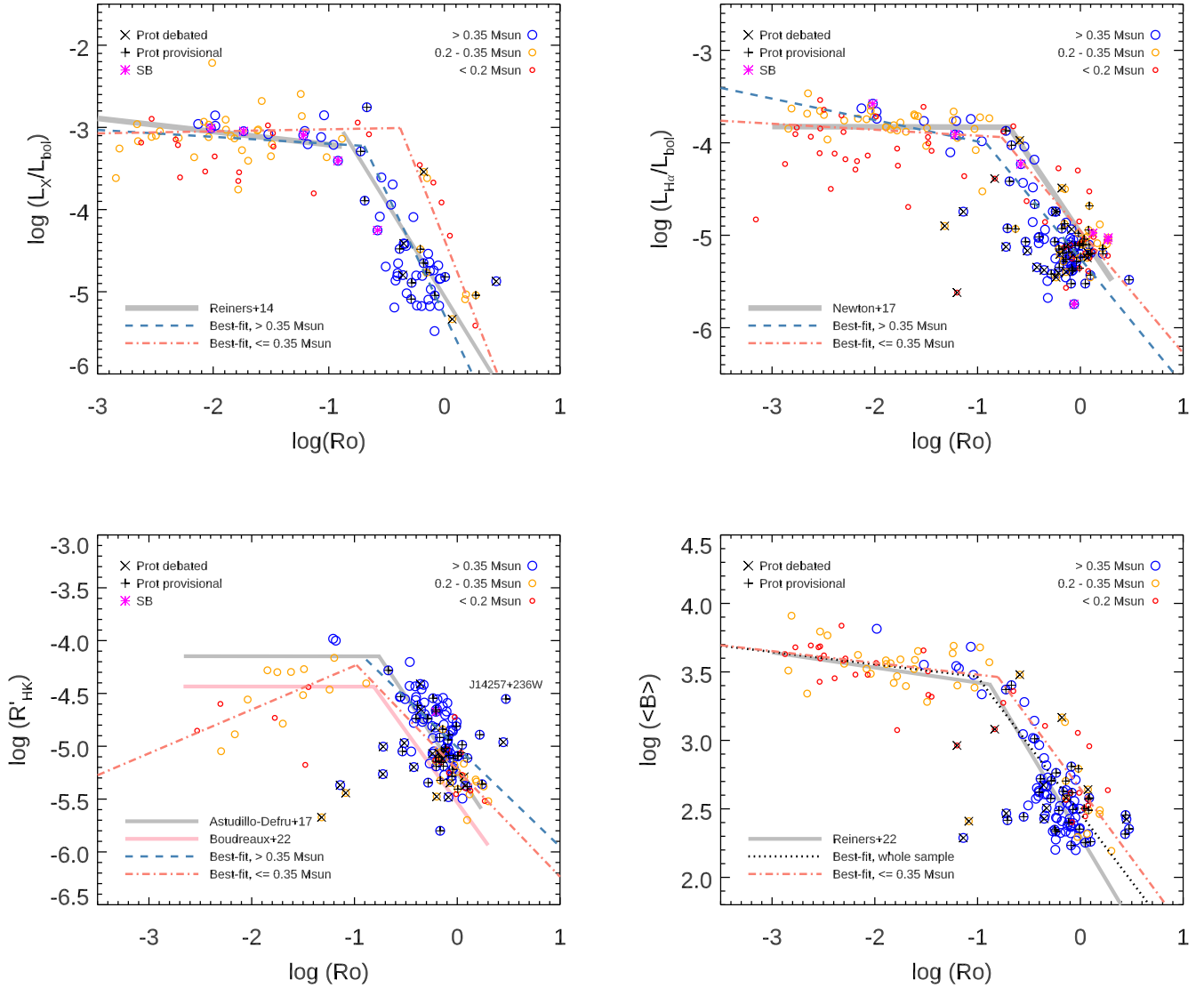


Fig. 9. Rotation–activity relations studied for our sample, as discussed in Sect. 5.1. Top left: normalized X-ray luminosity L_X/L_{bol} as function of the Rossby number Ro for 113 M dwarfs. The corresponding best-fit relation from Reiners et al. (2014) is plotted in thick grey lines. Top right: normalized H α luminosity $L_{H\alpha}/L_{\text{bol}}$ as function of Ro for 196 M dwarfs. The best-fit broken power-law relation from Newton et al. (2017) is displayed in grey. Bottom left: normalized Ca II H&K emission ($R'_{\text{HK}} \equiv L_{\text{Ca}}/L_{\text{bol}}$) as function of Ro for 144 stars. The marked outlier J14257+236W was not included in our fit. Best-fit relations from Astudillo-Defru et al. (2017a) and Boudreaux et al. (2022) are overplotted. Bottom right: average magnetic field strength $\langle B \rangle$ versus Ro for 162 stars. In all plots, earlier-, mid-, and later-type M dwarfs (i.e., $M_\star > 0.35 M_\odot$, $0.35 M_\odot > M_\star > 0.2 M_\odot$, $< 0.2 M_\odot$) are denoted by large blue, medium-sized orange, and small red circles, respectively. Stars with non-debated period values are fitted with broken power laws, shown in broken dashed lines in black (whole sample), blue ($> 0.35 M_\odot$), and green ($\leq 0.35 M_\odot$). Stars with debated periods are marked by black ‘X’s, and with provisional periods they are marked by black ‘+’s. Known SBs are represented by magenta asterisks. Where applicable, best-fit rotation-activity relations for subsamples within defined mass ranges are overlaid (black dotted lines: whole sample, blue dashed lines: $> 0.35 M_\odot$, red dash-dotted lines: $\leq 0.35 M_\odot$).

In Fig. 9 we plot 196 stars with both $L_{H\alpha}$ and P_{rot} determinations. In the same way as for X-ray, we fitted the relation from Eq. (6) to $L_{H\alpha}/L_{\text{bol}}$ for all stars except 20 whose periods have ‘D’ (debated) designations. We fit to the whole sample and the $> 0.35 M_\odot$ and $\leq 0.35 M_\odot$ subsets, Fig. 9 shows the functions corresponding to the medians of the parameter posteriors for the $> 0.35 M_\odot$ and $\leq 0.35 M_\odot$ fits. In addition, the fully convective sample was itself large enough such that we could further subdivide it into the mid- and late-M dwarfs across $0.2 M_\odot$ and still get convergent fits (not plotted). We used them to investigate any finer gradations in the mass-dependence of the fitted relations. The best-fit parameters for all five subsamples are given in Table 2. Overplotted in Fig. 9 is the relation given by

Newton et al. (2017), whose sample spans a similar mass range to ours. Note that Newton et al. (2017) computed Ro using the equations from Wright et al. (2011), which were not properly calibrated for fully convective stars.

The saturation regime presents a slight discrepancy from Newton et al. (2017). Their relation assumed a constant saturation emission level. In our overall sample, we find a slight downward slope of -0.08 ± 0.05 , formally incompatible with a null slope. The few early-M dwarfs on the saturation branch exhibit an even stronger downward trend (-0.23 ± 0.16). Though the uncertainties are much larger, it seems to suggest that chromospheric emission as traced by H α could have a weak Ro -dependence even upon saturation, similar to that seen in X-ray

and B -fields. On the other hand, the mid- and late-M dwarfs in the saturated regime have progressively milder slopes, mirroring the tentative trend observed in X-ray.

The best-fit saturation breakpoint in the early-M subsample is somewhat smaller ($Ro_{\text{sat}} \sim 0.12$) than that in the late-M subsample ($Ro_{\text{sat}} \sim 0.17$), the latter being comparable to $Ro_{\text{sat}} = 0.21 \pm 0.02$ from [Newton et al. \(2017\)](#). However, the slopes in the unsaturated arm are not as strong in our sample (about -1.3 to -1.4) as in [Newton et al. \(2017\)](#); -1.7 ± 0.1 therein). In general, it may be more difficult to interpret comparisons in the unsaturated regime, because the measurement of $H\alpha$ luminosity is more problematic and uncertainties may be large. Figure 7 in [Newton et al. \(2017\)](#) shows significant downward scatter in the tail end of the unsaturated branch, below $L_{H\alpha}/L_{\text{bol}} \sim 10^{-5}$, similar to here. Therefore, we do not assign too much meaning to the fit differences in the unsaturated regime.

Ca II H&K. Ca II H&K flux is commonly expressed with the metric R'_{HK} . R'_{HK} time series were measured for 200 stars in the CARMENES sample using assorted public archival spectra covering the blue wavelength ranges ([Perdelwitz et al. 2021](#)). For each star with multiple R'_{HK} measurements, we took the mean of its time series weighted by the errors as its R'_{HK} value. We plot R'_{HK} against Ro for 144 stars, of which 124 are deemed to have non-debated periods.

Since there are very few early-M dwarfs with measured R'_{HK} on the saturation branch, we fitted the two-arm rotation–activity relation Eq. (6) for R'_{HK} only to 43 fully convective M dwarfs. For the early-M dwarfs, we fitted the relation to the unsaturated arm¹⁵ using a fixed $Ro_{\text{sat}} \equiv 0.13$. Intriguingly, for the fully convective M dwarfs, we find a very significant upward trend with slope 0.41 ± 0.13 in the saturation regime, implying receding emission with faster rotation for the rapid rotators. If robust, this could be evidence of chromospheric supersaturation ([Christian et al. 2011](#)). However, the fact that this trend is not matched in $H\alpha$ or coronal emission suggests possible systematics in the measurement of R'_{HK} for these late-type fast rotators (see below as well as discussion in [Perdelwitz et al. 2021](#)).

Several previous works have explored the R'_{HK} –rotation relation for low-mass stars. [Astudillo-Defru et al. \(2017a\)](#) studied the R'_{HK} – P_{rot} relation in 38 predominantly early-type M dwarfs. On the other hand, [Boudreaux et al. \(2022\)](#) measured R'_{HK} for 53 fully convective M dwarfs with known rotation periods. In Fig. 9, we overplot the two relations, given by [Boudreaux et al. \(2022\)](#) in terms of R'_{HK} – Ro , based on [Wright et al. \(2018\)](#)’s $\tau_{\text{conv}}-(V-K_s)$ relation.

For rapid rotators with $P_{\text{rot}} < 10$ d (corresponding to $Ro \lesssim 0.14$), [Astudillo-Defru et al. \(2017a\)](#) found a constant $R'_{\text{HK}} = -4.045$. [Boudreaux et al. \(2022\)](#) showed that later-type M dwarfs have a notably lower Ca II H&K saturation level at about $R'_{\text{HK}} = -4.4$. However, neither found evidence of a dropoff in activity as Ro decreases. In the unsaturated regime, the previous works find a log-linear correlation that is also traced out by our sample. The [Astudillo-Defru et al. \(2017a\)](#) and [Boudreaux et al. \(2022\)](#) relations are offset from one another, suggesting a mass-dependent level of normalized Ca II H&K emission in the unsaturated regime. Qualitatively, such a mass-dependence manifests similarly in our sample.

Following [Astudillo-Defru et al. \(2017a, Fig. 6 therein\)](#), we plot our R'_{HK} against P_{rot} for stars with ‘secure’ periods in

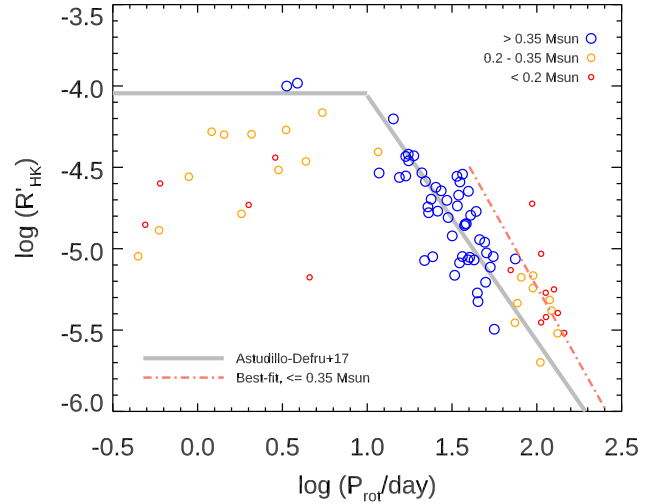


Fig. 10. Normalized Ca II H&K emission (R'_{HK}) as a function of P_{rot} . ‘D’ and ‘P’ rotators are omitted from the plot. The relation from [Astudillo-Defru et al. \(2017a\)](#) is overplotted in grey. To illustrate the offset with that relation for our fully convective stars in the unsaturated regime, we also show the best-fit power law for 18 ‘S’ rotators with $M_* \leq 0.35 M_{\odot}$ and $P_{\text{rot}} > 40$ d in dashed red lines.

Fig. 10. The correlation quantified by [Astudillo-Defru et al. \(2017a\)](#) is overplotted. While this empirical relation has limited physical meaning in itself, it has been widely applied in crudely estimating rotation periods of inactive stars in the unsaturated regime, whose R'_{HK} can be readily obtained.

The agreement with our measurements is decent overall, with a root-mean-square scatter of ~ 0.17 dex in P_{rot} . While the early-M dwarfs appears to follow the relation of [Astudillo-Defru et al. \(2017a\)](#), our smallest stars ($< 0.2 M_{\odot}$) appear to have systematically higher R'_{HK} for a given P_{rot} . For illustration, we fitted a power law to the 18 fully convective stars with ‘secure’ $P_{\text{rot}} > 40$ d to obtain the following:

$$\log R'_{\text{HK}} = -1.86 \log(P_{\text{rot}}/d) - 1.52. \quad (7)$$

Evaluated for $\log(R'_{\text{HK}}) = -5.0$, [Astudillo-Defru et al. \(2017a\)](#) gives $P_{\text{rot}} = 42$ d whereas Eq. (7) would give $P_{\text{rot}} = 74$ d. Considering that the sample of [Astudillo-Defru et al. \(2017a\)](#) contained only 7 fully convective M dwarfs with $P_{\text{rot}} > 40$ d, it may be tempting to conclude that their relation is simply less accurate for mid- and late-M dwarfs. On the other hand, such a large discrepancy could also be explained by methodological differences in the way R'_{HK} is derived between the works. [Perdelwitz et al. \(2021\)](#) pointed out that their R'_{HK} measurements are systematically offset by ~ 0.2 dex from that of [Astudillo-Defru et al. \(2017a\)](#) towards lower activity values and later-type stars, especially for $\log(R'_{\text{HK}}) < -5.0$. Such an offset roughly corresponds to the size of the observed discrepancy. Therefore, when using an R'_{HK} – P_{rot} relation to infer P_{rot} , it is important to use the version correctly calibrated to the method-specific R'_{HK} measurements.

B-field. [Reiners et al. \(2022\)](#) measured average surface magnetic field strengths (or upper limits) for 283 M dwarfs in our sample by modelling high-resolution CARMENES spectra. They showed that the rotation– B field relation takes an analogous form to that of other well-known rotation–activity relations. This has significant implications for the magnetic origin of stellar activity phenomena, as discussed extensively by [Reiners et al. \(2022\)](#).

¹⁵ This fit was done without the severe outlier J14257+236W, whose long period is provisional and whose inclusion would have drastically skewed the fit.

We show $\langle B \rangle$ versus Ro for the 162 stars in our sample with both $\langle B \rangle$ (excluding upper limits) and P_{rot} measurements in Fig. 9. Of these, 149 have ‘S’ (secure) and ‘P’ (provisional) period designations. As before, we fitted the canonical rotation-activity relation Eq. (6) to $\langle B \rangle$. Due to the dearth of early-M dwarfs with B -field measurements on the saturated arm, these fits were not carried out on the early-M subset. The best-fit parameters are printed in Table 2.

The whole-sample fits agree well with the original relation given in Reiners et al. (2022; despite slight difference in the computation of τ_{conv} , see Appendix B). The saturated regime exhibit a downward slope of ~ -0.09 significant to $>2\sigma$, comparable to the -0.11 ± 0.03 slope found by Reiners et al. (2022), indicating that surface magnetic field strengthens with decreasing Rossby number even in the nominal saturation regime (see also Kochukhov 2021). The trend appears to extend down to $Ro = 10^{-3}$.

The free-fitted saturation breakpoint settled on $Ro_{\text{sat}} \sim 0.1$ and ~ 0.16 for the whole sample and the fully convective subset, respectively, which are fairly similar to the 0.13 assumed by Reiners et al. (2022). However, the slope of -1.0 in the unsaturated arm is somewhat in tension with that of Reiners et al. (2022, $\beta_{\text{unsat}} = -1.26 \pm 0.10$). This discrepancy could be partially attributed to updates to the sample, as well as in differences in the fitting methods (i.e., in Reiners et al. 2022, the ordinary least squares bisector method was used, which accounts for error in both X and Y variables).

5.2. Period–mass, period–kinematics relations

Several previous works have investigated the distribution of rotation periods as a function of stellar mass and age, in order to shed light on the mechanisms of rotational evolution (e.g., Irwin et al. 2009; McQuillan et al. 2014; Newton et al. 2016b; Rebull et al. 2018; Popinchalk et al. 2021). A striking finding relates to the shape of the upper and lower envelopes in P_{rot} . The maximum P_{rot} has been shown to increase from ~ 50 d in early-M dwarfs to ~ 150 d in the latest-type M dwarfs, while the minimum P_{rot} decreases from ~ 0.3 to ~ 0.1 d over the same mass range. Another key insight from these studies is the bimodality of the distribution among the mid- to late-type M dwarfs, clustering around $P_{\text{rot}} < 5$ d and > 50 d. Relatively few stars have a rotation period intermediate between the two extremes, with the gap opening wider towards lower masses. On the other hand, earlier-type stars are much less likely to be found as fast-rotators. Since stars across the mass range are born with statistically indistinguishable primordial rotation period distributions (Venuti et al. 2017; Popinchalk et al. 2021), any differences in their final rotation distributions must mean they have experienced different angular momentum shedding pathways over time.

How the CARMENES survey sample fits into the context of the period-mass relationship for M dwarfs is displayed in Fig. 11. We plot the P_{rot} values against the stellar masses for our sample. The background shows measurements by McQuillan et al. (2014) and Newton et al. (2016b, ‘A’ and ‘B’ rotators only) from *Kepler* and M_{Earth} light curves, respectively. Unlike previous studies, which often used optical colours as proxies for mass, the stellar masses for the CARMENES sample are homogeneously determined as detailed in Sect. 4.3.

The CARMENES sample traces out the major features that have been noted by previous authors. Though our sample is not as large as some of its predecessors, it generously covers both sides of the partial-to-fully convective boundary, thereby better resolving the upper envelope in the transition region between the early and mid-M dwarfs at $\sim 0.4 M_{\odot}$ (see

also Fig. 12 in Popinchalk et al. 2021). The large quantity of measurements from *Kepler* light curves shows a sharp boundary at 40–50 d, which seemingly represents the maximum rotation period attained for early M dwarfs (McQuillan et al. 2014). Our sample appears to challenge this notion, exhibiting a fuzzy upper envelope sprinkled with several stars with $P_{\text{rot}} \sim 100$ d. However, none of these long periods have the status ‘secure’. To understand the end state of early-M dwarf spin evolution, it would be useful to clarify these periods with additional measurements.

An underlying variable in the period-mass distribution is stellar age, which governs the stage of a star’s spin-down. While precise ages for M dwarfs are difficult to determine directly, Galactic kinematic information can provide constraints. Since CARMENES is an RV survey, all stars have their v_{rad} measured from high-resolution spectra. Combining these with *Gaia* proper motions gives a full picture of the 3D Galactic kinematics of these stars. Cardona et al. (2022) matched Galactic kinematics of the CARMENES sample to known young moving groups in the solar neighbourhood and deduced ages for a young subsample up to ~ 800 Myr. The age-resolved period-mass diagram is also shown in Fig. 11. Despite its coarseness, the age dimension gives structure to the period-mass scatter plot. The earliest M dwarfs ($\geq 0.5 M_{\odot}$) already begin to settle onto the slow-rotating sequence at ~ 100 Myr. By 800 Myr the sequence includes most stars with $\geq 0.4 M_{\odot}$. SBs identified by Baroch et al. (2018, 2021) are marked and can account for most of the few early-M field stars that fall significantly below the slow-rotator sequence. The fact that the slow rotator sequence is not yet in place by 800 Myr across the entire M dwarf mass range has also been established by other authors using K2 data in open clusters (e.g., Douglas et al. 2017; Popinchalk et al. 2021).

The sample exhibits a bimodality of periods below $\sim 0.4 M_{\odot}$, with a gap of intermediate periods separating the slow- and fast-rotating sequence. This is a consequence of the much longer overall timescales of spin-down in fully convective stars. Assuming that the star formation history in the solar neighbourhood has not been punctuated, Newton et al. (2016b) proposed that the gap feature among fully convective stars can be explained by first stalled, then rapid spin-down past a given P_{rot} . A similar phenomenon has been reported in sunlike stars and early M dwarfs (e.g., Curtis et al. 2020). Here we show that a large fraction of the fast-rotators can be associated with a young age. Within this range of ages below ~ 1 Gyr, the collection of rapid rotators among the late-M dwarfs lacks clear stratification. This region in the $P_{\text{rot}}-M_{\star}$ space likely comprises a mixture of the natal distribution of rotation rates, spin-up due to size contraction during the long pre-main sequence lifetimes (a few hundred Myr), and subsequent spin-down (see also Popinchalk et al. 2021).

Since there are few rotators in the intermediate-period transition region (~ 30 d) and none have an inferred age, it is difficult to directly study the hypothesis of Newton et al. (2016b). Interestingly, the position and shape of the gap appear to be correlated with the phenomenon of activity-saturation, which could provide a clue to its origin. As in Jeffers et al. (2018), we plot in Fig. 11 the X-ray saturation period as a function of stellar mass based on Eq. (10) from Reiners et al. (2014). To apply this equation, we mapped M_{\star} into L_{bol} using a 5-Gyr PARSEC isochrone at solar metallicity (Bressan et al. 2012). The saturation period curve divides the clusters of slow and fast rotators and traces the shape of the lower envelope of the slow period sequence. There is a marked deficit of stars in the neighbourhood of this curve, which coincides with the gap. This seems to

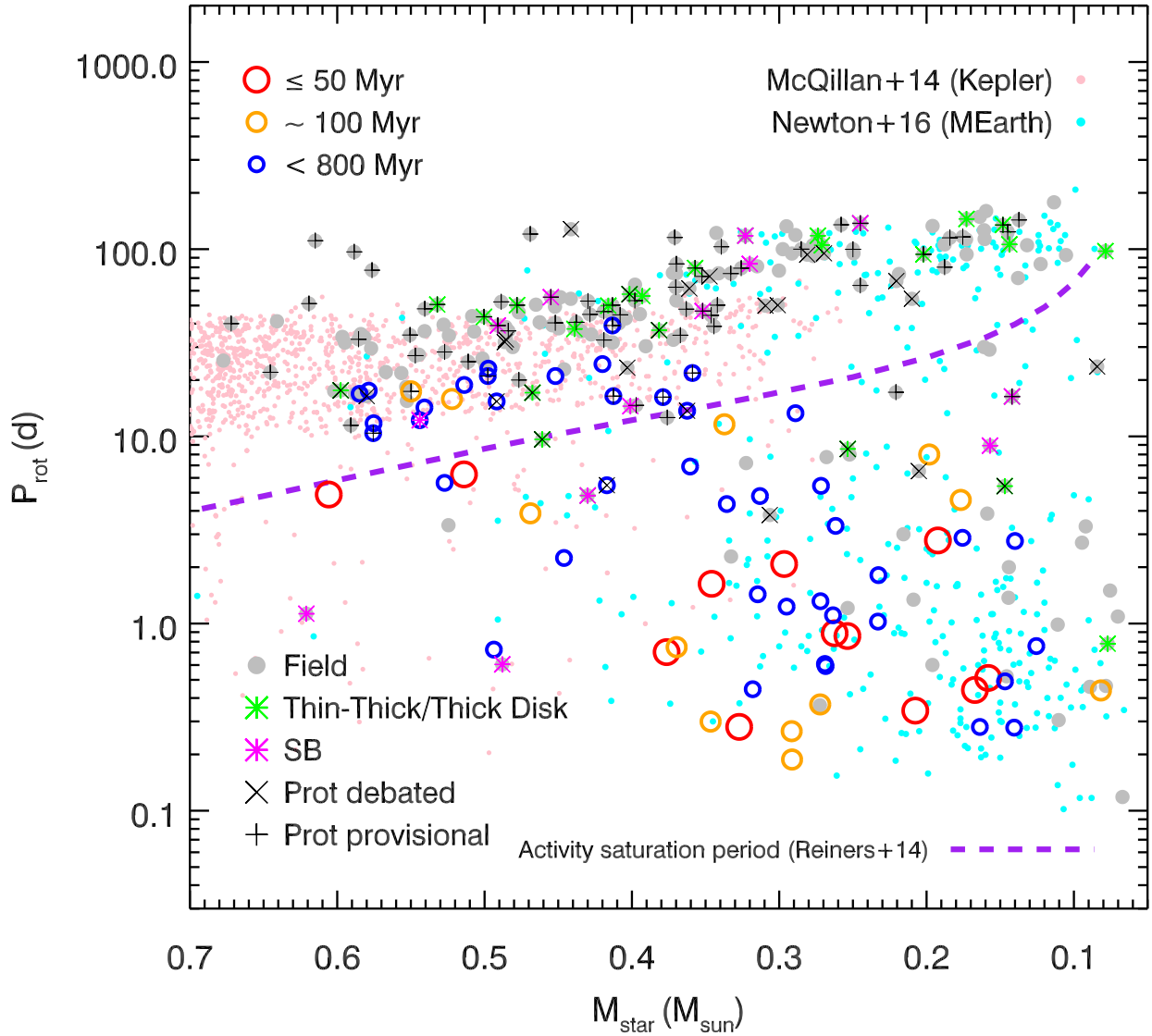


Fig. 11. Measured P_{rot} versus M_{star} . Pink and cyan points represent stars from [McQuillan et al. \(2014\)](#) and [Newton et al. \(2016b; ‘A’ and ‘B’ rotators only\)](#), respectively. The purple dashed line represents the saturation period as a function of stellar mass, based on Eq. (10) of [Reiners et al. \(2014\)](#) and L_{bol} from 5-Gyr PARSEC isochrones ([Bressan et al. 2012](#)). The empty circles denote young stars in the CARMENES sample assigned to stellar kinematic groups by [Cardona et al. \(2022\)](#). They are colour- and size-coded by age, as indicated in the legend. Filled grey points represent the rest of the stars from the CARMENES sample (collectively termed ‘field’). Additional symbols overlaid on the CARMENES stars: magenta asterisks mark known SBs or spectroscopic triples; green asterisks highlight stars belonging to the thin-thick or thick disk based on Galactic kinematics; black ‘X’s and ‘+’s denote stars with debated or provisional periods, respectively.

illustrate a physical link between angular momentum evolution and activity saturation: a star experiences efficient spin-down until it has exited the saturation phase (e.g., [Reiners & Mohanty 2012](#)). Many mid- to late-type M dwarfs appear to remain in the saturation regime into field age (i.e., ≥ 1 Gyr), which is also likely related to their observed activity lifetimes of several Gyr ([West et al. 2008](#)).

To observationally resolve the spin evolution sequence between ~ 1 Gyr and the field requires ideally a comprehensive study of rotation periods for M dwarfs in benchmark open clusters of intermediate age. However, few such clusters are nearby, and none close enough to probe down to M dwarf brightness (e.g., [Curtis et al. 2020](#)), at least not without resource-intensive campaigns on large ground-based telescopes (e.g., M67, [Dungee et al. 2022](#)). Another crude age indicator is membership in the Galaxy’s structural components. In Fig. 11 we indicate the stars kinematically classified to be in the thin-thick

or thick disk component of the Galaxy ([Cortés Contreras 2017](#)), which correspond to stars ≥ 8 Gyr (e.g., [Fuhrmann 1998](#)). Most of them seem to fall on the upper envelope of the slow rotator sequence, consistent with the spin-down framework.

Relatedly, Galactic velocity dispersion can also serve as a direct (if crude) age proxy, whereby larger velocity dispersion is associated with older age (e.g., [Newton et al. 2016b; Kuman et al. 2019; Angus et al. 2020; Lu et al. 2021](#)). Figure 12 compares the Galactic kinematics (as measured by *Gaia* and CARMENES RV) with the measured P_{rot} for the CARMENES GTO sample, as well as for the ‘A’ and ‘B’ rotators in [Newton et al. \(2016b\)](#). As in [Newton et al. \(2016b\)](#), we use $\sqrt{U^2 + V^2 + W^2}$ from *Gaia* EDR3 to quantify the total space motion of each star, where U , V and W are the radial, azimuthal, and vertical velocity components with respect to the local standard of rest ($U_{\odot}, V_{\odot}, W_{\odot} = [11, 12, 7] \text{ km s}^{-1}$). Stars with larger rotation periods tend to have a larger spread in space velocities

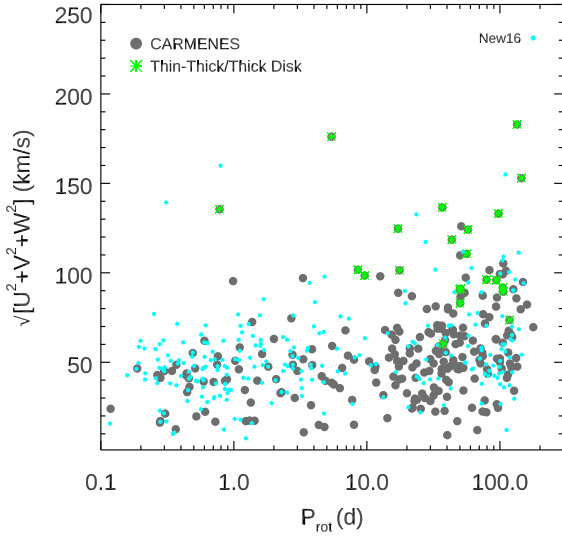


Fig. 12. Measured P_{rot} versus galactic kinematics. Grey filled points represent the CARMENES sample presented in this work. Cyan points denote stars from [Newton et al. \(2016b\)](#); ‘A’ and ‘B’ rotators only). The green asterisks are classified to be thin-thick or thick disk stars.

and larger average space motions, which is expected given slower rotators tend to be older stars. This is an average trend and does not apply in the one-on-one sense to individual stars, since the process of dynamically heating the Galactic disk is stochastic.

Recently, [Pass et al. \(2022\)](#) showed that yet another promising avenue to investigate the rotation history of M dwarfs is to study those with wide binary companions (FGK or white dwarfs) whose ages can be constrained. They narrowed the window for rapid spin-down to around 2–3 Gyr. Using gyro-kinematic ages on a large sample of stars, [Lu et al. \(2024\)](#) identified evidence of fundamental changes to the spindown mechanism across the fully-convective boundary, with fully convective stars experiencing significantly higher angular momentum loss rates. The advent of new gyrochronological relations calibrated for M dwarfs ([Dunee et al. 2022](#); [Gaidos et al. 2023](#); [Engle & Guinan 2023](#); [Lu et al. 2023](#)) will shed further light on the spin evolution of low-mass stars and cement P_{rot} as a critical input in constraining ages.

5.3. Planet hosts

There are 97 known planets across 63 systems in our 348-star sample (see Table C.4). Figure 13 shows the planet orbital versus stellar rotation periods, and Fig. 14 plots the raw rotation period distribution of known planet hosts compared to the overall sample. Relative to the ambient stellar background, planet hosts appear to have a significant preference for slower rotation. According to a two-sample Komolgorov–Smirnov (K–S) test, the distributions are distinct at high significance ($p\text{-value} = 2.4 \times 10^{-10}$).

The discrepancy could be rooted in astrophysics or due to observational bias. RV surveys have more complex selection effects, in part because their sampling strategies are often concerned with maximizing planet yields. A clue that favours observational bias as the explanation for the relative dearth of fast-rotating planet hosts in our sample is that, while the majority of planets in this sample were found by RV, three out of the four planet systems around the stars with $P_{\text{rot}} < 15$ d were discovered

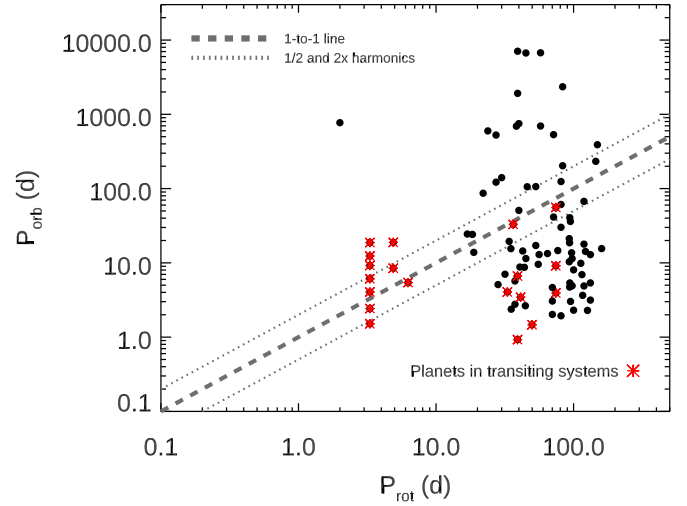


Fig. 13. Orbital period of planets versus spin period of host stars. Planets in transiting systems are denoted by red asterisks. The 1-to-1 relation is in grey dashed lines, while the 1/2 \times and 2 \times harmonics are in grey dotted lines.

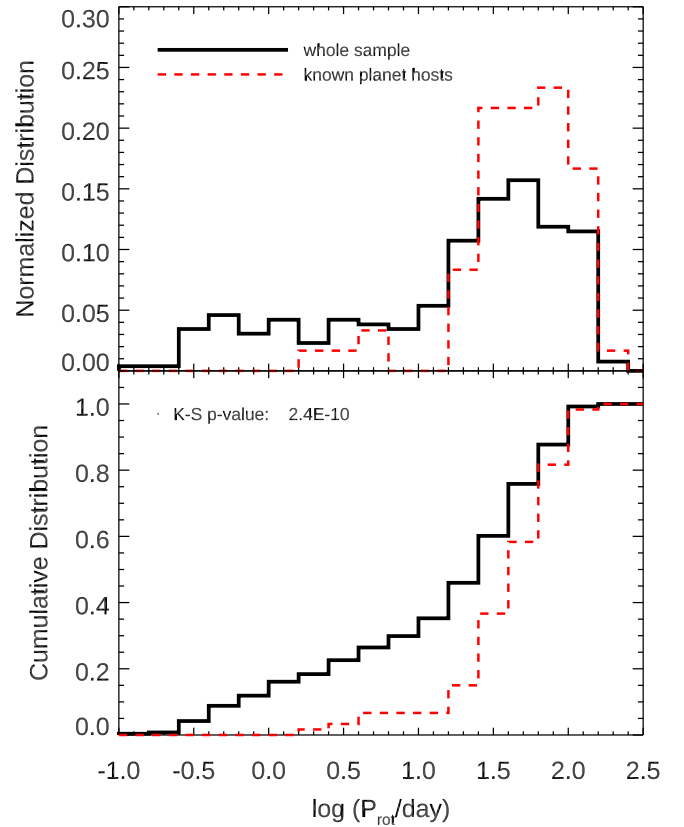


Fig. 14. Rotation period distribution of all known planet hosts (red dashed) compared to the entire sample (black solid). Top: differential distribution. Bottom: cumulative distribution. The p -value of the 2-sample K–S test is 2.4×10^{-10} , i.e., the two distributions are very likely to be distinct.

by transit (K2-33, AU Mic, TRAPPIST-1), the exception being TZ Ari. Since the RV method is less sensitive to planets around active stars, the monitoring of certain targets, many of which are fast rotators, were discontinued early on ([Sabotta et al. 2021](#); [Ribas et al. 2023](#)).

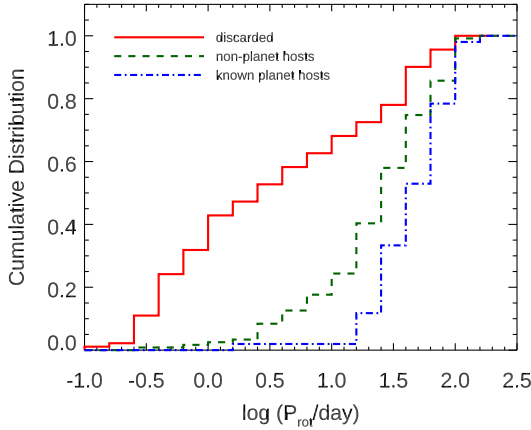


Fig. 15. Cumulative distribution of rotation periods in the context of RV selection biases. Red solid: rotation period distribution of stars discarded in the planet occurrence analysis of Ribas et al. (2023); green dashed: stars in common with Ribas et al. (2023) that are not known to be planet hosts; blue dot-dashed: known planet hosts in Ribas et al. (2023).

To control for the effect of RV survey selection bias against active stars, we cross-matched our sample of stars with P_{rot} measurements with that used in the planet occurrence rate analysis of Ribas et al. (2023), which is also based on the M dwarfs observed in the CARMENES GTO survey. The sample was debiased by discarding RV-loud stars (Tal-Or et al. 2018), spectroscopic binaries and triples (mostly from Baroch et al. 2018 and Baroch et al. 2021), as well as excluding systems with transiting planets not in the original input catalogue (especially TESS planets), or with fewer than ten RV measurements. Of the 170 stars in common between the two samples, 51 have known planets. In addition, there are 68 stars in the sample of Ribas et al. (2023) without a P_{rot} determination, four of which have planets. On the other hand, there are another 91 stars, nine of which have known planets, with a P_{rot} determination but discarded from the planet occurrence rate analysis of Ribas et al. (2023).

We compare the P_{rot} distribution for the discarded and debiased sample in Fig. 15. About 75% of the discarded stars have $P_{\text{rot}} < 15$ d, with a broad maximum at about 0.5–2 d. More than 40% of these stars are RV-loud stars, among them young transiting planet systems such as K2-33 (David et al. 2016) and AU Mic (Plavchan et al. 2020). In the debiased sample of Ribas et al. (2023), the distributions of planet hosts and non-hosts are identical for $P_{\text{rot}} \gtrsim 15$ d. Previous works mostly focused on sunlike stars have found that there is no relation between the P_{rot} of moderate and low rotators and the presence of planets (e.g., Walkowicz & Basri 2013; Ceillier et al. 2016). However, to our knowledge, our work represents one of the first times that this is established for M dwarfs.

At $P_{\text{rot}} \lesssim 15$ d, a significant deficit of stars with known planets compared to those without persists even in the debiased sample. This could still be attributed to detection bias. That is, everything else being equal, it is more difficult to detect a low-RV amplitude planet of a given mass and orbital period around an M dwarf with a shorter P_{rot} , owing to stronger magnetic field and greater RV jitter (Reiners et al. 2018b, 2022). Such a bias would not be completely eliminated by the target exclusion criteria of Ribas et al. (2023). This explanation is most plausible because fast-rotation is an evolutionary phase in the star’s lifetime, and the slow-rotating stars, virtually all of which have on average at least one planet (Ribas et al. 2023), started out as fast-rotators. It is also possible that planets in M dwarf systems tend to start out

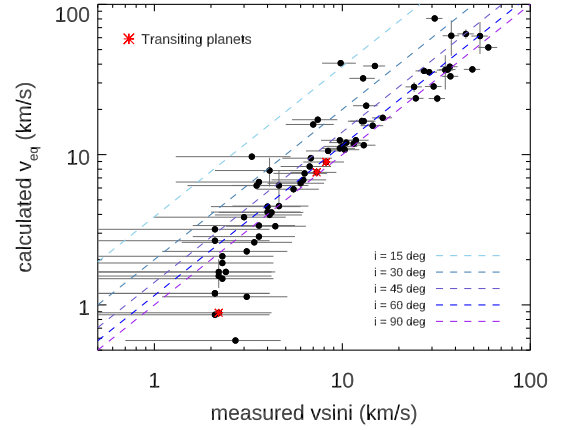


Fig. 16. Projected spin inclination angles for stars with measured $v \sin i$. Transiting planet systems are highlighted in red asterisks and consistent with a spin-orbit-aligned configuration. The rest are not known to be planet hosts.

on larger orbits and migrate secularly inwards over time, making younger planets more difficult to detect in RV surveys than their mature counterparts.

The fact that astrophysics may play a role in sculpting the dearth of planets discovered around fast-rotators has been proposed before. Using three years of data from *Kepler*, a transiting planet survey largely immune to RV biases, McQuillan et al. (2013b) discovered a notable lack of close-in planets ($P_{\text{orb}} \lesssim 3$ d) around fast-rotating stars ($P_{\text{rot}} \lesssim 10$ d). They discussed aspects of physical coupling in the angular momentum evolution of the star-planet system, including processes such as stellar magnetic braking, planet migration, and tidal interactions, which could affect the demographics of planets as a function of stellar rotation state. However, the exact mechanism leading to their specific observed pattern was unclear. Recently, Sibony et al. (2022) found evidence that planet-hosting stars rotate 1.6 d slower than non planet-hosts, a small but significant difference. However, they could not identify the root cause responsible for this difference. Both works dealt chiefly with sunlike stars.

To disentangle the two scenarios would require a detailed completeness analysis on the data as well as star and planet formation and evolution models beyond the scope of this manuscript. Nevertheless, our work demonstrates that, even with a state-of-the-art observing programme such as CARMENES, there are still significant challenges in studying planets around young and active M dwarfs using the RV technique, restricting our ability to probe nascent planet populations in early stages of evolution.

For stars with known $v \sin i$, R_* , and P_{rot} , the line-of-sight inclination of the stellar rotation axis can be constrained (see Eq. (3)). Figure 16 presents these stars overplotted on iso-inclination contours. Those stars falling beyond the 90 deg contour are outliers discussed in Sect. 4.3 and Appendix A.2. The only known planet hosts among these stars are transiting planet systems, and they are consistent with spin-orbit alignment.

6. Summary

In this work, we further characterize the CARMENES survey input sample of 348 nearby bright M dwarfs by presenting new rotation period determinations from photometric and spectroscopic time series data. Our data come from ground-based photometric observations (e.g., the SuperWASP survey), from the

TESS satellite, and from the CARMENES spectroscopic survey itself. Standard periodogram analyses followed by careful vetting yielded 158 periods for 129 stars (some stars have measurements in multiple data sets), ranging between 0.12 d and 140 d. While the majority of short periods (<5 d) were measured by single-sector TESS-PDCSAP data and longer periods (>10 d) by ground-based surveys spanning year-long baselines, we found multi-sector TESS SAP light curves to be effective for detecting or verifying a number of intermediate periods (~ 5 – 20 d). Together with measurements already available in the literature, the total number of stars in this sample with a measured rotation period is now 261 or 75%.

Leveraging the comprehensive and uniform catalogue of stellar properties for this sample that has been recently made available, we study P_{rot} as a function of various stellar parameters. We find the periods to have very good consistency with $v \sin i$ and R_{\star} measurements in the subsample for which all three properties have been determined. P_{rot} exhibits the expected overall negative correlation with the $pEW'_{\text{H}\alpha}$ metric, a proxy for H α emission, though with considerable scatter. Combining information from $v \sin i$, $pEW'_{\text{H}\alpha}$, and agreement with literature measurements, we recommend one P_{rot} value for each star and assign a confidence rating of ‘secure’, ‘provisional’, or ‘debated’.

Since many of the stars in our sample have multiple period measurements available in the literature, we assess their typical degree of consistency as a function of period itself. Fitting a power law, we find the dispersion of independent period measurements for a star to be strongly positively correlated with period value. We adopt this power law function as an empirical estimate of P_{rot} error. Short periods (<10 d) are most likely to be very precise ($\sim 1\%$), whereas longer periods (>100 d) can be determined to no better than $\sim 10\%$. Furthermore, 25% of periods longwards of 10 d have a dispersion $>20\%$. In general, published formal errors fall short of the empirical errors, by $1.5\times$ for $P_{\text{rot}} \geq 10$ d and $2\times$ for $P_{\text{rot}} \geq 100$ d. The trend of growing error with period value chiefly reflects the fact that longer P_{rot} ’s are in practice more difficult to measure owing to a variety of factors, and that the difficulty scales more than proportionally with the length of the period. We recommend using independent measurements to verify P_{rot} ’s longwards of ~ 10 d. Since the habitable zones around all but the latest M dwarfs lie beyond the orbital period of ~ 10 d (Newton et al. 2016a; Kopparapu et al. 2013), careful determination of stellar rotation periods in this range is critical to rule out false positives and confirm the most interesting RV planet detections.

We show the sample in the context of rotation-activity relations for chromospheric (H α , Ca II H&K) and coronal (X-ray) emission, as well as surface B-field strength as a function of the Rossby number. Our fits are broadly consistent with those obtained by previous authors. We find small but suggestive evidence for mass-dependence in the saturation behaviour of X-ray and H α emission across the fully-convective boundary, as well as a possible non-constant level of H α emission in the saturation regime. A larger sample building on the current one is needed to test the robustness of these results. We show that choice of methodologies in measuring Ca II H&K emission can have a significant quantitative impact on the $R'_{\text{HK}}-P_{\text{rot}}$ relation.

We also examine P_{rot} versus stellar mass, galactic kinematics, and age, confirming the previous findings of an upper envelope in P_{rot} that increases with stellar mass across the M dwarf range, and a relative dearth of rotators with intermediate periods (~ 5 – 50 d) among fully convective stars. Early-M dwarfs reach the bottom of the slow-rotator sequence by 800 Myr and continue to spin down. Fully convective M dwarfs remain as fast

rotators in the activity-saturated regime until beyond 1 Gyr, but eventually reach >100 d periods. The deficit of intermediate-period rotators among mid- to late-M dwarfs appears to coincide with their activity-saturation periods, suggesting a physical link. The slowest rotators are associated with the largest space motion, consistent with belonging to older kinematic components of the Galaxy. Several early-M dwarfs appear to have rotation periods in the ~ 100 d range, much slower than the upper limit suggested by *Kepler* data (McQuillan et al. 2014), which warrants further investigation with independent measurements.

Finally, we point out that the known planet hosts in this sample are overwhelmingly preferentially slow rotators ($P_{\text{rot}} \geq 15$ d). Since the majority of planets in this sample were found by RV, such an outcome predominantly reflects selection and detection biases in blind RV surveys. Considering most M dwarfs with ages ≤ 1 Gyr have $P_{\text{rot}} \lesssim 15$ d, there are evidently important challenges in using the RV technique to discover and study young planet systems.

Acknowledgements. We thank the anonymous reviewer for insightful and constructive suggestions that significantly improved the quality of this work. CARMENES is an instrument for the Centro Astronómico Hispano-Alemán de Calar Alto (CAHA, Almería, Spain). CARMENES is funded by the German Max-Planck-Gesellschaft (MPG), the Spanish Consejo Superior de Investigaciones Científicas (CSIC), the European Union through FEDER/ERF FICTS-2011-02 funds, and the members of the CARMENES Consortium (Max-Planck-Institut für Astronomie, Instituto de Astrofísica de Andalucía, Landessternwarte Königstuhl, Institut de Ciències de l’Espai, Institut für Astrophysik Göttingen, Universidad Complutense de Madrid, Thüringer Landessternwarte Tautenburg, Instituto de Astrofísica de Canarias, Hamburger Sternwarte, Centro de Astrobiología and Centro Astronómico Hispano-Alemán), with additional contributions by the Spanish Ministry of Economy, the German Science Foundation through the Major Research Instrumentation Programme and DFG Research Unit FOR2544 “Blue Planets around Red Stars”, the Klaus Tschira Stiftung, the states of Baden-Württemberg and Niedersachsen, and by the Junta de Andalucía. The *Joan Oró* Telescope (TJO) of the Montsec Observatory (OdM) is owned by the Generalitat de Catalunya and operated by the Institute for Space Studies of Catalonia (IEEC). This work makes use of observations from the Las Cumbres Observatory global telescope network. We acknowledge financial support from the Agencia Estatal de Investigación of the Ministerio de Ciencia e Innovación through projects PID2019-109522GB-C51[14], PID2019-107061GB-C64, and PID2019-110689RB-100 and the Centre of Excellence ‘Severo Ochoa’ Instituto de Astrofísica de Andalucía (SEV-2017-0709). Data were partly collected with the 90-cm and 150-cm telescopes at Sierra Nevada Observatory (OSN), operated by the Instituto de Astrofísica de Andalucía (IAA, CSIC). This work was also funded by the Generalitat de Catalunya/CERCA programme, and the DFG through the priority programme SPP 1992 “Exploring the Diversity of Extrasolar Planets” (JE 701/5-1) and the Research Unit FOR2544 “Blue Planets around Red Stars”.

References

- Affer, L., Damasso, M., Micela, G., et al. 2019, *A&A*, **622**, A193
- Agol, E., Dorn, C., Grimm, S. L., et al. 2021, *PSJ*, **2**, 1
- Aigrain, S., Llama, J., Ceillier, T., et al. 2015, *MNRAS*, **450**, 3211
- Aller, A., Lillo-Box, J., Jones, D., Miranda, L. F., & Barceló Forteza, S. 2020, *A&A*, **635**, A128
- Alonso-Floriano, F. J., Morales, J. C., Caballero, J. A., et al. 2015, *A&A*, **577**, A128
- Amado, P. J., Bauer, F. F., Rodríguez López, C., et al. 2021, *A&A*, **650**, A188
- Angus, R., Morton, T., Aigrain, S., Foreman-Mackey, D., & Rajpaul, V. 2018, *MNRAS*, **474**, 2094
- Angus, R., Beane, A., Price-Whelan, A. M., et al. 2020, *AJ*, **160**, 90
- Astudillo-Defru, N., Delfosse, X., Bonfils, X., et al. 2017a, *A&A*, **600**, A13
- Astudillo-Defru, N., Díaz, R. F., Bonfils, X., et al. 2017b, *A&A*, **605**, L11
- Astudillo-Defru, N., Forveille, T., Bonfils, X., et al. 2017c, *A&A*, **602**, A88
- Barnes, S. A. 2007, *ApJ*, **669**, 1167
- Baroch, D., Morales, J. C., Ribas, I., et al. 2018, *A&A*, **619**, A32
- Baroch, D., Morales, J. C., Ribas, I., et al. 2021, *A&A*, **653**, A49
- Basri, G., & Shah, R. 2020, *ApJ*, **901**, 14
- Basri, G., Streichenberger, T., McWard, C., et al. 2022, *ApJ*, **924**, 31
- Bauer, F. F., Zechmeister, M., Kaminski, A., et al. 2020, *A&A*, **640**, A50
- Blanco-Pozo, J., Perger, M., Damasso, M., et al. 2023, *A&A*, **671**, A50

- Bluhm, P., Luque, R., Espinoza, N., et al. 2020, *A&A*, **639**, A132
- Bonfils, X., Astudillo-Defru, N., Díaz, R., et al. 2018, *A&A*, **613**, A25
- Boudreaux, T. M., Newton, E. R., Mondrik, N., Charbonneau, D., & Irwin, J. 2022, *ApJ*, **929**, 80
- Bourrier, V., Lovis, C., Beust, H., et al. 2018, *Nature*, **553**, 477
- Brasseur, C. E., Phillip, C., Fleming, S. W., Mullally, S. E., & White, R. L. 2019, *Astrophysics Source Code Library* [record ascl:1905.0007]
- Bressan, A., Marigo, P., Girardi, L., et al. 2012, *MNRAS*, **427**, 127
- Brown, T. M., Baliber, N., Bianco, F. B., et al. 2013, *PASP*, **125**, 1031
- Burn, R., Schlecker, M., Mordasini, C., et al. 2021, *A&A*, **656**, A72
- Butters, O. W., West, R. G., Anderson, D. R., et al. 2010, *A&A*, **520**, L10
- Caballero, J. A., Cortés-Contreras, M., Alonso-Floriano, F. J., et al. 2016, in *19th Cambridge Workshop on Cool Stars, Stellar Systems, and the Sun (CS19)*, 148
- Caballero, J. A., González-Álvarez, E., Brady, M., et al. 2022, *A&A*, **665**, A120
- Cale, B. L., Reefe, M., Plavchan, P., et al. 2021, *AJ*, **162**, 295
- Cardona, C., Bejar, V. J. S., Lodieu, N., et al. 2022, *A&A*, submitted
- Ceillier, T., van Saders, J., García, R. A., et al. 2016, *MNRAS*, **456**, 119
- Charbonneau, P. 2005, *Liv. Rev. Sol. Phys.*, **2**, 2
- Christian, D. J., Mathioudakis, M., Arias, T., Jardine, M., & Jess, D. B. 2011, *ApJ*, **738**, 164
- Cifuentes, C., Caballero, J. A., Cortés-Contreras, M., et al. 2020, *A&A*, **642**, A115
- Cloutier, R., Astudillo-Defru, N., Doyon, R., et al. 2017, *A&A*, **608**, A35
- Cloutier, R., Rodríguez, J. E., Irwin, J., et al. 2020, *AJ*, **160**, 22
- Collins, K. A., Kielkopf, J. F., Stassun, K. G., & Hessman, F. V. 2017, *AJ*, **153**, 77
- Colome, J., & Ribas, I. 2006, *IAU Special Session*, **6**, 11
- Cortés Contreras, M. 2017, PhD Thesis, Complutense University of Madrid, Spain
- Cortés-Contreras, M., Béjar, V. J. S., Caballero, J. A., et al. 2017, *A&A*, **597**, A47
- Cram, L. E., & Mullan, D. J. 1979, *ApJ*, **234**, 579
- Curtis, J. L., Agüeros, M. A., Matt, S. P., et al. 2020, *ApJ*, **904**, 140
- Czesla, S., Schröter, S., Schneider, C. P., et al. 2019, *Astrophysics Source Code Library* [record ascl:1906.010]
- Damasso, M., Perger, M., Almenara, J. M., et al. 2022, *A&A*, **666**, A187
- David, T. J., Hillenbrand, L. A., Petigura, E. A., et al. 2016, *Nature*, **534**, 658
- Dedrick, C. M., Fulton, B. J., Knutson, H. A., et al. 2021, *AJ*, **161**, 86
- Delrez, L., Gillon, M., Queloz, D., et al. 2018, in *Ground-based and Airborne Telescopes VII*, eds. H. K. Marshall, & J. Spyromilio, *SPIE Conf. Ser.*, **10700**, 1070011
- Díaz, R. F., Delfosse, X., Hobson, M. J., et al. 2019, *A&A*, **625**, A17
- Díez Alonso, E., Caballero, J. A., Montes, D., et al. 2019, *A&A*, **621**, A126
- Donahue, R. A., Saar, S. H., & Balunas, S. L. 1996, *ApJ*, **466**, 384
- Donati, J. F., Morin, J., Petit, P., et al. 2008, *MNRAS*, **390**, 545
- Donati, J. F., Lehmann, L. T., Cristofari, P. I., et al. 2023, *MNRAS*, **525**, 2015
- Douglas, S. T., Agüeros, M. A., Covey, K. R., & Kraus, A. 2017, *ApJ*, **842**, 83
- Dreizler, S., Crossfield, I. J. M., Kossakowski, D., et al. 2020, *A&A*, **644**, A127
- Dressing, C. D., & Charbonneau, D. 2015, *ApJ*, **807**, 45
- Dunee, R., van Saders, J., Gaidos, E., et al. 2022, *ApJ*, **938**, 118
- Durney, B. R., & Latour, J. 1978, *Geophys. Astrophys. Fluid Dyn.*, **9**, 241
- Engle, S. G., & Guinan, E. F. 2023, *ApJ*, **954**, L50
- Fekel, F. C., & Henry, G. W. 2000, *AJ*, **120**, 3265
- Feng, J., Shectman, S. A., Clement, M. S., et al. 2020, *ApJS*, **250**, 29
- Foreman-Mackey, D., Hogg, D. W., Lang, D., & Goodman, J. 2013, *PASP*, **125**, 306
- Fouqué, P., Martioli, E., Donati, J. F., et al. 2023, *A&A*, **672**, A52
- Fuhrmann, K. 1998, *A&A*, **338**, 161
- Fuhrmeister, B., Czesla, S., Schmitt, J. H. M. M., et al. 2019, *A&A*, **623**, A24
- Fuhrmeister, B., Czesla, S., Perdelwitz, V., et al. 2023, *A&A*, **670**, A71
- Gaia Collaboration (Brown, A. G. A., et al.) 2021, *A&A*, **649**, A1
- Gaidos, E., Claytor, Z., Dunee, R., Ali, A., & Feiden, G. A. 2023, *MNRAS*, **520**, 5283
- Gibbs, A., Bixel, A., Rackham, B. V., et al. 2020, *AJ*, **159**, 169
- Giles, H. A. C., Collier Cameron, A., & Haywood, R. D. 2017, *MNRAS*, **472**, 1618
- Gillon, M., Jehin, E., Lederer, S. M., et al. 2016, *Nature*, **533**, 221
- Goldman, D. S., Henden, A. A., & Schuler, C. A. 2006, *JAAVSO*, **34**, 278
- González-Álvarez, E., Micela, G., Maldonado, J., et al. 2019, *A&A*, **624**, A27
- González-Álvarez, E., Zapatero Osorio, M. R., Caballero, J. A., et al. 2020, *A&A*, **637**, A93
- González-Álvarez, E., Petralia, A., Micela, G., et al. 2021, *A&A*, **649**, A157
- González-Álvarez, E., Kemmer, J., Chaturvedi, P., et al. 2023, *A&A*, **675**, A141
- Gordon, T. A., Davenport, J. R. A., Angus, R., et al. 2021, *ApJ*, **913**, 70
- Gorini, P., Kemmer, J., Dreizler, S., et al. 2023, *A&A*, **680**, A28
- Greimel, R., & Robb, R. M. 1998, *Information Bulletin on Variable Stars*, **4652**, 1
- Haghighipour, N., Vogt, S. S., Butler, R. P., et al. 2010, *ApJ*, **715**, 271
- Hallinan, G., Antonova, A., Doyle, J. G., et al. 2008, *ApJ*, **684**, 644
- Hartman, J. D., Bakos, G. Á., Noyes, R. W., et al. 2011, *AJ*, **141**, 166
- Hébrard, E. M., Donati, J. F., Delfosse, X., et al. 2016, *MNRAS*, **461**, 1465
- Hobson, M. J., Díaz, R. F., Delfosse, X., et al. 2018, *A&A*, **618**, A103
- Hobson, M. J., Delfosse, X., Astudillo-Defru, N., et al. 2019, *A&A*, **625**, A18
- Howard, A. W., Johnson, J. A., Marcy, G. W., et al. 2010, *ApJ*, **721**, 1467
- Howard, A. W., Marcy, G. W., Fischer, D. A., et al. 2014, *ApJ*, **794**, 51
- Howard, W. S., Corbett, H., Law, N. M., et al. 2020, *ApJ*, **895**, 140
- Irving, Z. A., Saar, S. H., Wargelin, B. J., & do Nascimento, J.-D., 2023, *ApJ*, **949**, 51
- Irwin, J., & Bouvier, J. 2009, in *The Ages of Stars*, eds. E. E. Mamajek, D. R. Soderblom, & R. F. G. Wyse, 258, 363
- Irwin, J., Berta, Z. K., Burke, C. J., et al. 2011, *ApJ*, **727**, 56
- Jeffers, S. V., Schöfer, P., Lamert, A., et al. 2018, *A&A*, **614**, A76
- Jeffers, S. V., Barnes, J. R., Schöfer, P., et al. 2022, *A&A*, **663**, A27
- Johnson, J. A., Butler, R. P., Marcy, G. W., et al. 2007, *ApJ*, **670**, 833
- Johnson, J. A., Howard, A. W., Marcy, G. W., et al. 2010, *PASP*, **122**, 149
- Johnson, E. N., Czesla, S., Fuhrmeister, B., et al. 2021, *A&A*, **651**, A105
- Kaminski, A., Trifonov, T., Caballero, J. A., et al. 2018, *A&A*, **618**, A115
- Kemmer, J., Stock, S., Kossakowski, D., et al. 2020, *A&A*, **642**, A236
- Kesseli, A. Y., Muirhead, P. S., Mann, A. W., et al. 2018, *AJ*, **155**, 225
- Kim, Y.-C., & Demarque, P. 1996, *ApJ*, **457**, 340
- Kiman, R., Schmidt, S. J., Angus, R., et al. 2019, *AJ*, **157**, 231
- Kinemuchi, K., Barclay, T., Fanelli, M., et al. 2012, *PASP*, **124**, 963
- Kiraga, M. 2012, *Acta Astron.*, **62**, 67
- Kiraga, M., & Stepień, K. 2007, *Acta Astron.*, **57**, 149
- Kiraga, M., & Stepień, K. 2013, *Acta Astron.*, **63**, 53
- Knutson, H. A., Madhusudhan, N., Cowan, N. B., et al. 2011, *ApJ*, **735**, 27
- Kochukhov, O. 2021, *A&A Rev.*, **29**, 1
- Kopparapu, R. K., Ramirez, R., Kasting, J. F., et al. 2013, *ApJ*, **765**, 131
- Kossakowski, D., Kürster, M., Trifonov, T., et al. 2023, *A&A*, **670**, A84
- Lafarga, M., Ribas, I., Reiniers, A., et al. 2021, *A&A*, **652**, A28
- Lalitha, S., Baroch, D., Morales, J. C., et al. 2019, *A&A*, **627**, A116
- Lammer, H., Selsis, F., Ribas, I., et al. 2003, *ApJ*, **598**, L121
- Lampón, M., López-Puertas, M., Czesla, S., et al. 2021, *A&A*, **648**, L7
- Lightkurve Collaboration (Cardoso, J. V. D. M., et al.) 2018, *Astrophysics Source Code Library* [record ascl:1812.013]
- Lothringer, J. D., Benneke, B., Crossfield, I. J. M., et al. 2018, *AJ*, **155**, 66
- Lu, Y. L., Angus, R., Curtis, J. L., David, T. J., & Kiman, R. 2021, *AJ*, **161**, 189
- Lu, Y., Angus, R., Foreman-Mackey, D., & Hattori, S. 2023, *AJ*, submitted [arXiv:2310.14990]
- Lu, Y. L., See, V., Amard, L., Angus, R., & Matt, S. P. 2024, *Nat. Astron.*, **8**, 223
- Luque, R., Nowak, G., Pallé, E., et al. 2018, *A&A*, **620**, A171
- Luque, R., Pallé, E., Kossakowski, D., et al. 2019, *A&A*, **628**, A39
- Luque, R., Fulton, B. J., Kunimoto, M., et al. 2022, *A&A*, **664**, A199
- Magaudá, E., Stelzer, B., Covey, K. R., et al. 2020, *A&A*, **638**, A20
- Magaudá, E., Stelzer, B., & Raetz, S. 2022a, *Astron. Nachr.*, **343**, e20220049
- Magaudá, E., Stelzer, B., Raetz, S., et al. 2022b, *A&A*, **661**, A29
- Mamajek, E. E., & Hillenbrand, L. A. 2008, *ApJ*, **687**, 1264
- Marfil, E., Tabernero, H. M., Montes, D., et al. 2021, *A&A*, **656**, A162
- Mazeh, T., Tamuz, O., & Zucker, S. 2007, in *Transiting Extrapolar Planets Workshop*, eds. C. Afonso, D. Weldrake, & T. Henning, *ASP Conf. Ser.*, **366**, 119
- McCully, C., Volgenau, N. H., Harbeck, D. R., et al. 2018, in *Software and Cyberinfrastructure for Astronomy V*, eds. J. C. Guzman, & J. Ibsen, *SPIE Conf. Ser.*, **10707**, 107070K
- McQuillan, A., Aigrain, S., & Mazeh, T. 2013a, *MNRAS*, **432**, 1203
- McQuillan, A., Mazeh, T., & Aigrain, S. 2013b, *ApJ*, **775**, L11
- McQuillan, A., Mazeh, T., & Aigrain, S. 2014, *ApJS*, **211**, 24
- Medina, A. A., Winters, J. G., Irwin, J. M., & Charbonneau, D. 2020, *ApJ*, **905**, 107
- Medina, A. A., Winters, J. G., Irwin, J. M., & Charbonneau, D. 2022, *ApJ*, **935**, 104
- Messina, S., Desidera, S., Lanzafame, A. C., Turatto, M., & Guinan, E. F. 2011, *A&A*, **532**, A10
- Montet, B. T., Crepp, J. R., Johnson, J. A., Howard, A. W., & Marcy, G. W. 2014, *ApJ*, **781**, 28
- Morales, J. C., Mustill, A. J., Ribas, I., et al. 2019, *Science*, **365**, 1441
- Morin, J., Donati, J. F., Petit, P., et al. 2008, *MNRAS*, **390**, 567
- Morin, J., Donati, J. F., Petit, P., et al. 2010, *MNRAS*, **407**, 2269
- Moutou, C., Hébrard, E. M., Morin, J., et al. 2017, *MNRAS*, **472**, 4563
- Nagel, E., Czesla, S., & Schmitt, J. H. M. M. 2016, *A&A*, **590**, A47
- Nagel, E., Czesla, S., Schmitt, J. H. M. M., et al. 2019, *A&A*, **622**, A153
- Newton, E. R., Irwin, J., Charbonneau, D., Berta-Thompson, Z. K., & Dittmann, J. A. 2016a, *ApJ*, **821**, L19
- Newton, E. R., Irwin, J., Charbonneau, D., et al. 2016b, *ApJ*, **821**, 93
- Newton, E. R., Irwin, J., Charbonneau, D., et al. 2017, *ApJ*, **834**, 85

- Newton, E. R., Mondrik, N., Irwin, J., Winters, J. G., & Charbonneau, D. 2018, *AJ*, **156**, 217
- Norton, A. J., Wheatley, P. J., West, R. G., et al. 2007, *A&A*, **467**, 785
- Noyes, R. W., Hartmann, L. W., Baliunas, S. L., Duncan, D. K., & Vaughan, A. H. 1984, *ApJ*, **279**, 763
- Núñez, A., Agüeros, M. A., Covey, K. R., et al. 2022, *ApJ*, **931**, 45
- Nutzman, P., & Charbonneau, D. 2008, *PASP*, **120**, 317
- Oelkers, R. J., Rodríguez, J. E., Stassun, K. G., et al. 2018, *AJ*, **155**, 39
- Oláh, K., Kóvári, Z., Petrovay, K., et al. 2016, *A&A*, **590**, A133
- Oshagh, M., Santos, N. C., Ehrenreich, D., et al. 2014, *A&A*, **568**, A99
- Owen, J. E., & Jackson, A. P. 2012, *MNRAS*, **425**, 2931
- Pallavicini, R., Golub, L., Rosner, R., et al. 1981, *ApJ*, **248**, 279
- Palle, E., Orell-Miquel, J., Brady, M., et al. 2023, *A&A*, **678**, A80
- Parker, E. N. 1955, *ApJ*, **122**, 293
- Pass, E. K., Charbonneau, D., Irwin, J. M., & Winters, J. G. 2022, *ApJ*, **936**, 109
- Pass, E. K., Winters, J. G., Charbonneau, D., Irwin, J. M., & Medina, A. A. 2023, *AJ*, **166**, 16
- Passeyger, V. M., Schweitzer, A., Shulyak, D., et al. 2019, *A&A*, **627**, A161
- Perdelwitz, V., Mittag, M., Tal-Or, L., et al. 2021, *A&A*, **652**, A116
- Perger, M., Scandariato, G., Ribas, I., et al. 2019, *A&A*, **624**, A123
- Perryman, M. 2018, *The Exoplanet Handbook* (Cambridge: Cambridge University Press)
- Pinamonti, M., Sozzetti, A., Giacobbe, P., et al. 2019, *A&A*, **625**, A126
- Pizzolato, N., Maggio, A., Micela, G., Sciortino, S., & Ventura, P. 2003, *A&A*, **397**, 147
- Plavchan, P., Barclay, T., Gagné, J., et al. 2020, *Nature*, **582**, 497
- Pojmanski, G., Pilecki, B., & Szczygiel, D. 2005, *Acta Astron.*, **55**, 275
- Pollacco, D. L., Skillen, I., Collier Cameron, A., et al. 2006, *PASP*, **118**, 1407
- Popinchalk, M., Faherty, J. K., Kiman, R., et al. 2021, *ApJ*, **916**, 77
- Quirrenbach, A., Amado, P. J., Caballero, J. A., et al. 2014, in *Ground-based and Airborne Instrumentation for Astronomy V*, eds. S. K. Ramsay, I. S. McLean, & H. Takami, *SPIE Conf. Ser.*, **9147**, 91471F
- Quirrenbach, A., Amado, P. J., Ribas, I., et al. 2018, in *Ground-based and Airborne Instrumentation for Astronomy VII*, eds. C. J. Evans, L. Simard, & H. Takami, *SPIE Conf. Ser.*, **10702**, 107020W
- Quirrenbach, A., CARMENES Consortium, Amado, P. J., et al. 2020, *SPIE Conf. Ser.*, **11447**, 114473C
- Quirrenbach, A., Passeyger, V. M., Trifonov, T., et al. 2022, *A&A*, **663**, A48
- Rackham, B. V., Apai, D., & Giampapa, M. S. 2018, *ApJ*, **853**, 122
- Raetz, S., Stelzer, B., Damasso, M., & Scholz, A. 2020, *A&A*, **637**, A22
- Ramsay, G., Doyle, J. G., & Doyle, L. 2020, *MNRAS*, **497**, 2320
- Rebull, L. M., Stauffer, J. R., Cody, A. M., et al. 2018, *AJ*, **155**, 196
- Reiners, A., & Basri, G. 2008, *ApJ*, **684**, 1390
- Reiners, A., & Mohanty, S. 2012, *ApJ*, **746**, 43
- Reiners, A., & Schmitt, J. H. M. M. 2003, *A&A*, **398**, 647
- Reiners, A., Schüssler, M., & Passeyger, V. M. 2014, *ApJ*, **794**, 144
- Reiners, A., Ribas, I., Zechmeister, M., et al. 2018a, *A&A*, **609**, L5
- Reiners, A., Zechmeister, M., Caballero, J. A., et al. 2018b, *A&A*, **612**, A49
- Reiners, A., Shulyak, D., Käpylä, P. J., et al. 2022, *A&A*, **662**, A41
- Reinhold, T., & Hekker, S. 2020, *A&A*, **635**, A43
- Reinhold, T., Reiners, A., & Basri, G. 2013, *A&A*, **560**, A4
- Ribas, I., Guinan, E. F., Güdel, M., & Audard, M. 2005, *ApJ*, **622**, 680
- Ribas, I., Tuomi, M., Reiners, A., et al. 2018, *Nature*, **563**, 365
- Ribas, I., Reiners, A., Zechmeister, M., et al. 2023, *A&A*, **670**, A139
- Ricker, G. R., Winn, J. N., Vanderspek, R., et al. 2015, *JATIS*, **1**, 014003P
- Rivera, E. J., Lissauer, J. J., Butler, R. P., et al. 2005, *ApJ*, **634**, 625
- Sabotta, S., Schlecker, M., Chaturvedi, P., et al. 2021, *A&A*, **653**, A114
- Sanz-Forcada, J., Micela, G., Ribas, I., et al. 2011, *A&A*, **532**, A6
- Sarkis, P., Henning, T., Kürster, M., et al. 2018, *AJ*, **155**, 257
- Schöfer, P., Jeffers, S. V., Reiners, A., et al. 2019, *A&A*, **623**, A44
- Schöfer, P., Jeffers, S. V., Reiners, A., et al. 2022, *A&A*, **663**, A68
- Schweitzer, A., Passeyger, V. M., Cifuentes, C., et al. 2019, *A&A*, **625**, A68
- Sibony, Y., Helled, R., & Feldmann, R. 2022, *MNRAS*, **513**, 2057
- Stelzer, B., Damasso, M., Scholz, A., & Matt, S. P. 2016, *MNRAS*, **463**, 1844
- Stock, S., Kemmer, J., Reffert, S., et al. 2020a, *A&A*, **636**, A119
- Stock, S., Nagel, E., Kemmer, J., et al. 2020b, *A&A*, **643**, A112
- Suárez Mascareño, A., Rebolo, R., González Hernández, J. I., & Esposito, M. 2015, *MNRAS*, **452**, 2745
- Suárez Mascareño, A., Rebolo, R., & González Hernández, J. I. 2016, *A&A*, **595**, A12
- Suárez Mascareño, A., González Hernández, J. I., Rebolo, R., et al. 2017a, *A&A*, **605**, A92
- Suárez Mascareño, A., Rebolo, R., González Hernández, J. I., & Esposito, M. 2017b, *MNRAS*, **468**, 4772
- Suárez Mascareño, A., Rebolo, R., González Hernández, J. I., et al. 2018, *A&A*, **612**, A89
- Suárez Mascareño, A., González-Álvarez, E., Zapatero Osorio, M. R., et al. 2023, *A&A*, **670**, A5
- Tal-Or, L., Zechmeister, M., Reiners, A., et al. 2018, *A&A*, **614**, A122
- Tamuz, O., Mazeh, T., & Zucker, S. 2005, *MNRAS*, **356**, 1466
- Terrien, R. C., Keen, A., Oda, K., et al. 2022, *ApJ*, **927**, L11
- Testa, P., Drake, J. J., & Peres, G. 2004, *ApJ*, **617**, 508
- Toledo-Adrón, B., González Hernández, J. I., Rodríguez-López, C., et al. 2019, *MNRAS*, **488**, 5145
- Toledo-Adrón, B., Suárez Mascareño, A., González Hernández, J. I., et al. 2021, *A&A*, **648**, A20
- Trifonov, T., Kürster, M., Zechmeister, M., et al. 2018, *A&A*, **609**, A117
- Trifonov, T., Lee, M. H., Kürster, M., et al. 2020, *A&A*, **638**, A16
- Trifonov, T., Caballero, J. A., Morales, J. C., et al. 2021, *Science*, **371**, 1038
- Venuti, L., Bouvier, J., Cody, A. M., et al. 2017, *A&A*, **599**, A23
- Vida, K., Kóvári, Z., Pál, A., Oláh, K., & Kriskovics, L. 2017, *ApJ*, **841**, 124
- Voges, W., Aschenbach, B., Boller, T., et al. 1999, *A&A*, **349**, 389
- Walkowicz, L. M., & Basri, G. S. 2013, *MNRAS*, **436**, 1883
- Watson, C. L., Henden, A. A., & Price, A. 2006, *Soc. Astron. Sci. Ann. Symp.*, **25**, 47
- West, A. A., Hawley, S. L., Bochanski, J. J., et al. 2008, *AJ*, **135**, 785
- West, A. A., Weisenburger, K. L., Irwin, J., et al. 2015, *ApJ*, **812**, 3
- Wright, N. J., Drake, J. J., Mamajek, E. E., & Henry, G. W. 2011, *ApJ*, **743**, 48
- Wright, D. J., Wittenmyer, R. A., Tinney, C. G., Bentley, J. S., & Zhao, J. 2016, *ApJ*, **817**, L20
- Wright, N. J., Newton, E. R., Williams, P. K. G., Drake, J. J., & Yadav, R. K. 2018, *MNRAS*, **479**, 2351
- Zechmeister, M., & Kürster, M. 2009, *A&A*, **496**, 577
- Zechmeister, M., Dreizler, S., Ribas, I., et al. 2019, *A&A*, **627**, A49

- ¹ Centre for Planetary Habitability, Department of Geosciences, University of Oslo, Sem Saelands vei 2b, 0315 Oslo, Norway
- ² Institut für Astrophysik, Georg-August-Universität, Friedrich-Hund-Platz 1, 37077 Göttingen, Germany
e-mail: yutong.shan@uni-goettingen.de
- ³ Departamento de Física de la Tierra y Astrofísica and IPARCOS-UCM (Instituto de Física de Partículas y del Cosmos de la UCM), Facultad de Ciencias Físicas, Universidad Complutense de Madrid, 28040 Madrid, Spain
- ⁴ Instituto de Astrofísica de Andalucía (CSIC), Glorieta de la Astronomía s/n, 18008 Granada, Spain
- ⁵ Instituto de Astrofísica de Canarias, Via Láctea s/n, 38205 La Laguna, Tenerife, Spain
- ⁶ Departamento de Astrofísica, Universidad de La Laguna, 38206 La Laguna, Tenerife, Spain
- ⁷ Centro de Astrobiología (CSIC-INTA), ESAC campus, Camino bajo del castillo s/n, 28692 Villanueva de la Cañada, Madrid, Spain
- ⁸ Hamburger Sternwarte, Universität Hamburg, Gojenbergsweg 112, 21029 Hamburg, Germany
- ⁹ Centre for Mathematical Plasma Astrophysics, Katholieke Universiteit Leuven, Celestijnenlaan 200B, bus 2400, 3001 Leuven, Belgium
- ¹⁰ Institut de Ciències de l'Espai (ICE, CSIC), Campus UAB, Can Magrans s/n, 08193 Bellaterra, Spain
- ¹¹ Institut d'Estudis Espacials de Catalunya (IEEC), 08034 Barcelona, Spain
- ¹² Landessternwarte, Zentrum für Astronomie der Universität Heidelberg, Königstuhl 12, 69117 Heidelberg, Germany
- ¹³ AstroLAB IRIS, Provinciaal Domein "De Palingbeek", Verbrandemolenstraat 5, 8902 Zillebeke, Ieper, Belgium
- ¹⁴ Vereniging Voor Sterrenkunde, Oude Bleken 12, 2400 Mol, Belgium
- ¹⁵ Max-Planck-Institut für Astronomie, Königstuhl 17, 69117 Heidelberg, Germany
- ¹⁶ Max-Planck-Institut für Sonnensystemforschung, Justus-von-Liebig-Weg 3, 37077 Göttingen, Germany
- ¹⁷ School of Physics & Astronomy, University of Birmingham, Edgbaston, Birmingham B15 2TT, UK
- ¹⁸ Thüringer Landessternwarte Tautenburg, Sternwarte 5, 07778 Tautenburg, Germany
- ¹⁹ Department of Physics, Ariel University, Ariel 40700, Israel
- ²⁰ Center for Astroparticles and High Energy Physics (CAPA), Universidad de Zaragoza, 50009 Zaragoza, Spain
- ²¹ School of Sciences, European University Cyprus, Diogenes street, Engomi 1516 Nicosia, Cyprus
- ²² Department of Physics, University of Warwick, Gibbet Hill Road, Coventry CV4 7AL, UK

Appendix A: Outliers

A.1. Literature comparison outliers

Below, we list and discuss the discrepant periods between this work and the literature described in Section 4.2 and shown in Fig. 3. We distinguish between cases where the periods are likely harmonically related (Sect. A.1.1) and those lacking a straightforward explanation (Sect. A.1.2). We note again that this is not an exhaustive list of all instances where measured periods disagree. Instead, these examples illustrate the type and extent of deviations confronted, as well as the thought processes and evidence used to decide on the best period we adopt. For each case, we also present final period assessments, following the reasoning described here and mirroring the guidelines given in Sect. 4.5.

A.1.1. Harmonics

When two contending periods are harmonics of each other, it is in general expected that one of them, typically the larger one, is correct. This is because the first harmonic of the true period can manifest itself as the prevailing period of modulation when, for example, the star's spot distribution is bimodal across its hemispheres, resulting in a 'double-dipping' feature throughout each full rotation (e.g., Basri & Shah 2020; Jeffers et al. 2022; Schöfer et al. 2022). On the other hand, there is no simple mechanism that may explain the production of one dip over two rotations. While the double-dip phenomenon is usually temporary and minute differences in the dip morphologies may be resolved with high-precision, high-cadence photometric data, it is more difficult to distinguish nearly equal-sized dips in ground-based data or data that cover only a short time baseline. We evaluate the following cases with this principle in mind.

J01019+541. The best TESS period of 0.139 d is exactly half that from MEarth data 0.278 d (DA19, Newton et al. 2016b). We give preference to the longer period from the literature.

J04173+088. The period of this fast rotator was measured to be 0.185 d using MEarth data (West et al. 2015). However, both the TESS light curve and SuperWASP data spanning 6 seasons unambiguously indicate a period of 0.3697 d, exactly twice as long (see discussion in Johnson et al. 2021). We strongly favour the longer period from our work.

J10182–204. Baroch et al. (2018) obtained a period of 7.3 d from archival SuperWASP data. TESS SAP light curves resolve a double-dipping modulation pattern with periodicity twice that at 14.5 d, which we deem to be convincing.

J16581+257. The period measured from one season of SuperWASP observations is 11.73 d, about half that reported from ASAS data in the literature (23.8 d, DA19, Oelkers et al. 2018). We consider the longer periods to be correct.

J20450+444. DA19 measured a 19.9 d period from archival SuperWASP data. However, a period of ~ 39 d, about twice the literature period, is implicated in spectroscopic indicators (the two Ca-IRT lines, H α , and TiO). In fact, TESS SAP light curves also rule the shorter period for J20450+444 as implausible. Therefore, we update this period to the longer one from our work.

In a couple of cases, there is additional evidence in favour of the shorter period:

J06371+175. A 37 d period is strongly implicated by APT photometry presented in the planet discovery paper of Luque et al. (2022) and also significant in both seasons of SuperWASP data. Although the second season of SuperWASP data

slightly prefers a ~ 74 d period, we still adopted the shorter period.

J20525–169. The literature period is ~ 68 d (ASAS, DA19, Suárez Mascareño et al. 2016) or 85 d (MEarth, Newton et al. 2018), which are approximately yearly aliases of one another, and 134 d from our work in H α and Ca-IRTb, nearly exactly twice the ASAS period. We adopted the 68 d period but note that it is 'debated'.

A.1.2. Other discrepant cases

J03213+799. The literature measurement of 32.4 d is based on photometric data from AstroLAB that were available at the time. In this work, we perform a new analysis using a more complete light curve from AstroLAB. To be conservative, we indicate that the new period is still 'debated' and would benefit from further confirmation.

J03463+262. The literature value of ~ 16 d comes from KELT photometry (Oelkers et al. 2018), and is supported by SuperWASP data as well as Ca-IRTa. However, multiple spectroscopic indicators H α , Ca-IRTb, and TiO show a ~ 10 d period. We prefer the value derived from photometry, but indicate that it is 'debated'.

J04153–076. This active mid-M dwarf ($pEW'_{H\alpha} = -3.3\text{\AA}$) is expected to have a relatively short period. Using CARMENES data, Lafarga et al. (2021) detected a significant signal at 1.8 d in three spectroscopic indicators: RV, CRX, and BIS. With the latest spectroscopic time series, we detect a 8.56 d period in the two Ca-IRTb lines. The measured $v \sin i = 2.2$ km/s indicates that the $P_{\text{rot}} \lesssim 6$ d, slightly preferring the value from Lafarga et al. (2021). However, the limited precision in $v \sin i$ means the 8 d period can also be easily accommodated. We take the period in this work as the nominal 'best' period, but designate it as 'debated'.

J05337+019. This object is an SB1 analyzed in detail by Baroch et al. (2021). The rotation period of 0.6 d robustly determined from TESS (see Figure C.2) and unbinned SuperWASP data agree with each other and also with the orbital period of the binary, as measured from RV, which is consistent with tidal synchronization. One of the reported periods in the literature is 2.8 d, which is an alias of the 0.6 d period. Therefore, we are confident in the 0.6 d period derived in this work and assign it a 'secure' rating.

J09140+196. The literature period of 89.9 d comes from DA19's analysis of archival ASAS data, whereas the SuperWASP data exhibit an unequivocal sinusoidal signal at 39 d over a 127 d time baseline. The same SuperWASP data were analyzed in Baroch et al. (2021), reaching a similar value. It is possible that the two periods are harmonically related. However, a reanalysis of the data used by DA19 shows that the 89.9 d peak, while formally significant, competes with many other peaks of similar or greater height, therefore cannot be unambiguously interpreted. Therefore, we prefer the ~ 39 d period, but indicate it as 'provisional'.

J11000+228. The literature period is 171 d from longitudinal B-fields (Donati et al. 2023), which is rather long for an early-M dwarf. We see a much shorter, 53 d period in both TiO and R'_{HK} time series, corroborated at least tentatively by SuperWASP light curves. We deem our period to be more reasonable, and brand it as 'secure' owing to multiple lines of support.

J11509+483. This star has many reported periods in the literature. Earlier works measured a period of ~ 125 d (Irwin et al. 2011; Newton et al. 2016b; Díez Alonso et al. 2019), all based on MEarth data. However, a new analysis of the latest MEarth data presented a longer period at 149 d (Medina et al. 2022), and subsequent measurements using spectropolarimetric time

series support this longer period of Medina et al. (2022; 158 d and 176 d, Fouqué et al. 2023; Donati et al. 2023, respectively). Three of our spectroscopic indicator time series ($H\alpha$, Ca-IRTb, TiO) show an ~ 83 d period, which could represent the first harmonic of the longer periods. We list the P_{rot} of Medina et al. (2022), the middle ground within $\sim 15\%$ of all the available measurements, as the best period with a ‘secure’ rating.

J12230+640. The literature period of 32.9 d originates from the analysis of archival NSVS photometry data by DA19. The Ca-IRT time series contains 151 epochs and reveals a 51.5 d signal, which incidentally coincides with a smaller peak in the NSVS data. While we deem the photometric period more likely to be correct, the veracity of the other signal cannot be ruled out. Therefore, we list the DA19 period as the best period with a ‘debated’ designation.

J14257+236E. The period from DA19 is 17.6 d and is derived from unbinned public SuperWASP data. A reanalysis of the same data with daily binning shows that this peak, while present, is not formally significant. Multiple spectroscopic indicators ($H\alpha$, Ca-IRT) reflect a period of ~ 12.8 d, casting further doubt into the photometric period but not enough to flat-out refute it. Therefore, we list the DA19 period as the best period but flag it as ‘debated’.

J14321+081. The 0.757 d period comes from MEarth data recently presented by Pass et al. (2023) and previously by Newton et al. (2016b) as a ‘U’-rotator. This is a very faint ($V > 15$ mag) but very active late-M star whose $v \sin i$ bounds the period to $\lesssim 1.7$ d (see also Section 4.3). While our unbinned SuperWASP data exhibit a highly significant period at 1.115 d and 1.025 d (and their aliases) in the first season, the weight of the two agreeing literature values tips the value in favour of the shorter period, which we indicate as ‘secure’.

J19346+045. The literature value of 12.9 d (DA19) is from ASAS photometry with FAP = 0.33%. We find a 21.8 d period in $H\alpha$ and Ca-IRTab. An identical period in dLW (Lafarga et al. 2021) strengthens our preference for the longer period measured in this work, which we assign as the best period with a rating of ‘secure’.

J23381–162. The literature value of 61.66 d comes from Watson et al. (2006), which refers to the AAVSO database of variable stars. The SuperWASP data show conflicting periods (therefore a U-designation). While there is a large-amplitude sinusoidal signal of ~ 91 d in season 6, a similarly clear signal at ~ 54 d in season 7 is only slightly less formally significant. In summary, we consider the evidence insufficient to reject the period in the literature, though flag it as ‘debated’.

A.2. $v \sin i$ outliers

Here we list and describe the $v \sin i$ outliers as shown in Figure 4 in Section 4.3.

J05337+019. This is an SB1 analyzed in detail in Baroch et al. (2021), with the companion suspected to be a white dwarf (See also Section A.1). The $v \sin i$ measurement implicates a maximum rotation period of 2.5 d (1σ : 3.2 d), which is completely consistent with the rotational modulation of 0.6 d well-resolved in TESS and SuperWASP data. Oelkers et al. (2018) found a period of 2.8 d, which is an alias of 0.6 d. The clearly contradicting period that appears in Fig. 4 is 18.6 d from Howard et al. (2020).

J10584–107. The $v \sin i$ measurement implicates a maximum rotation period of 3.7 d (1σ : 13 d). The SuperWASP data give a 28 d period which, as discussed in Section 3.1.1, is suspected to be moon-related and likely to be unreliable.

J18356+329. With $P_{\text{rot}} \sim 0.1$ d, this is the fastest rotator in the sample. $P_{\text{max}} = 0.089$ d and the 1σ upper bound is 0.103 d, which is only marginally exceeded by the photometrically-measured P_{rot} of 0.118 d (e.g., DA19, TESS). The discrepancy could be easily accounted for if the error on either $v \sin i$ or R_* is slightly underestimated.

J19169+051S. This very late-type (M8V) and faint star is in a wide binary with J19169+051N (73’’8). It exhibits very large $H\alpha$ activity, although at its radius ($\sim 0.1R_*$) the saturation period is ~ 150 d (see Section 5.1), which implies that even extremely slow rotators can be expected to display considerable level of activity. The $v \sin i$ measurement constrains the maximum period to be ~ 1.4 d (1σ upper limit is 3.2 d), which severely contradicts the photometric rotation period of 23.6 d reported by DA19. However, it is worth noting that the DA19 period comes from MEarth, the same data that led Newton et al. (2016b) to conclude that no reliable period can be derived.

J06574+740, J20305+654. The measured P_{rot} for these stars exceed their expected $P_{\text{rot,max}}$ by 16%, just over the threshold of 15%. They could be easily explained if errors in the stellar radius or rotational velocity are slightly underestimated. J06574+740 is interesting because its light curve from every sector shows a beat pattern of two closely-spaced frequencies at 0.61 and 0.63 d (see Fig. C.3). This star is catalogued in *Gaia* as a duplicate source and has a high astrometric excess noise. Furthermore, it has been classified as RV-loud after the criteria of Tal-Or et al. (2018), exhibiting peak-to-peak RV variability of > 600 m/s over 11 epochs of monitoring (spread over 450 d). Both clues indicate that this object could be an unresolved binary. However, in this interpretation, the apparent spin-synchronization of the binary components at ~ 0.6 d is more difficult to explain. The RV amplitude of an equal-mass binary consistent with the observed spectral type and spin-orbit synchronized at 0.6 d is expected to be of order ~ 100 km/s. On the other hand, the fact that J06574+740 does not show overluminosity in a colour-magnitude diagram argues against the binary hypothesis. The beating pattern could also be due to two latitudinally displaced spots exhibiting differential rotation (see, e.g., Nage et al. 2016). In both possible scenarios, the modulation signal is attributed to rotation and has relatively good consistency with the measured $H\alpha$ activity and $v \sin i$. We consider the most significant of the two peaks at 0.61 d to be the ‘securely’ determined P_{rot} for this target, and recommend follow-up observations to resolve the nature of this system.

A.3. $pEW'_{H\alpha}$ outliers

In Fig. 5 of Sect. 4.4, the clump of extreme outliers with $P_{\text{rot}} \lesssim 1$ d correspond to measurements from Oelkers et al. (2018, J00184+440, J09439+269, J17115+384, J22115+184) and a ‘U’ rotator from Newton et al. (2016b, J01026+623). All five stars have $v \sin i < 2$ km/s which, given their radii, rules out $P_{\text{rot}} < 1$ d in all but a narrow range of inclination angles. All except J00184+440 have alternative P_{rot} measurements in the literature longwards of 10 d.

The rest of the points in this quadrant have modestly rapid rotations with $3 \text{ d} \lesssim P_{\text{rot}} < 10 \text{ d}$. Though closer to the overall trend, there are reasons to suspect these particular periods may be unreliable. The periods for J04225+105, J08119+087 and J14155+046 are measured from MEarth light curves by DA19 and Baroch et al. (2018), but have been deemed ‘N’ rotators by Newton et al. (2016b) who analysed the same data. The period of J09561+627 is 8.54 d according to Oelkers et al. (2018), which is about half of the ~ 18 d measured by Lafarga et al. (2021)

and 16.9 d from TESS SAP in this work, as discussed in Section 4.2. The sub-10 d periods of J16554–083N, J19072+208, and J20567–104 were measured by DA19 from rather noisy ASAS data, the latter two with non-trivial FAPs (0.91 % and 0.28%).

Appendix B: Rossby number computation

Since the dynamo mechanism relies on the motion of charged fluids in the stellar interior, stellar rotation and convection are thought to be relevant. Leading theories posit that if the timescale of rotation is short compared with that of convection, then the dynamo would operate efficiently, inducing more vigorous magnetic field generation (e.g., Parker 1955; Durney & Latour 1978; Noyes et al. 1984). Therefore, a commonly used parameter in physically connecting stellar rotation and activity phenomena is the Rossby number (Ro), a dimensionless quantity that characterizes the ratio between the two timescales: $Ro \equiv P_{\text{rot}}/\tau_{\text{conv}}$. τ_{conv} is the convective overturn time and depends on the stellar type, but cannot be directly measured. While theoretical calculations of τ_{conv} are becoming available (e.g., Kim & Demarque 1996), they are subject to stellar model assumptions and, importantly, do not work for fully convective stars. In practice, τ_{conv} is often estimated empirically from minimizing the scatter in observed activity–rotation relations (e.g., Pizzolato et al. 2003; Kiraga & Stepien 2007; Wright et al. 2011). A recent calibration as a function of $(V - K_s)$ colour comes from Wright et al. (2018), which is applicable across the entire M dwarf range:

$$\log \tau_{\text{conv}} = 0.64^{+0.1}_{-0.12} + 0.25^{+0.08}_{-0.07} (V - K_s). \quad (\text{B.1})$$

The relation is also given in terms of M_\star as follows (Wright et al. 2018):

$$\log \tau_{\text{conv}} = 2.33^{+0.06}_{-0.05} - 1.50^{+0.21}_{-0.20} (M_\star/M_\odot) + 0.31^{+0.16}_{-0.17} (M_\star/M_\odot)^2. \quad (\text{B.2})$$

These relations supersede the previous widely-used versions from Wright et al. (2011). The earlier version is less accurate for late-type stars, deviating from the updated one by up to $\sim +0.2$ dex.

An alternative prescription, used by Reiners et al. (2022), is given in terms of L_\star : $\tau_{\text{conv}} = 12.3\text{d} \times (L_{\text{bol}}/L_\odot)^{-1/2}$. Figure B.1

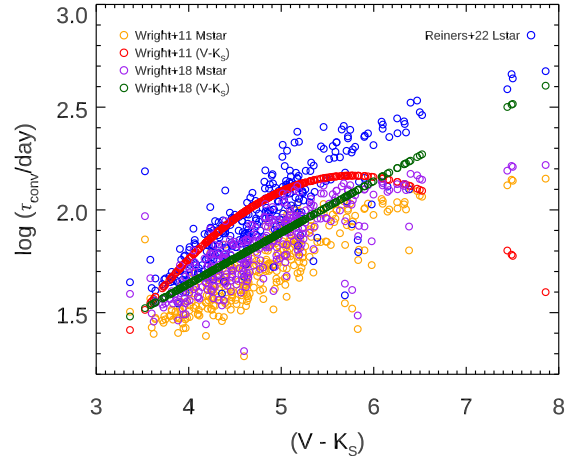


Fig. B.1. Systemtic differences in calculated τ_{conv} from popular formulae for our sample, which can result in differences in Ro .

shows the τ_{conv} versus $(V - K_s)$ resulting from using different version of the relations for our sample.

A number of authors have also remarked that activity measures, when not luminosity normalized, are tightly correlated with rotation period itself, and that τ_{conv} in fact has a similar scaling with colour as L_{bol} . Therefore, the significance of the Ro as the fundamental determinant of magnetic activity over the simple and more readily measured P_{rot} has been questioned (e.g., Pizzolato et al. 2003; Reiners et al. 2014). Furthermore, Reiners et al. (2014) advocated for the utility of the generalized Rossby number $P_{\text{rot}}^{-2} R_\star^{-4}$, demonstrating that it provides a slightly tighter relation with normalized X-ray luminosity over a wide range of dwarf spectral types (F to M) than the traditional Ro . Nevertheless, many activity–rotation studies continue to use Ro . In order to facilitate direct comparison with results from the literature, we present most of our activity–rotation relations in terms of Ro . We use $(V - K_s)$ colours from Cifuentes et al. (2020) and Eqn. B.1 combined with the measured P_{rot} , where available, to compute Ro for our sample. For the stars without a V -mag measurement in our sample, we used the $M_\star - Ro$ relation given in Equation B.2.

Appendix C: Long tables and additional figures

Tables C.1, C.2, and C.4 are available in their entirety in electronic form at the CDS via anonymous ftp to cdsarc.u-

strasbg.fr (130.79.128.5) or via <http://cdsweb.u-strasbg.fr/cgi-bin/qcat?J/A+A/>. Below we show representative snapshots of each table to provide guidance on their content.

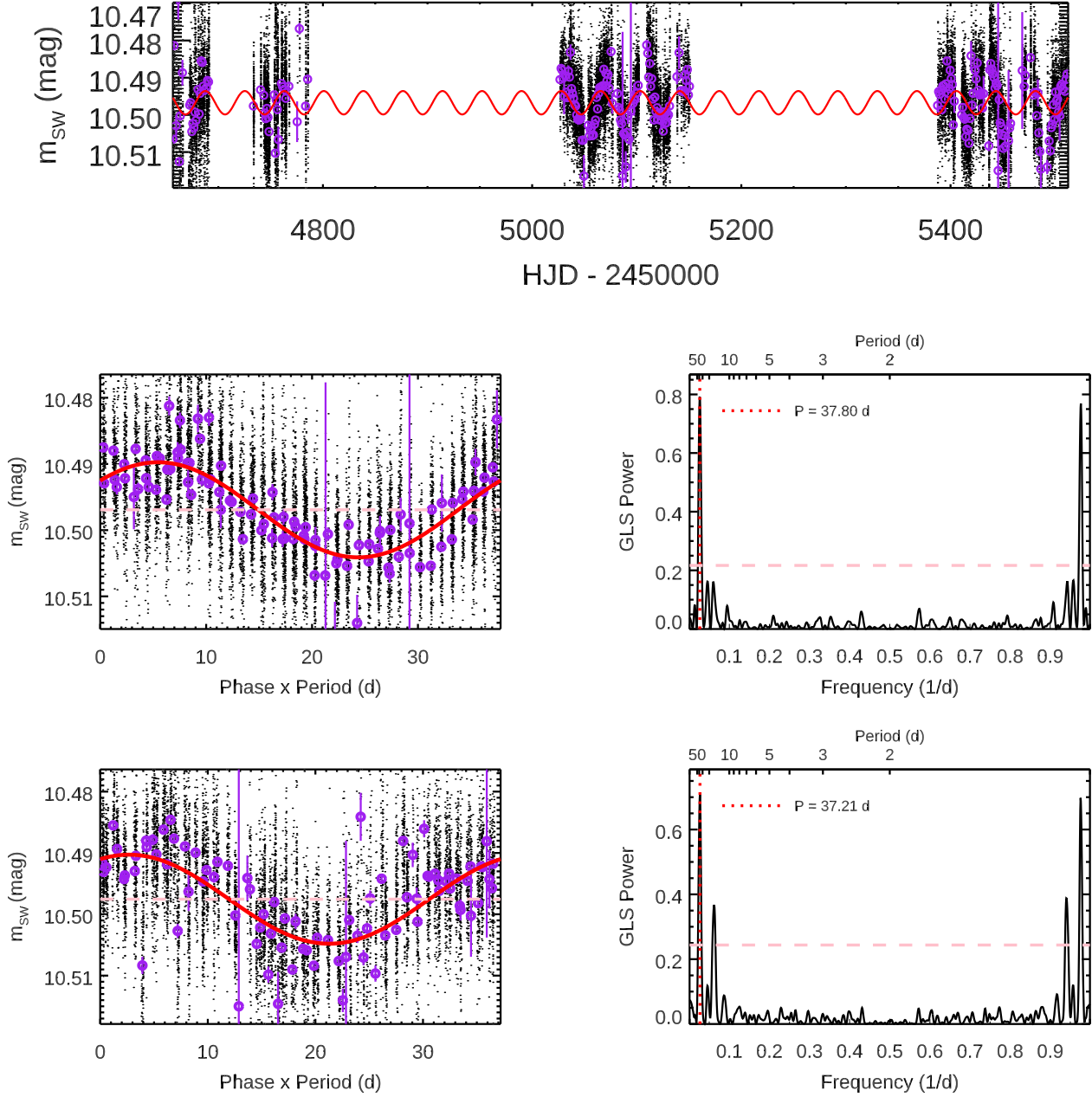


Fig. C.1. Example SuperWASP light curve for J22330+093. Top: all three seasons with black dots being the data points at every epoch. The purple circles and corresponding error bars represent the daily-binned points, computed as described in the text. In red we overplot the sinusoid parametrized by the best period from the second season. The best period is at 37.8 d in the second season (HJD \sim 5100, middle panels) and agrees well with that in season 3 (37.2 d, HJD \sim 5400, bottom panels). The pink dashed line in the light curve denotes the best-fit mean magnitudes, whereas in the periodograms it corresponds to FAP = 0.1%.

Karmn J05337+019 = V371 Ori

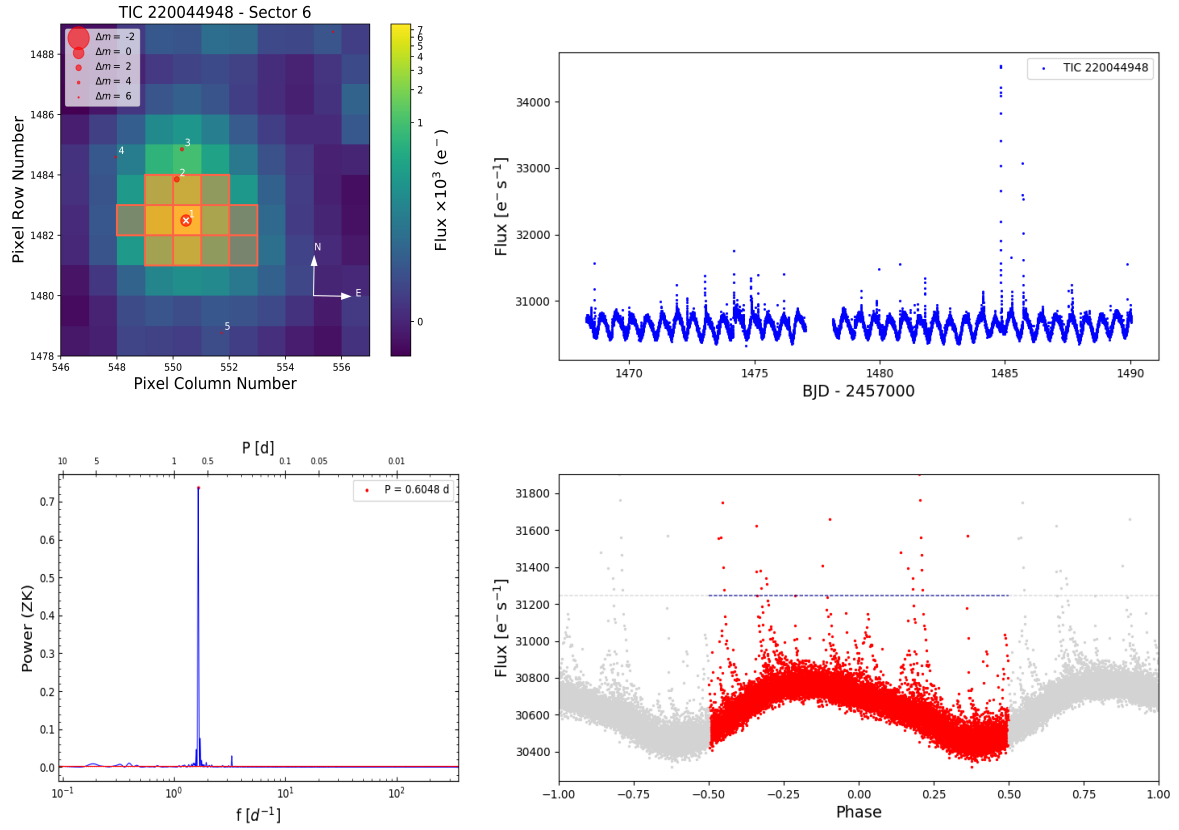


Fig. C.2. Summary page for the analysis of PDCSAP light curves from J05337+019, TESS sector 6. Top left: target pixel map; top right: PDCSAP light curve; bottom left: GLS periodogram; bottom right: light curve phase-folded on the peak period (0.6048 d).

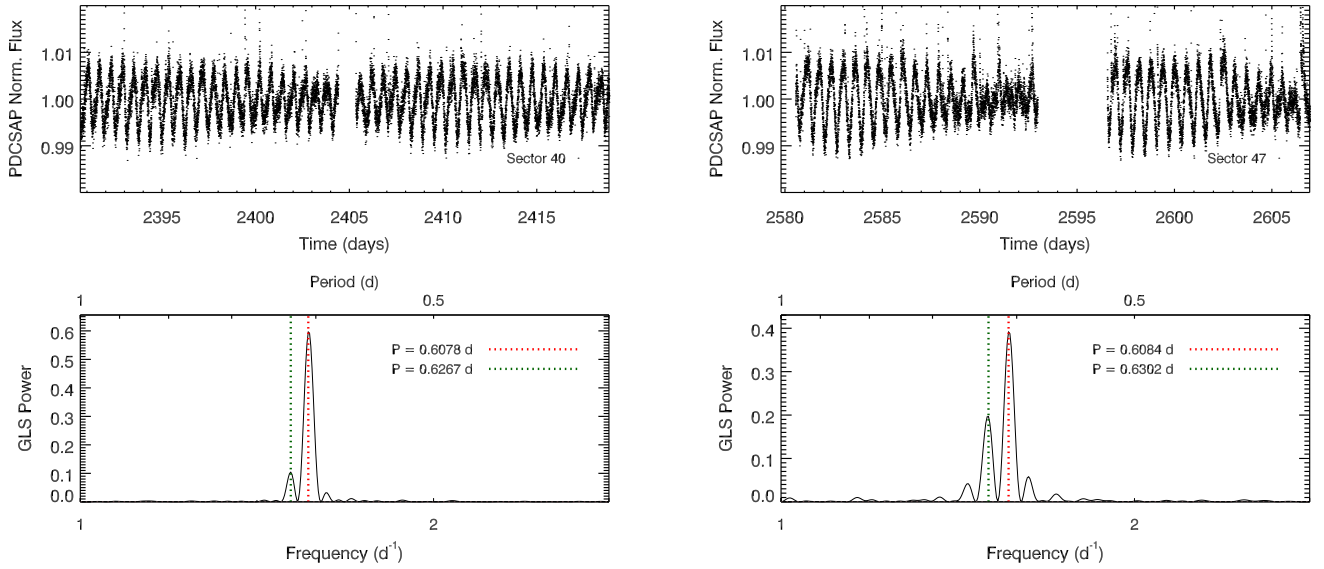


Fig. C.3. TESS light curve analysis for J06574+740. Top: PDCSAP light curves for J06574+740 from sector 40 (left) and 47 (right). The light curves exhibit a ‘beating’ pattern, suggestive of there being two stars with very similar rotation periods. Bottom: periodograms showing a main peak at 0.608 d and a smaller but still highly significant peak at ~ 0.63 d, which could be the rotational signal from a binary companion or from differential rotation.

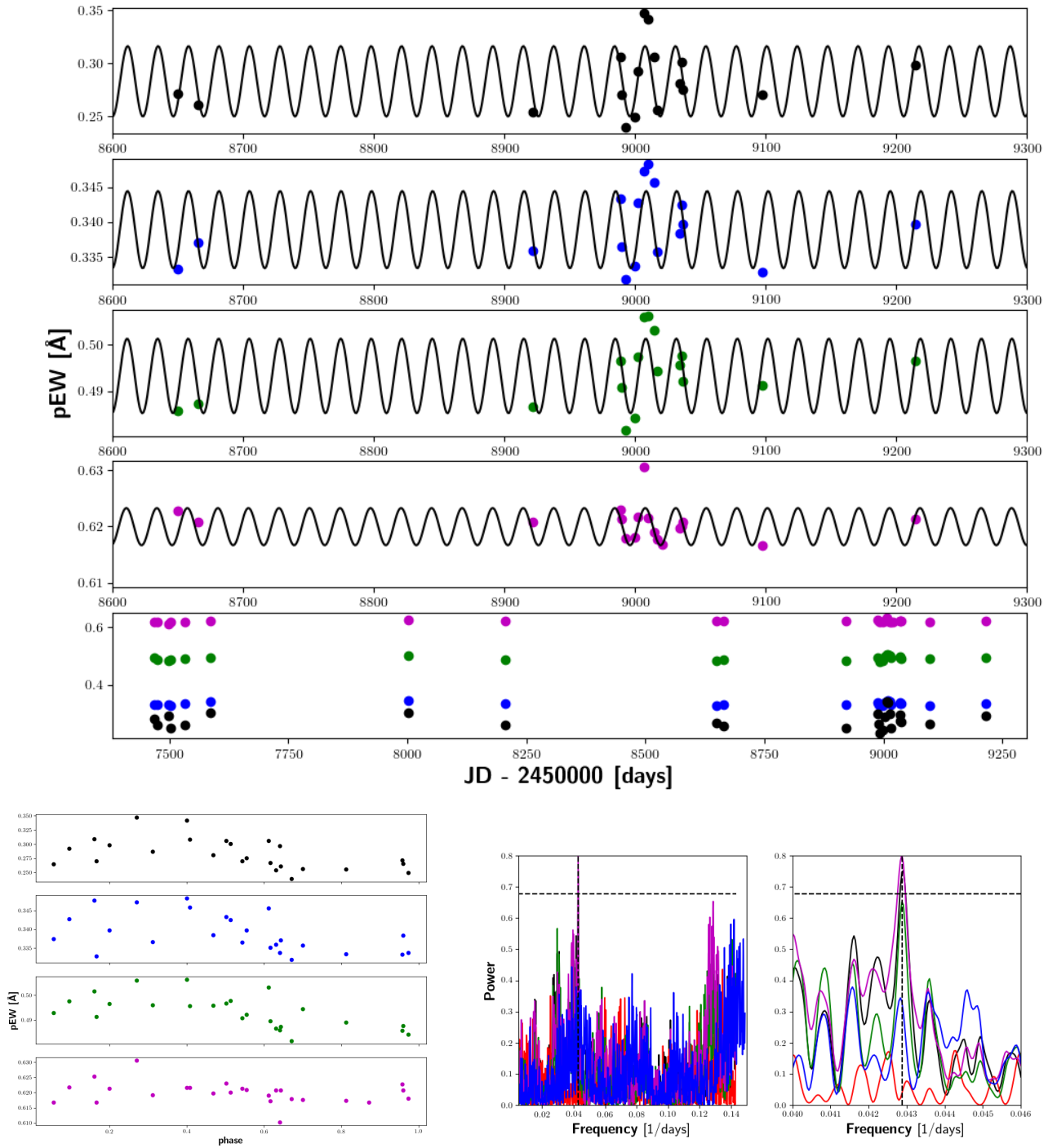


Fig. C.4. Example of spectroscopic indicator time series analysis for J14524+123. Top: time series data with sinusoids corresponding to the best-fitting period (23.3 d) overplotted; Middle: time series of the individual indicators over the entire baseline; Bottom left: phase-folded on the strongest period; Bottom right: GLS periodogram (middle) and zoom-in on the strongest period (right) of the 4 indicators, with horizontal dashed line denoting FAP = 0.1% and the peak highlighted by the vertical line. Black = H α , blue = Ca-IRTa, green = Ca-IRTb, magenta = TiO. Red denotes the window function.

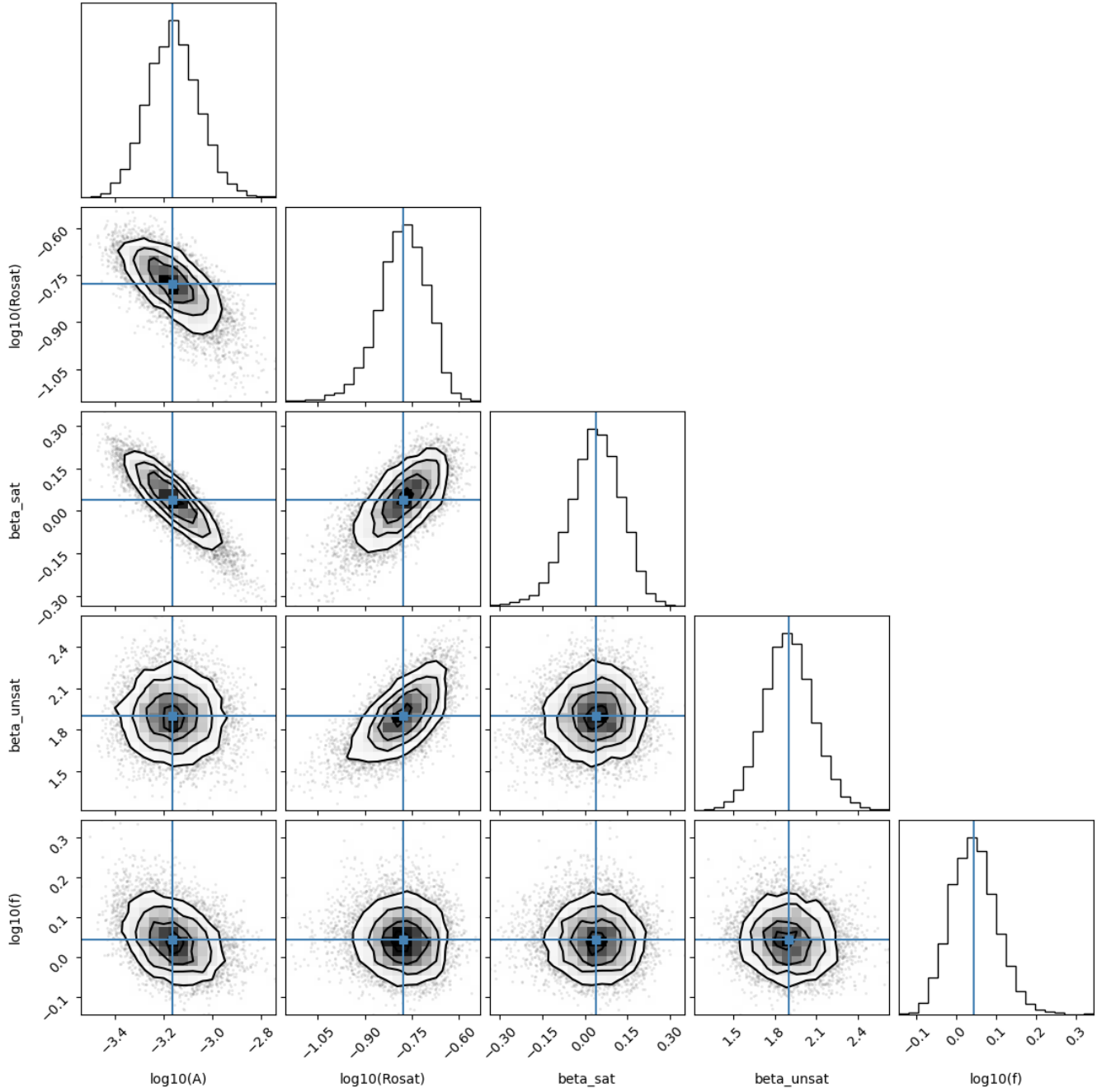


Fig. C.5. Posterior distributions for each parameter fit in the rotation-activity relation L_X/L_{bol} versus Ro , as described in Sect. 5.1 and Eqn. 6. This MCMC fit is performed over the whole stellar mass range. The contours shown are 0.5σ , 1σ , 1.5σ and 2σ . The median value for each parameter is marked in blue. This corner plot is generated using `corner.py` (<https://corner.readthedocs.io/en/latest/>).

Table C.1. Stellar parameters of the investigated stars.

Karmn	Spectral Type ^a	Best P_{rot} (d)	Source ^b	Secure flag ^c	M_{\star} (M_{\odot})	$\log \tau_{\text{d}}$	$\log Ro$	$v \sin i$ (km/s)	R_{\star} (R_{\odot})	$P_{\text{rot,max}}$ (d)	$pEW'_{\text{H}\alpha}$ (Å)	L_{bol} ($10^{-2} L_{\odot}$)	$\log \frac{L_X}{L_{\text{bol}}}$	$\log \frac{L_{\text{H}\alpha}}{L_{\text{bol}}}$	$\log R'_{\text{HK}}$	$\log \left(\frac{B}{G}\right)$	SB flag	Age ^d (Myr)	Kin. Member
J00051+457	M1.0 V	15.37	DA19	D	0.49	1.70	-0.52	< 2.0	0.49	...	-0.06	4.36	...	-5.17	-4.97	...	800	YD	
J00067-075	M5.5 V	93.00	Fou23	S	0.11	2.24	-0.27	< 2.0	0.12	...	0.00	0.14	D	
J00162+198E	M4.0 V	105.00	DA19	S	0.27	1.93	0.10	< 2.0	0.28	...	0.05	0.86	...	-5.46	-5.70	TD-D	
J00162+198W	M4.0 V	4.83	DA19	S	0.43	1.90	-1.22	...	0.43	...	-4.16	2.18	-3.09	-3.91	SB2	TD-D	
J00183+440	M1.0 V	45.00	SM18	S	0.39	1.71	-0.05	< 2.0	0.40	...	-0.07	2.39	-4.68	...	-5.33	D	
J00184+440	M3.5 V	113.30	Don23	S	0.16	1.93	0.13	< 2.0	0.17	...	-0.03	0.33	...	-5.02	-5.42	D	
J00286-066	M4.0 V	0.34	1.87	...	< 2.0	0.35	...	0.12	1.50	D	
J00389+306	M2.5 V	50.20	DA19	P	0.41	1.74	-0.04	< 2.0	0.41	...	0.04	2.46	...	-5.28	-5.11	D	
J00570+450	M3.0 V	0.33	1.82	...	< 2.0	0.34	...	-0.08	1.50	...	-4.88	YD	
J01013+613	M2.0 V	34.70	SM18	P	0.37	1.72	-0.18	< 2.0	0.37	...	-0.07	2.00	-4.65	-4.93	-5.10	D	
J01019+541	M5.0 V	0.28	DA19	S	0.14	2.20	-2.76	30.6± 3.1	0.16	0.3	-5.74	0.19	...	-3.84	800	D	
J01025+716	M3.0 V	50.52	T.W.	S	0.47	1.79	-0.09	< 2.0	0.46	...	0.08	2.99	-5.48	-5.33	-5.03	D	
J01026+623	M1.5 V	18.82	T.W.	S	0.51	1.74	-0.46	< 2.0	0.51	...	-0.04	4.83	...	-4.86	-4.43	...	800	YD	
J01033+623	M5.0 V	1.02	T.W.	S	0.23	2.05	-2.04	10.5± 2.0	0.24	1.2	-9.77	0.47	-2.97	-3.60	800	YD	
J01048-181	M5.0 V	143.20	New18	P	0.14	2.16	-0.01	< 2.0	0.15	...	0.00	0.22	...	-5.36	D	
J01056+284	M5.0 V	16.32	Bar18	P	0.14	2.05	-0.83	...	0.16	...	-0.12	0.32	SB2	TD	
J01125-169	M4.5 V	70.10	T.W.	S	0.14	2.06	-0.21	< 2.0	0.15	...	-1.36	0.23	-3.46	-4.28	-5.13	D	
J01339-176	M4.0 V	7.75	T.W.	S	0.27	1.91	-1.02	< 2.0	0.28	...	-1.62	0.90	-3.36	-4.08	YD	
J01352-072	M4.0 V	0.70	T.W.	S	0.38	1.98	-2.13	59.8± 6.9	0.72	0.6	-7.74	4.77	-2.96	-3.63	25	YD	
J01433+043	M2.0 V	14.65	T.W.	P	0.40	1.70	-0.53	< 2.0	0.40	...	-0.08	2.27	...	-5.07	-5.05	D	

Note: This table is available in its entirety at the CDS. ^a: For known SBs, we tabulate the combined spectral type or that of the primary. ^b: T.W. refers to This Work. ^c: Secure flags: ‘S’ = secure; ‘P’ = provisional; ‘D’ = debated. ^d: Ages of 800 Myr are upper limits.

Table C.2. Adopted, literature, and all measured P_{rot} of our investigated stars.

Karmn	Best P_{rot} (d)	Source	Secure flag ^a	$P1^b$ (d)	$\delta P1$ (d)	Ref1	P (Planet) (d)	Ref (Planet)	P (Laf21) (d)	P (Other phot) (d)	Other phot facility	P (TESS) (d)	TESS LC type	P (SWASP) (d)	SWASP flag	P (Spect) (d)
J00051+457	15.37	DA19	D	15.37	0.09	DA19
J00067-075	93.00	Fou23	S	93.00	1.60	Fou23	126.00	SM23
J00162+198E	105.00	DA19	S	105.00	44.00	DA19
J00162+198W	4.83	DA19	S	4.83	0.06	DA19
J00183+440	45.00	SM18	S	45.00	4.40	SM18	43.82	How14	46.19
J00184+440	113.30	Don23	S	113.30	4.30	Don23
J00286-066
J00389+306	50.20	DA19	P	50.20	1.30	DA19
J00570+450
J01013+613	34.70	SM18	P	34.70	0.10	SM18
J01019+541	0.28	DA19	S	0.28	0.00	DA19	0.14	PDCSAP
J01025+716	50.52	LCO-V	S	51.50	2.60	DA19	51.73	50.52	LCO-V	51.37
J01026+623	18.82	OSN-R	S	19.90	0.40	DA19	18.90	Per19	20.00	18.82	OSN-R	18.94	SAP	18.89
J01033+623	1.02	TESS	S	1.02	0.01	DA19	1.02	PDCSAP
J01048-181	143.20	New18	P	143.20	...	New18
J01056+284	16.32	Bar18	P	16.32	0.24	Bar18
J01125-169	70.10	SWASP	S	69.20	2.40	DA19	83.00	AD17b	80.67	70.10
J01339-176	7.75	TESS-SAP	S	7.85	...	Pas23	7.75	SAP
J01352-072	0.70	TESS	S	0.70	...	Kir12	0.70	PDCSAP
J01433+043	14.65	SWASP	P	14.65

Note: This table is available in its entirety at the CDS. ^a: Secure flags: ‘S’ = secure; ‘P’ = provisional; ‘D’ = debated. ^b: Other literature periods can be found in online version of this table.

Table C.3. List of reference abbreviations to Table C.2.

Abbreviation	Reference
AD17b	Astudillo-Defru et al. 2017b
AD17c	Astudillo-Defru et al. 2017c
Aff19	Affer et al. 2019
Ama21	Amado et al. 2021
Bar18	Baroch et al. 2018
Bla23	Blanco-Pozo et al. 2023
Blu20	Bluhm et al. 2020
Bon18	Bonfils et al. 2018
Bou18	Bourrier et al. 2018
Cab22	Caballero et al. 2022
Clo17	Cloutier et al. 2017
Clo20	Cloutier et al. 2020
DA19	Díez Alonso et al. 2019
Don08	Donati et al. 2008
Dav16	David et al. 2016
Ded21	Dedrick et al. 2021
Dia19	Díaz et al. 2019
Don23	Donati et al. 2023
Dre20	Dreizler et al. 2020
Fen20	Feng et al. 2020
Fek00	Fekel & Henry 2000
Fou23	Fouqué et al. 2023
GA20	González-Álvarez et al. 2020
GA21	González-Álvarez et al. 2021
GA23	González-Álvarez et al. 2023
Gil16	Gillon et al. 2016
Gor23	Gorini et al. 2023
GR98	Greimel & Robb 1998
Hal08	Hallinan et al. 2008
Hag10	Haghighipour et al. 2010
Har11	Hartman et al. 2011
Heb16	Hébrard et al. 2016
Hob18	Hobson et al. 2018
Hob19	Hobson et al. 2019
How14	Howard et al. 2014
How20	Howard et al. 2020
Irv23	Irving et al. 2023
Irw11	Irwin et al. 2011
Joh07	Johnson et al. 2007
Joh10	Johnson et al. 2010
Kir12	Kiraga 2012
Kos23	Kossakowski et al. 2023
KS07	Kiraga & Stepień 2007
KS13	Kiraga & Stepień 2013
Laf21	Lafarga et al. 2021
Lal19	Lalitha et al. 2019

Table C.3. Continued.

Abbreviation	Reference
Lot18	Lothringer et al. 2018
Luq18	Luque et al. 2018
Luq19	Luque et al. 2019
Luq22	Luque et al. 2022
Med20	Medina et al. 2020
Med22	Medina et al. 2022
Mes11	Messina et al. 2011
Mor08	Morin et al. 2008
Mor10	Morin et al. 2010
Mor19	Morales et al. 2019
Mou17	Moutou et al. 2017
Nag19	Nagel et al. 2019
New16	Newton et al. 2016b
New18	Newton et al. 2018
Nor07	Norton et al. 2007
Oel18	Oelkers et al. 2018
Ola16	Oláh et al. 2016
Pas22	Pass et al. 2022
Pas23	Pass et al. 2023
Per19	Perger et al. 2019
Pin19	Pinamonti et al. 2019
Poj05	Pojmanski et al. 2005
Qui22	Quirrenbach et al. 2022
Rae20	Raetz et al. 2020
Rei20	Reinhold & Hekker 2020
Rib18	Ribas et al. 2018
Riv05	Rivera et al. 2005
Sar18	Sarkis et al. 2018
SM15	Suárez Mascareño et al. 2015
SM16	Suárez Mascareño et al. 2016
SM17	Suárez Mascareño et al. 2017b
SM17b	Suárez Mascareño et al. 2017a
SM18	Suárez Mascareño et al. 2018
SM23	Suárez Mascareño et al. 2023
Ste16	Stelzer et al. 2016
Sto20a	Stock et al. 2020a
Sto20b	Stock et al. 2020b
Ter22	Terrien et al. 2022
Tes04	Testa et al. 2004
TP19	Toledo-Adrón et al. 2019
TP21	Toledo-Adrón et al. 2021
Tri21	Trifonov et al. 2021
Vid17	Vida et al. 2017
Wat06	Watson et al. 2006
Wes15	West et al. 2015

Table C.4. Planets table.

Karmin	Best P_{rot} (d)	Secure flag	Transit flag	P_{orb1} (d)	$m_P \sin i1$ (m_{\oplus})	Ref1	P_{orb2} (d)	$m_P \sin i2$ (m_{\oplus})	Ref2	P_{orb3} (d)	$m_P \sin i3$ (m_{\oplus})	Ref3	Add. planets
J00067-075	93.00	S		10.35	1.08	SM23	21.20	1.36	SM23		
J00183+440	45.00	S		11.44	3.98	Tri22 Rib23	6694.00	50.40	Tri22 Rib23		
J01026+623	18.82	S		13.85	5.63	Per19		
J01125-169	70.10	S		2.02	0.70	Sto20a	3.06	1.14	Sto20a	4.66	1.09	Sto20a	
J02002+130	2.00	S		771.40	67.00	Qui22		
J02530+168	97.56	S		4.91	1.05	Zec19	11.41	1.11	Zec19		
J03133+047	126.20	S		2.29	3.95	Bau20		
J04167-120	33.00	P	Y	4.05	30.80	Dre20		
J04429+189	40.70	S		8.78	9.10	Tri18		
J04520+064	...			2288.00	260.00	How10		
J04538-177	53.10	P		17.13	6.49	Fen20	106.30	7.56	Fen20		
J05019-069	93.87	S		5.36	2.02	AD17c	40.54	2.31	AD17c		
J06105-218	27.30	S		122.00	7.27	Fen20	526.00	8.48	Fen20		
J06371+175	37.50	S		2.77	2.14	Luq22	5.71	3.09	Luq22		
J06548+332	122.00	S		14.24	4.27	Sto20b Rib23		
J07274+052	93.50	D		4.72	1.18	AD17c	18.65	2.89	AD17c		
J08023+033	...		Y	1.20	1.86	Kem20	15.51	7.41	Kem20		
J08409-234	57.50	D		695.66	557.10	Fen20	6739.00	522.50	Fen20		
J08413+594	83.27	S		203.13	146.00	Mor19 Rib23	2350.00	143.00	Mor19 Rib23		
J09144+526	16.88	S		24.45	10.27	GA20		
J09360-216	74.30	S	Y	3.93	1.84	Luq19	9.12	3.40	Luq19	55.66	6.10	Luq19	
J10023+480	...			3.82	13.02	Hob19		
J10088+692	41.20	S	Y	3.44	5.90	Blu20		
J10289+008	31.72	S		7.03	1.71	Ama21		
J11033+359	56.15	S		12.95	2.69	Sto20b		
J11110+304E	40.00	P		50.80	7.60	Ded21	749.83	53.83	Ded21		
J11302+076	36.40	S	Y	32.94	8.49	Sar18		
J11417+427	71.50	D		41.38	96.60	Tri20	532.60	72.10	Tri20		
J11421+267	44.60	S		2.64	21.36	Tri18		
J11477+008	112.83	S		9.87	1.40	Bon18		
J11509+483	148.95	S		389.70	10.60	Bla23		
J12123+544S	96.70	P		13.67	6.89	Sto20b		
J12388+116	55.35	S		9.57	13.20	Fen20		
J12479+097	49.90	D	Y	1.47	2.82	Tri21		
J13229+244	95.00	D		3.02	8.00	Luq18		
J13299+102	30.00	S		140.43	5.20	Dam22		
J14010-026	43.90	S		8.71	6.52	Tri18		
J14342-125	94.77	S		36.12	2.59	GA23		
J15194-077	132.50	S		5.37	15.20	Tri18	12.92	5.65	Tri18	3.15	1.66	Tri18	
J16102-193	6.26	S	Y	5.43	...	Dav16		
J16167+672S	22.00	P		86.57	23.00	Rei18b Rib23		
J16254+543	76.79	S		14.63	2.82	SM17b		
J16303-126	119.00	S		4.89	1.36	Wri16	17.87	4.25	Wri16	67.27	5.21	Wri16	
J16581+257	23.80	S		598.30	104.24	Joh10		
J17033+514	115.00	P		6.94	3.71	Gor23		
J17355+616	18.39	S		24.16	9.00	Pin19		
J17378+185	35.02	S		15.53	6.64	Lal19		
J17578+046	145.00	S		232.80	3.23	Rib18		
J18353+457	34.00	S		19.47	13.64	GA21		
J18409-133	28.23	P		5.10	10.75	Gor23		
J18580+059	35.20	S		2.38	2.96	TP21		
J19169+051N	46.00	S		105.90	12.20	Kam18		
J20260+585	159.88	S		15.56	1.26	Kos23		
J20450+444	39.12	P	Y	0.93	1.90	Pal22	6.64	5.80	Pal22		
J20451-313	4.89	S	Y	8.46	20.12	Cal21	18.86	0.00	Cal21		
J21164+025	42.68	S		14.44	13.40	Lal19		
J21221+229	38.40	S		691.90	105.00	Qui22		
J21466+668	100.00	P		2.31	2.50	Ama21	8.05	3.75	Ama21		
J22096-046	39.20	S		1915.00	286.00	Mon14	7068.00	223.10	Mon14		
J22137-176	116.40	P		3.65	7.40	Luq18		
J22252+594	64.60	S		13.35	16.57	Nag19		
J22532-142	81.00	S		61.08	760.90	Tri18	30.13	241.50	Tri18	1.94	6.91	Tri18	Y
J23064-050	3.30	S	Y	1.51	1.37	Ago21	2.42	1.31	Ago21	4.05	0.39	Ago21	Y

Note: This table is available in its entirety (including additional planets) at the CDS.

Table C.5. List of reference abbreviations to Table C.4.

Abbreviation	Reference
Ago21	Agol et al. 2021
AD17c	Astudillo-Defru et al. 2017c
Ama21	Amado et al. 2021
Bau20	Bauer et al. 2020
Bla23	Blanco-Pozo et al. 2023
Blu20	Bluhm et al. 2020
Bon18	Bonfils et al. 2018
Cal21	Cale et al. 2021
Dam22	Damasso et al. 2022
Dav16	David et al. 2016
Ded21	Dedrick et al. 2021
Dre20	Dreizler et al. 2020
Fen20	Feng et al. 2020
GA20	González-Álvarez et al. 2020
GA21	González-Álvarez et al. 2021
GA23	González-Álvarez et al. 2023
Gor23	Gorini et al. 2023
Hob19	Hobson et al. 2019
How10	Howard et al. 2010
Joh10	Johnson et al. 2010
Kam18	Kaminski et al. 2018
Kem20	Kemmer et al. 2020
Lal19	Lalitha et al. 2019
Luq18	Luque et al. 2018
Luq19	Luque et al. 2019
Luq22	Luque et al. 2022
Mon14	Montet et al. 2014
Mor19	Morales et al. 2019
Nag19	Nagel et al. 2019
Pal23	Palle et al. 2023
Per19	Perger et al. 2019
Pin19	Pinamonti et al. 2019
Qui22	Quirrenbach et al. 2022
Rei18b	Reiners et al. 2018a
Rib18	Ribas et al. 2018
Rib23	Ribas et al. 2023
Sar18	Sarkis et al. 2018
SM17b	Suárez Mascareño et al. 2017a
SM23	Suárez Mascareño et al. 2023
Sto20a	Stock et al. 2020a
Sto20b	Stock et al. 2020b
TP21	Toledo-Adrón et al. 2021
Tri18	Trifonov et al. 2018
Tri20	Trifonov et al. 2020
Tri21	Trifonov et al. 2021
Tri22	Trifonov et al., in prep
Wri16	Wright et al. 2016
Zec19	Zechmeister et al. 2019